Developing Spatially-Offset Femtosecond Stimulated Raman Spectroscopy to Investigate Charge Transport Through a Vibrational Lens

A THESIS

SUBMITTED TO THE FACULTY OF THE

UNIVERSITY OF MINNESOTA

BY

Siu Yi Kwang

IN PARTIAL FULFILLMENT OF THE REQUIREMENTS

FOR THE DEGREE OF

DOCTOR OF PHILOSOPHY

Advisor: Renee R. Frontiera

May, 2021

Acknowledgements

I may be the only author on this thesis, but I did not make it here alone.

Thank you Renee, for being my advisor, and for guiding me through my research project. Thank you for being flexible with me while pushing me when you knew I could achieve something. You're part of the reason why I chose to attend University of Minnesota and I'm glad that I did.

To Professors James Johns, David Blank, Aaron Massari, Ken Leopold, Russ Holmes, thank you for being part of my academic journey. Thank you for serving on my oral or thesis committee and for the scientific conversations that we've had.

To my precious labmates, past and present, thank you so much for your support! To Ruchira, thank you for being so helpful to me in my first few years in graduate school. To Dave, you're so inspirational and I thank you for all the discussions we've had. To Chris R, thank you for being on the Libra team and helping to shoulder some responsibility for being the most 'senior' person on Libra. To Ariel, thank you for baked treats and for being a great role model at juggling sooo many responsibilities at once. To Emily, Alyssa, Jamie and Christian, thank you for being pioneers of the group. To Chris W, I remember being excited about not being the most junior member in the lab. Soon, you will be the most senior graduate student and I know you'll do great! To Ryan, Ziwei and Margaret, each of you bring something different to the lab and I'm glad all of you joined. Thank you for the chats in the labs or corridors. To Shahzad and Arghya, both of you had to spend most of last year learning the ropes through remote help, but

you pulled through and you'll keep growing! To Polly, Collin and Joe, welcome to the Frontiera Raman family and hope you'll make more wonderful memories here!

If you notice one name missing, that's because awesome Kajari deserves a separate mention. Thank you Kajari for being my lab twin, for growing with me together. I remember that one semester when our TA assignments were side by side, that was fun. Thank you for all the wonderful memories and for keeping in touch after graduating. Can't wait for our getaway trip!

To Katie and Fei, thank you for being such wonderful friends. Thank you for giving me the honor of being Fred's (cute cat) god-mum and supporting me through the ups and downs of graduate school. Thank you for the hotpots and the many chats, and I'm excited that we'll still be around to support one another for years to come.

To my parents, thank you for accepting my decision to leave Singapore in search of opportunities here. Thank you for your love and support even when you're so faraway. 我已经长大了，你们不用担心我了。 When covid is over, I will be able to visit home more regularly.

To Linda, Ray, Katie and Pat, thank you for accepting me into your family. Sorry for not addressing you directly by your first names often yet because that is considered to be really rude in Chinese culture. To Vega and Clover, thank you for being such cute kitties and being such a wonderful addition to my life.

Last but not least, thank you Ryan, my favorite (and only) husband. To friends who are finding out for the first time, don't worry, this is a very recent development and the wedding is postponed until post-covid. And I don't consider myself 100% married until after our wedding. Thank you Ryan, for supporting me and for believing in me when I don't. Here's to many years of adventure and growth together.

Abstract

Current solar cell technology based on a single p-n junction has a maximum efficiency dictated by the Shockley-Queisser limit of 33%. Singlet fission, which occurs in some organic semiconductors, has the potential to push that limit to 44% because it results in the formation of two separate triplets from the input of one photon. In order for organic semiconductor solar cells based on singlet fission to be a viable option, the excitons need be capable of traveling a sizable distance (up to microns) to reach the electrodes. Thus, understanding what facilitates or hinders exciton transport is crucial in the optimization of charge transport efficiency. However, exciton transport is notoriously difficult to study because they are short-lived, have short diffusion lengths, and easily recombine.

In this project, I focused on developing a brand new ultrafast Raman imaging technique called spatially-offset femtosecond stimulated Raman spectroscopy (SO-FSRS) that has both the spatial and temporal resolution to track structural changes in molecular systems during exciton transport. Any structural changes can alter the frequencies or intensities of vibrational modes which are reflected in the Raman spectra. In the experimental setup, the photoexcitation pulse is displaced from the Raman probe and pump pulses such that excitons are generated at a known distance from the probing region. The photoexcitation pulse is then raster-scanned to generate a Raman map of exciton transport. The details on how SO-FSRS are developed are documented in this thesis.

After the successful development of SO-FSRS, its utility was first demonstrated with 6,13-bis(triisopropylsilylethynl) pentacene. I showed that the fast exciton and free charge carrier transport axes are identical, but the exciton transport is less anisotropic by a factor of $\sim$3. SO-FSRS is the first technique that can directly track molecular structural evolution during exciton transport, which can provide us with chemical insights on how to tailor-make molecules for specific electronic devices.

Contents

List of Tables

List of Figures

List of Abbreviations

FSRS	femtosecond stimulated Raman spectroscopy
SO-FSRS	spatially-offset femtosecond stimulated Raman spectroscopy
TIPS-pn	6,13-bis(triisopropylsilylethynyl) pentacene
e-h	electron-hole
HOMO	highest occupied molecular orbital
LUMO	lowest unoccupied molecular orbital
CT	charge transfer
TA	transient absorption
NOPA	non-collinear optical parametric amplification
BBO	beta barium borate
FWHM	full-width at half-maximum
SERDS	shifted excitation Raman difference spectroscopy
VSFG	vibrational sum frequency generation
SF	singlet fission
IR	infrared
RR	resonance Raman
TRRR	time-resolved resonance Raman
ISRS	impulsive stimulated Raman spectroscopy
TR-PL	time-resolved photoluminescence
2DES	two-dimensional electronic spectroscopy
TR-2PPE	time-resolved two-photon photoemission
TR-EPR	time-resolved electron paramagnetic resonance
NBO	natural bond orbital
THz	terahertz
TAM	transient absorption microscopy

PSU	power supply unit
DAQ	data acquisition
PCI	peripheral component interconnect
AWG	American wire gauge
NI MAX	National Instruments Measurement & Automation Explorer
$MAPbI_3$	methylammonium lead iodide

Chapter 1

Introduction

1.1 Motivation

Despite growing between 15-25% each year for the past five years, solar energy only contributed to 1.3% of U.S. energy consumption in 2020. [13] Thus, solar energy is an under-utilized resource. The efficiency of single-junction solar cells is capped at a theoretical limit of 33% due to inherent energy loss when absorbed light gets converted into electrical energy. [14] In recent years, there has been growing interest in organic semiconductors that undergo singlet fission, a unique process that can create twice the electrical carriers, or charges, for every light input. Not only is this class of solar cells more environmentally friendly, the maximum efficiency achievable is also increased to 45%. [15] However, the best organic semiconductor solar cells available today only have an efficiency of 18.2%. [16] They cannot operate at their maximum potential because a lot of energy is lost during the generation and movement of these charges to electrodes where electrical currents are generated. In order to push the efficiency of these organic solar cells closer to its theoretical limit, gaps in our understanding of the mechanisms of charge generation and charge transport need to be bridged.

Femtosecond stimulated Raman spectroscopy (FSRS) is a vibrationally sensitive

technique that can track structural changes in molecular systems after photoexcitation on the femtosecond timescale. Thus, FSRS allows for the mechanism of charge generation to be studied closely. Studying charge transport is more tricky because the generated charges, typically excitons, tend to have short lifetimes [17, 18] and short diffusion lengths. [19] To track molecular structural changes during charge transport, I aimed to introduce a spatial component to FSRS to develop spatially-offset FSRS (SO-FSRS). SO-FSRS has all the benefits of FSRS but is specifically equipped to image charge transport and seek out structural insights on what facilitates or hinders charge transport. Using SO-FSRS to study photovoltaics allows us to gain chemical insights on how to tailor modifications of existing systems to enhance their solar cell performances.

1.2 Outline

This thesis focuses on highlighting the utility of vibrationally sensitive ultrafast spectroscopic techniques and documents the development of SO-FSRS, the first excited-state imaging technique that can directly track structural evolution in molecular systems during charge transport.

Chapter 2 provides the theoretical background behind exciton transport, singlet fission and FSRS. It then covers the experimental setup used in FSRS and SO-FSRS experiments, followed by how Raman features can be isolated with certainty in FSR spectra.

Chapter 3 describes how vibrational spectroscopies have contributed to the advancement in singlet fission chromophore design. It ends with future directions that vibrational techniques can continue to bring to the field of singlet fission.

Chapter 4 documents the development of SO-FSRS, from the selection of hardware to the writing of codes to analyzing the acquired data. This is meant as a reference guide for future users of SO-FSRS to gain a understanding on its operations and how it can be further improved in future.

Chapter 5 demonstrates the utility of SO-FSRS by testing it out on a model system 6,13-bis(triisopropylsilylethynyl) pentacene (TIPS-pn). It also shows how SO-FSR spectra can be analyzed and interpreted.

Chapter 6 discusses the future directions on SO-FSRS. It describes a few photovoltaic systems that are suitable to be studied with SO-FSRS. It also introduces the possibility of incorporating compressive sensing with SO-FSRS to signficantly reduce data acquisition.

Last but not least, chapter 7 brings this thesis to a conclusion. It summarizes the progress I achieved in developing SO-FSRS and where the technique will go.

Chapter 2

Background

2.1 Exciton Transport

2.1.1 Excitons in Molecular Crystals

Excitons are bound electron-hole (e-h) pair systems. In organic molecular crystals, a closed-shell molecule in its ground state has a pair of electrons in its highest occupied molecular orbital (HOMO). When one of the electrons is promoted into the lowest unoccupied molecular orbital (LUMO), a hole is generated in the HOMO. In an organic semiconductor molecular crystal, the electron can be promoted into the LUMO of the same molecule, or the LUMO of its nearest neighbor.

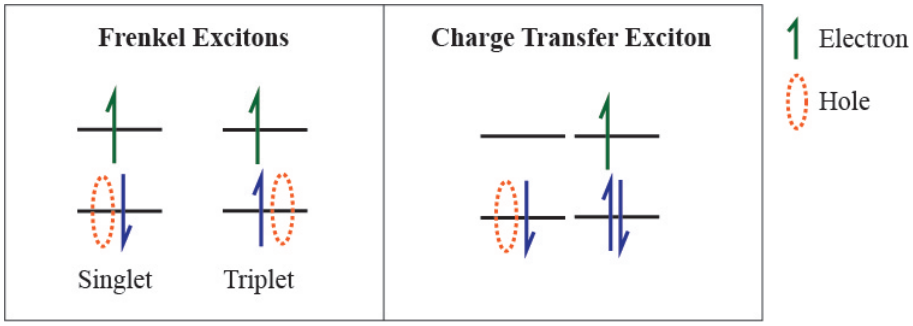

Figure 2.1: A Frenkel exciton (left) is a bound e-h pair localized on the same molecule. When the total spin of the molecule is 0 or 1, the exciton is in its singlet or triplet state respectively. A CT excition (right) is a bound e-h pair that is residing in adjacent molecules.

In the first scenario, the bound e-h localized on one molecule is known as Frenkel exciton. Frenkel excitons can either be singlets or triplets, depending on the spin of the electrons. In the second scenario, the e-h pair is found on two adjacent molecules and is known as the charge transfer (CT) exciton. These excitons are schematically represented in Figure 2.1. The distinction between Frenkel and CT excitons is not always clear due to the delocalization of electrons. Instead, it is more accurate to think of the excitons having a significant CT nature, observed by a separation of electron density. By considering only nearest neighbor interactions, such a system can be described generically by an electronic Hamiltonian as shown below: [20]

$$\begin{aligned}\hat{H}_{el} = &\sum_n [-U(0)c_n^\dagger c_n d_n^\dagger d_n - U(1)c_n^\dagger c_n d_{n+1}^\dagger d_{n+1}] \\ &+ \sum_n [t_e c_n^\dagger c_{n+1} + t_h d_n^\dagger d_{n+1} + H.C.] + \sum_n [V c_n^\dagger d_n^\dagger d_{n+1} c_{n+1} + H.C.]\end{aligned} \tag{2.1}$$

where $c_n^\dagger(c_n)$ refer to the electron creation (annihilation) operators at site n, $d_n^\dagger(d_n)$ refer to the hole creation (annihilation) operators, $U(0)$ and $U(1)$ are the Coulomb energies of an $e-h$ pair in a Frenkel and CT exciton respectively, $H.C.$ is the Hermitian conjugate of the previous term, $t_e(t_h)$ is the transfer matrix element for the nearest neighbor

electron (hole) transfer and V is the dipole-dipole interaction term that transfers an $(e-h)$ pair from site $n+1$ to site n.

The first term corresponds to the electronic states of the Frenkel ($U(0)$) and CT ($U(1)$) excitons, whereas the second term accounts for the hopping of electrons or holes to the nearest neighbors (thereby changing a Frenkel exciton to a CT exciton and vice versa) and the third term accounts for when an exciton travels from site $n+1$ to site n, where n refers to a single molecule in a molecular crystal.

In many organic systems, the exciton binding energy $U(1)-U(0)$ is usually significantly larger than the interaction terms $V/t_e/t_h$. While not entirely accurate, it is reasonable to assume that Frenkel and CT excitons can be treated separately and the Hamiltonian can be rewritten as: [20]

$$\hat{H}_{el} = \hat{H}_{\text{Frenkel}} + \hat{H}_{\text{CT}} \tag{2.2}$$

where

$$\hat{H}_{\text{Frenkel}} = -U(0)\sum_n c_n^\dagger c_n d_n^\dagger d_n + \sum_n [V c_n^\dagger d_n^\dagger d_{n+1} c_{n+1} + H.C.] \tag{2.3}$$

and

$$\hat{H}_{\text{CT}} = -U(1)\sum_n c_n^\dagger c_n d_{n+1}^\dagger d_{n+1} + \sum_n [t_e c_n^\dagger c_{n+1} + t_h d_n^\dagger d_{n+1} + H.C.] \tag{2.4}$$

Although the bound e-h pair is found on different molecules in a CT exciton, CT excitons are not less localized than Frenkel excitons. Based on the Hamiltonians in Equations 2.3 and 2.4, both Frenkel and CT excitons can have wave functions that are delocalized over N sites. The difference is that the degree of charge separation within the basis functions will be larger for CT excitons.

It was assumed that Frenkel and CT excitons can be treated separately, and they can only couple with the same species because one consists of neutral states, while the latter consists of ionic states. [21,22] However, this is an oversimplified assumption. The coupling term $\hat{H}_{\text{Frenkel-CT}}$ is not negligible, [23–26] and processes such as the dissociation

of a Frenkel exciton into a CT exciton are viable. In singlet fission, Frenkel singlet and triplet excitons are generated, and their diffusion rates are of interest.

2.1.2 Exciton Diffusion

The transport or diffusion of excitons through a molecular crystal can be thought of as a random hopping of electrons into holes across one molecule to the other, with no physical displacement of the molecules. The hopping rate, k_{da} of the excitons can be approximated in terms of Fermi Golden's Rule: [27]

$$k_{da} = \frac{2\pi}{\hbar}|V_{da}|^2 \left(\frac{\sqrt{\pi}}{2\sigma} \exp\left[-\frac{\Delta_{da}^2}{4\sigma^2} \right] \right) \tag{2.5}$$

where V_{da} is the electronic coupling between the donor and acceptor states and the term in parentheses is the Franck-Condon-weighted density of states, with σ as the Gaussian width of the absorption (acceptor) and emission (donor) spectra (assuming the Gaussian widths are the same) and Δ_{da} as the Stokes shift between these two spectra. This expression makes use of the Condon approximation where it is assumed that the excitonic transition is so fast that the transition probability can be calculated at a fixed nuclear coordinate. [28] For singlets, the electronic coupling is often assumed to be dominated by Förster coupling as shown:

$$V_{da,\text{singlet}} \approx \frac{\kappa\mu^2}{n^2 R^3} \tag{2.6}$$

where μ is the magnitude of the transition dipole, n is the refractive index of the molecular crystal and R is the distance between the centers of masses of the donor and acceptor. κ has a value between 0 and 2 and it refers to the orientational factor, which is dependent on the relative orientation of the two transition dipoles.

Förster energy transfer, as depicted in Figure 2.2a, is a process where the energy of the excited electron on a singlet exciton is transferred non-radiatively to excite a

neighboring ground state electron to the corresponding excited state. A larger Förster coupling increases the probability of this process, and that translates to a more rapid hopping rate. Besides the hopping rate, the lifetimes of singlets also need to be considered to figure out their diffusion lengths. Due to the spontaneous radiation of the excited electron back to its ground state, its radiative lifetime, τ_{S} can be expressed as: [27]

$$\tau_{\mathrm{S}} = \frac{3c^2}{4E_S^3\mu^2} \tag{2.7}$$

where c is the speed of light and E_S is the singlet excitation energy. As shown in Equations 2.6 and 2.7, having a large transition dipole μ increases the electronic coupling V_{da} and hence the hopping rate k_{da}, but also decreases the lifetime of the singlet state. This competition prevents the diffusion lengths of singlets from increasing indefinitely, and they can range from a few nanometers [29–31] to few tens of nanometers. [32, 33] The Förster diffusion length $L_{D,S}$ can be expressed with empirical parameters: [20]

$$L_{D,S} = 6.36\sqrt{\eta}\, C^{2/3} R_0^3 \tag{2.8}$$

where C is the chromophore number density, R_0 is the Förster radius and η is the correction factor that accounts for chromophore density and the time derivative of mean squared displacement, [34, 35] and its calculated value ranges from 0.32 to 0.56. R_0 is defined as: [36]

$$R_0^6 = \frac{9000(\ln 10)\kappa^2 Q_D}{128 N_A \pi^5 n^4} \left[\frac{\int_0^\infty \epsilon_A(\bar{v}) F_D(\bar{v}) \bar{v}^{-4} d\bar{v}}{\int_0^\infty F_D(\bar{v}) d\bar{v}} \right] \tag{2.9}$$

where $\bar{v}$ is the energy in wavenumbers, Q_D is the quantum yield of the donor, N_A is Avogadro's number, n is the refractive index of the medium where the transfer takes place, $\epsilon_A(\bar{v})$ is the molar absorption coefficient of the acceptor, $F_D(\bar{v})$ is the fluorescence intensity of the donor and κ is the same oriental factor as mentioned in Equation 2.6. The ratio of integrals in the square brackets, which is represented by $J(\bar{v})$, represents the extent of spectral overlap between the fluorescence spectrum of the donor and the

absorption spectrum of the acceptor.

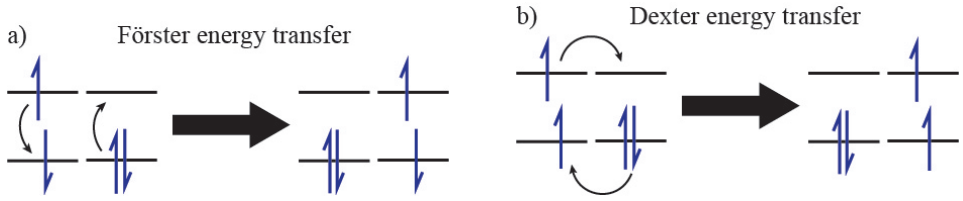

Figure 2.2: (a) Förster energy transfer is where an excited singlet state is transferred to its neighboring molecule by a non-radiative energy transfer as depicted by the curved arrows. (b) Dexter energy transfer is the main mechanism for triplet transport, where there is an electron exchange, as depicted by the curved arrows.

The same transfer mechanism does not work for triplet excitons because the Pauli Exclusion Principle prevents the excited electron in a triplet from returning to the ground state already occupied by another electron of the same spin. Instead, the dominant transfer mechanism for triplet excitons is the Dexter energy transfer, as shown in Figure 2.2b. The exchange of electrons between the donor and acceptor molecules depends on the magnitude of Dexter coupling which increases when there is a higher degree of overlap between the wave functions of the donor and acceptor. The Dexter coupling can be expressed as:

$$V_{da,\text{triplet}} \approx A \exp[-\zeta R] \tag{2.10}$$

where A is an pre-exponential factor that reflects the triplet energy transfer coupling and can be calculated from the fragment spin difference scheme published in reference [37], while $\zeta \approx 0.28\,\text{nm}^{-1}$ is the spatial extent of the overlap. Although the probability of Dexter energy transfer decays exponentially with distance, triplets have a much longer lifetime than singlets because triplets decay back to ground state singlets by phosphorescence, a slow intersystem crossing process that is dependent on spin-orbit coupling, which is very small for most organic semiconductors.

Diffusion lengths of excitons in organic semiconductors have been empirically determined to be on the orders of nanometers [38–40] to microns. [41, 42] While singlets are short-lived, their hopping rate is much higher; while triplets diffuse more slowly, they have a much longer lifetime. As both excited singlet and triplet excitons are generated in singlet fission, the more dominant form of exciton transport depends upon the system.

2.2 Singlet Fission

2.2.1 Principle Behind Singlet Fission

Singlet fission is a spin-allowed process where an excited singlet can undergo fission to lead to the formation of two individual triplets. A simplified version of the process can be expressed with the following chemical equation:

$$S_1 + S_0 \rightleftharpoons {}^1(TT) \rightleftharpoons {}^1(T\cdots T) \rightleftharpoons T_1 + T_1 \tag{2.11}$$

where S_1 is the first excited singlet state of a chromophore, T_1 is its first triplet state and S_0 is its ground state. A closed shell ground state is always a singlet state because the HOMO is occupied with a pair of electrons and the total magnetic spin of the chromophore will be 0. ^{1}(TT), which is known as the correlated triplet state or a multiexciton state, is an observable intermediate for the singlet fission process. [43,44] As ^{1}(TT) loses its electronic coupling while retaining its spin coherence, it forms ^{1}(T...T), [45, 46] the separated correlated triplet pair, which eventually loses its spin coherence to generate two individual triplet excitons T_1.

In singlet fission, a chromophore is first excited to the S_1 state via the absorption of a photon. Initially, it is not coupled with the neighboring chromophore, which is in its ground state S_0. An interaction Hamiltonian operator, $\hat{H}_{int} = \hat{H}_{el} + \hat{H}_{sp}$ acts on these two chromophores to induce the singlet fission process. $\hat{H}_{el}$ is a spin-free electrostatic

part that is shown in Equation 2.1, while $\hat{H}_{sp}$ is a spin-dependent part that accounts for spin-spin dipole interactions and Zeeman interactions [a] with an external magnetic field.

$\hat{H}_{el}$ acts on $S_1 + S_0$ to convert them into a coupled triplet state, where the electronic spins on both triplets are coherent, which means that the electronic angular momentums of the two chromophores have the same phase difference and the same frequency. [48] This electronic spin coherence allows the chromophores to retain singlet characteristics, making singlet fission a spin-allowed process. The depiction of ^{1}(TT) as an intermediate in Equation 2.11 is a simplified picture. If the electronic coupling between the two chromophores are weak, the energies of the singlet ^{1}(TT), triplet ^{3}(TT) and quintet ^{5}(TT) will be approximately degenerate. If this coupling is within $1\,\mathrm{cm}^{-1}$, the $\hat{H}_{sp}$ operator can act on the correlated triplet pair to mix these states sufficiently and the intermediate will be in a superposition of all three states. Thus, an external magnetic field can interfere with the singlet fission process and the spin coherence mentioned above will gradually be lost and the correlated pair diffuses apart as two individual triplets. The corresponding expanded Jablonski diagram is described in Figure 2.3.

[a] Spin of an electron is its intrinsic angular momentum. Spin-spin dipole interactions refer to the interaction energies between the magnetic dipole moments that arise from the spin of electrons. Zeeman interactions occur between an external magnetic field and a magnetic dipole moment associated with the electron spin, leading to a shift in energy levels. [47]

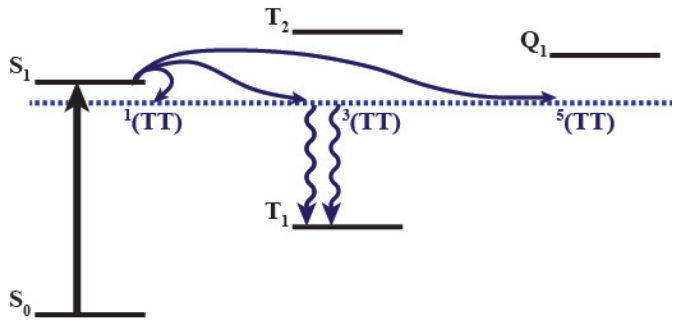

Figure 2.3: When the ground state singlet S_0 is excited to a S_1 state, it can couple with a neighboring molecule to give a correlated triplet pair state, which is a superposition of ^{1}(TT), ^{3}(TT) and ^{5}(TT). When the spin coherence is lost, such as by the interference of an external magnetic field, the correlated triplet pair state will split into two individual triplet T_1 states. Figure adapted from Ref [1].

If the coupling between the chromophores is strong, the ^{1}(TT), ^{3}(TT) and the ^{5}(TT) states will not be degenerate and the effect of $\hat{H}_{sp}$ will be negligible. A pure spin state ^{1}(TT) will be formed. If ^{1}(TT) is a lot more stable than ^{3}(TT) and ^{5}(TT), it will be energetically difficult for the triplets to diffuse apart. Thus, in order to harvest two triplets for solar cell applications, the coupling between chromophores should not be too strong. However, it should also not be so weak that the rate of formation of the correlated triplet-pair state is too low for feasible application. The remaining of this dossier will refer to the correlated triplet pair state as the pure-spin state ^{1}(TT). To date, there is no agreement on the mechanism for the intersystem crossing process that converts $S_0 + S_1$ to ^{1}(TT).

2.2.2 Proposed Mechanisms

There are two main proposed mechanisms for the formation of the correlated triplet pair state ^{1}(TT), namely the CT and the direct method.

In the CT mechanism, the S_1 and S_0 gain cationic and anionic characteristics as represented in Figure 2.4 before forming ^{1}(TT). Since this process involves converting Frenkel singlet excitons to CT excitons, then back to Frenkel triplet excitons, it is likely

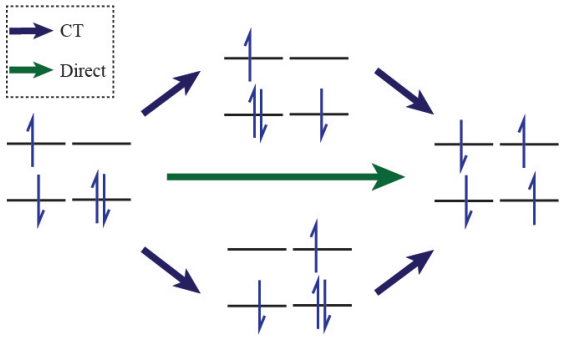

Figure 2.4: The green arrow depicts the direct mechanism where the S_1 and S_0 couple to form ^{1}(TT) directly. The blue arrows show the pathway of the S_1 and S_0 states gaining cationic and anionic characteristics before forming the ^{1}(TT).

that the coupling term $\hat{H}_{\text{Frenkel-CT}}$ mentioned in Section 2.1.1 is significant. In contrast, the direct mechanism is where S_1 and S_0 couple electronically to form ^{1}(TT) directly through an avoided crossing or conical intersection.

Monahan and Zhu argued in their review paper that CT is crucial for singlet fission. [49] For instance, Petelenz *et al.* reproduced the eigenenergies observed in the electroabsorption spectra of anthracene, tetracene and pentacene when they used a basis with Frenkel and CT contributions (∼2–27%) in their calculations. [50] Furthermore, calculations on Davydov splitting [b] required CT-Frenkel coupling to reproduce experimental observations in linear absorption spectra. [26, 52] Zhu *et al.* managed to observe the multiexciton intermediate via time-resolved two-photon photoemission spectroscopy and they observed that the multiexciton state is formed nearly simultaneously with the excited singlet state. [43] Theoretical calculations suggest that the short dephasing times of CT states can explain the ultrafast formation of the multiexciton state, suggesting that the excited singlet is coupled with the CT state. [53]

Nonetheless, Zimmerman *et al.* argued that the correlated-triplet pair is formed via direct mechanism, using calculations on tetracene and pentacene crystals, [54] in direct contrast with Petelenz's *et al.* work. [50] They calculated the potential energy

[b] Davydov splitting is the lost in degeneracy of electronic states as molecules in a crystal lattice have different orientations, leading to non-equivalent interaction energies with one another. [51]

surfaces of the singlets and triplets in tetracene and pentacene, and found a conical intersection. A conical intersection is caused by the strong vibronic coupling between the dimers (when fixed at certain geometries as in crystals) and it acts as a funnel to allow a direct conversion from $S_1 + S_0$ to ^{1}(TT). [55, 56] Recently, Musser *et al.* provided empirical evidence of the direct mechanism in singlet fission of TIPS-Pn [8] and their observed dynamics are consistent with dynamics calculations near conical intersections. [57] Burdett *et al.* also showed that the direct mechanism is a possible route for singlet fission to proceed because their theoretical model based on the direct mechanism successfully reproduced the delayed fluorescence spectra that they measured for crystalline tetracene. [44] Although there is yet to be a consensus, both the direct and CT mechanisms could play a role in singlet fission, and their contribution might depend on the system studied (e.g. endoergic or exoergic, intermolecular or intramolecular).

2.2.3 Existing Studies on Exciton Transport in Singlet Fission

To incorporate singlet fission with solar cell technology, the transport of the generated excitons needs to be better understood so that researchers can design singlet fission chromophores deliberately to improve their transport properties. One of the key challenges in this field is the difficulty in detecting and tracking excitons because their spectroscopic signals are easily drowned by signals from the ground state molecules, which are significantly more abundant. Thus, many studies on exciton transport were done computationally. [27, 58]

Samiullah *et al.* managed to overcome this problem by using photoinduced absorption spectroscopy, where they detected the quenching of photoluminescence signals of the ^{1}(TT) when they were absorbed by acceptor molecules. [59] They found that the diffusion of triplet excitons in thin films of diaryl (diphenyl)-substituted ladder-type poly(paraphenylene) can be described using the random walk model and the diffusion lengths and lifetimes of triplets were on the order of $\sim 1\,\mu$m and $\sim 10\,$ms. [59] Akselrod's *et al.* work also supported the random walk model. They used a home-built

fluorescence microscope to measure the delayed fluorescence released when the ^{1}(TT) of tetracene crystals recombined to become singlets. Their time-resolved and spatially-resolved technique not only demonstrated anisotropy in the diffusion axes, it also showed that nanoscale morphology, such as local exciton traps, has a huge impact on the diffusion rate. [60]

Nonetheless, these methods are indirect observations of exciton diffusion. Furthermore, a technique that depends on the recombination of ^{1}(TT) is non-ideal because recombination contradicts the goal to harvest multiple charge carriers from a single-photon input. In 2015, Wan *et al.* showed that they could observe the exciton transport in a single tetracene crystal directly through femtosecond transient absorption microscopy, with a spatial resolution of 50 nm and temporal resolution of 200 fs. [61] Similar to Akselrod's *et al.* work, they showed that triplet diffusion is more efficient in the b axis (defined by the crystallographic axes of tetracene crystals) whereas singlet diffusion is isotropic. They were able to distinguish singlets from triplets because the absorption spectra are observed at different delay times and the absorption bands are different. [61] They proposed that triplet-triplet recombination can be useful in that it helps maintain an equilibrium between the populations of singlet and triplet excitons, allowing for a long-range and relatively fast triplet exciton transport.

2.3 Femtosecond Stimulated Raman Spectroscopy

2.3.1 Spontaneous Raman Spectroscopy

Raman scattering was discovered by C.V. Raman and K.S. Krishnan in 1928 when they observed that the wavelengths of scattered light were different from the incident wavelength after the light was passed through a liquid sample. [62,63] This phenomenon was found to arise from vibrational modes of the molecules [64,65] and gave information about their molecular structures. [66,67]

When a photon with frequency ω_i interacts with a molecule, it can be scattered

either elastically or inelastically. Elastic scattering, also known as Rayleigh scattering, does not change the vibrational state of the molecule and the scattered photon has the same frequency ω_i. On the other hand, the vibrational state of the molecule either increases or decreases in inelastic scattering, also known as Stokes or Anti-Stokes Raman scattering, respectively. As shown in the Jablonski diagram in Figure 2.5, the difference in frequency of the scattered photon and the incident photon ω_i corresponds to the energy difference ω_0 between the initial and final vibrational states. [68]

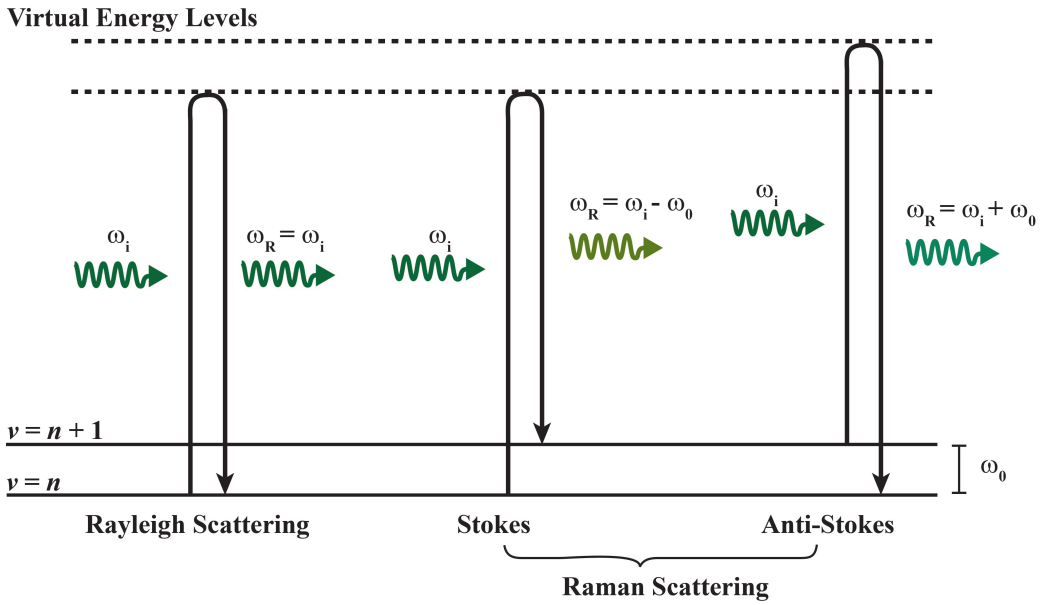

Figure 2.5: In scattering processes, the molecules are promoted to virtual energy levels after interaction with the photons. The virtual energy levels cannot be observed because the photons were not absorbed. The molecules then return to the ground state and release the scattered photons. In Rayleigh scattering, the scattered photon has the same energy as the incident photon and the molecule is still in the vibrational level n. In Raman scattering, the energy difference between the scattered photon and incident photon the energy difference between vibrational state n and $n+1$. The molecule will either be in a higher (Stokes) or lower (anti-Stokes) vibrational level after the scattering process.

Raman scattering can be optically observed only for vibrational or rotational modes that change the polarizability α of the molecule ($\frac{\partial \alpha}{\partial Q_i} \neq 0$); Q_i is a vibrational or

rotational coordinate. The polarizability is a measure of how easily a dipole can be induced in presence of an electric field, which is represented mathematically by

$$\tilde{\mu}_{\text{ind}} = \alpha \vec{E} \tag{2.12}$$

where $\vec{\mu}_{\text{ind}}$ is the induced dipole and $\vec{E}$ is the electric field responsible for this dipole moment.

The local electric field in a molecule fluctuates sinusoidally because the electronic motions are coupled to the much slower nuclear motions. Thus Equation 2.12 can be written as

$$\vec{\mu}_{\text{ind}} = \alpha_0 \vec{E} \cos \omega_i t + \frac{1}{2} \vec{E} Q_i \frac{\partial \alpha}{\partial Q_i} [\cos(\omega_i + \omega_R)t + \cos(\omega_i - \omega_R)t] \tag{2.13}$$

where ω_i is the frequency of the incident photon while ω_R is the frequency of the scattered Raman photon. As scattering probability, and hence Raman peak intensity, is proportional to the square of the induced dipole, only systems with a change in polarizability ($\frac{\partial \alpha}{\partial Q_i} \neq 0$) will have Raman signatures. The first term in Equation 2.13 can be neglected because it corresponds to Rayleigh scattering. [68]

The Raman shift, which is typically reported in wavenumbers (cm^{-1}), is defined by the difference in energy between the scattered and incident photons. As shown in Figure 2.5, anti-Stokes Raman scattering lowers the vibrational energy of the molecule. As a majority of the molecules are already in the lowest vibrational level under normal conditions, anti-Stokes feature intensity will be much lower than that of the corresponding Stokes feature. Therefore, for the rest of this dossier, Raman feature will refer to Stokes only.

2.3.2 Stimulated Raman Spectroscopy

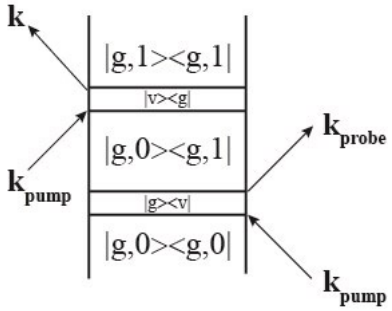

Figure 2.6: Double-sided Feynmann diagram of stimulated Raman process. [2] The first interaction with the Raman pump excites the ket <g,0| into a virtual state <v|, which is brought back to the ground state <g,1| by the Raman probe pulse. The Raman pump then comes in to promote the bra |g,0> to a virtual, and a photon is scattered out ($\vec{k}$) when the system returns to the ground state. The system is now in a higher vibrational state.

As spontaneous Raman scattering is a weak process ($\sim$1 scattered photon in every 10^7 incident photons), [69] one of the efforts to enhance the Raman signal is to utilize the stimulated emission process. Similar to spontaneous Raman, the system is promoted to a virtual state [c] by a Raman pump beam ($\vec{k}_{\text{pump}}$). However, instead of the system returning to the first excited vibrational state spontaneously, a probe beam ($\vec{k}_{\text{pr}}$) is used to stimulate the process, as shown in the Feynmann diagram in Figure 2.6. The scattered photon is scattered in the direction of $\vec{k}$, where

$$\vec{k} = \vec{k}_{\text{pump}} + \vec{k}_{\text{probe}} - \vec{k}_{\text{pump}} = \vec{k}_{\text{probe}}. \tag{2.14}$$

The scattered photon is coherent with the probe beam and all the Raman signal could be collected in the direction of the probe beam, as opposed to being scattered in all directions, as in spontaneous Raman scattering. This gives a much larger Raman signal for stimulated Raman spectroscopy as compared to spontaneous Raman spectroscopy.

[c] It is possible to excite the system to an existing electronic state, which would make this technique a hybrid between stimulated Raman and resonance Raman spectroscopy.

[69]

2.3.3 Principles Behind FSRS

Femtosecond stimulated Raman spectroscopy (FSRS) is an ultrafast technique that can measure the Raman spectra of excited states. The technique consists of three laser pulses – a femtosecond actinic or photoexcitation pump, a femtosecond Raman probe and picosecond Raman pump pulse. The Raman pump and probe pulses are spatially and temporally overlapped to maximize the stimulated Raman signal. The photoexcitation pump is also spatially overlapped with the other two beams so that the excitation site and probing site coincides.

When the photoexcitation pump interacts with the sample, it excites the molecules to a higher electronic level as shown in Figure 2.7. The time at which this occurs is defined as the zero time delay (t_0). The photoexcitation beam has a narrow bandwidth and its peak wavelength is tunable so that the experimental setup can be tailored to excite the system within a specific electronic transition. After a time delay t, the Raman pump and probe beams interact with the system to generate vibrational coherence. This contributes to the macroscopic polarizability of the system, represented as $|e, n\rangle \langle e, n+1|$, and the molecules would start oscillating between two vibrational states (Figure 2.7: Right). As the Raman pump lasts for a longer duration, it interacts with the system a second time to generate the scattered photons.

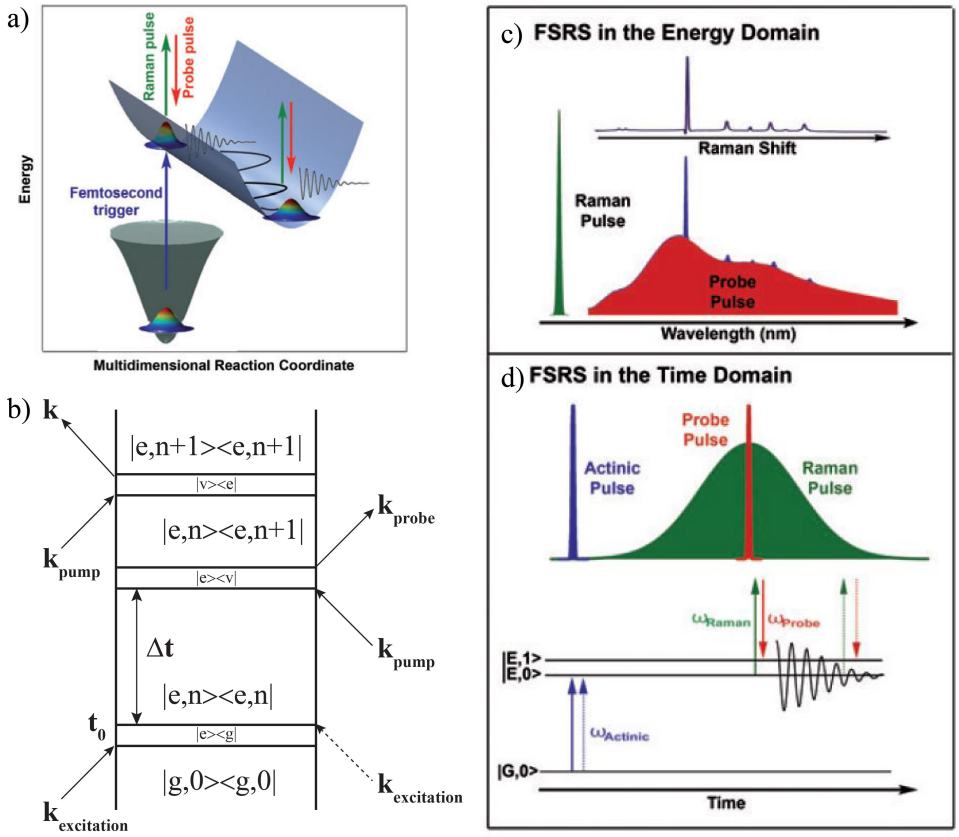

Figure 2.7: (a) A brief overview of the FSRS process, where the system decays across a multidimensional reaction coordinate after excitation. (b) Feynmann diagram for stimulated Raman scattering that incorporates the excitation of the molecule by the photoexcitation pump. The output ($\vec{k} = \vec{k}_{\text{probe}}$) is coherent with the Raman probe pulse. [3] (c) In the energy domain, the photoexcitation and Raman pump pulses have a narrow bandwidth while the probe pulse is a continuum. (d) In the time domain, the actinic pulse first excites the system. After a time delay, the Raman pump and probe pulses interact with the system to generate a vibrational coherence. As the Raman pump is broader in time, it will interact with the system a second time to generate a scattered photon. Image courtesy from Renee Frontiera. [4]

Based on the FSRS Feynmann diagram (Figure 2.7: Left bottom), $\vec{k} = \vec{k}_{\text{pump}} + \vec{k}_{\text{probe}} - \vec{k}_{\text{pump}} + \vec{k}_{\text{excitation}} - \vec{k}_{\text{excitation}} = \vec{k}_{\text{probe}}$, and the scattered photons are coherent with the Raman probe photons.

The probe beam and the scattered Raman photons are directed to a charge coupled

device (CCD) detector. The Raman signal is reported as a gain in the probe signal. To eliminate shot-to-shot fluctuations due to the instability of the Raman probe, the Raman gain is calculated using this equation: [3]

$$\text{Raman gain} = \frac{\text{Probe and signal counts with Raman pump on}}{\text{Probe and signal counts with Raman pump off}}. \tag{2.15}$$

In FSRS, the ground state spectrum is taken when the photoexcitation pump is off. After the photoexcitation pump has excited the molecules, the Raman spectra collected consist of the Raman spectra of both the ground state and excited state molecules. As only a minority of molecules will be in the excited states, the excited state spectra will be very weak. To extract these excited state spectra, the ground state spectrum is substracted from the Raman spectra collected at various time delays with respect to the photoexcitation pump.

FSRS is an ideal technique for studying singlet fission because it has many advantages. Besides having high temporal ($\sim 50 - 300\,\text{fs}$) resolution, that relies on the vibrational dephasing time of the molecular system, and high spectral ($\sim 10\,\text{cm}^{-1}$) resolution, [4, 70] FSRS also probes the Raman spectra of the excited singlet and triplet states directly instead of relying on signatures of accompanying processes such as the measurement of delayed fluorescence due to the recombination of triplets. [60] The relationship between the exciton transport and vibrational modes can then be studied directly. Raman peaks can be assigned very specifically to their corresponding vibrational modes whereas transient absorption (TA) bands are not easily assigned to certain electronic features. Furthermore, the FSRS setup itself allows the TA spectra to be recorded simultaneously. The absorbance can be calculated from the transmission of photons when the Raman pump is off, as shown in this equation:

$$\text{Absorbance} = -\log\left(\frac{\text{Probe counts with Photoexcitation pump on}}{\text{Probe counts with Photoexcitation pump off}}\right) \tag{2.16}$$

2.4 Experimental Setup

2.4.1 Femtosecond Stimulated Raman Spectroscopy

The FSRS setup consists of the Libra-HE laser system (Coherent Inc.) as the fundamental laser source. The output wavelength is centered at 800 nm with an output power of 4.6 W and repetition rate of 1 kHz. The schematic of the setup is shown in Figure 2.8. This primary laser beam is then split into three different pathways sending it through two 70:30 beam splitters.

The Raman pump (yellow pathway) is the first beam that is split off. It passes through a grating filter to narrow its bandwidth. This increases the pump pulse duration to 2.1 ps. [6] The Raman pump then passes through the time delay stage which can be adjusted to ensure that the Raman pump and probe pulses are temporally overlapped. A chopper that rotates at 0.5 kHz is used to chop the Raman pump so that the Raman pump can be on (when chopper is not blocking the beam) and off when chopper is blocking the beam).

The second beam used is the Raman probe beam (purple path). The laser pulse is sent through a sapphire crystal, which undergoes self-phase modulation, where the refractive index of the crystal changes for different wavelengths of light due to the optical Kerr effect. This leads to spectral broadening and generates a smooth white light continuum. The probe continuum is sent through a prism compressor to correct the chirp. As the Raman probe pulse has a wide range of wavelengths, its time duration is quite short following compression (approximately 30 fs).

The third beam (green path) goes through a non-collinear optical parametric amplifier (NOPA) to generate the photoexcitation pump. In the NOPA setup, the fundamental beam is further split into two beams; one is focused into a sapphire crystal to generate a continuum seed pulse while the other is sent through a doubling crystal (beta barium borate (BBO)) to generate a pump pulse at 400 nm. The seed and the pump pulses then converge at a BBO mixing crystal to amplify a portion of the continuum

and generate the photoexcitation pump. The wavelength of the photoexcitation pump can be tuned from 500 nm to 700 nm. The photoexcitation beam can be blocked or unblocked by turning a programmed shutter on or off.

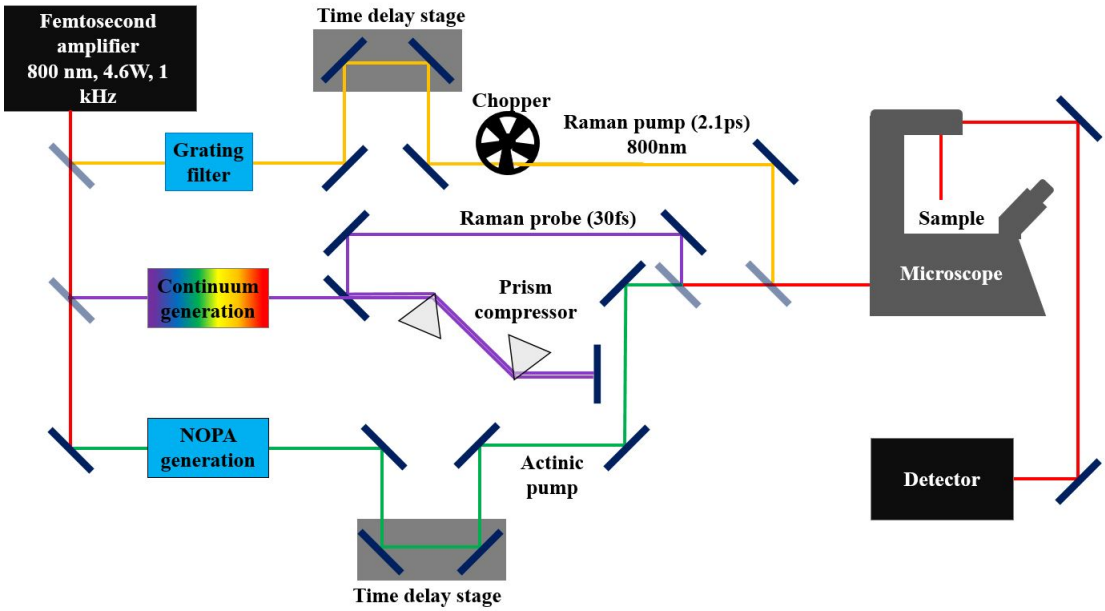

Figure 2.8: Schemtic of FSRS setup. The fundamental 800 nm, 4.6 W laser beam is split off to three different beams – Raman pump beam (yellow path), Raman probe beam (purple path) and photoexcitation pump beam (green path). They converge before entering the microscope, as represented by the red laser beam path. The dark blue rectangles are reflective mirrors and the pale blue rectangles are 70:30 beam splitters. [5, 6]

As shown in Figure 2.8, the Raman pump, probe and photoexcitation pump converge and are passed through the inverted microscope to the sample. All three beams are *p*-polarized with respect to the sample. The laser beams are focused onto the sample through a microscope setup. The collimated output, which consists of the probe photons and the coherent scattered Raman photons, is directed from the microscope to the detector.

Before conducting the experiment, all three beams need to be spatially and temporally aligned. The spatial and temporal overlap between the Raman pump and Raman

probe can be found by maximizing the Raman signal of cyclohexane, a common standard for calibrating Raman frequencies. The photoexcitation pump can be spatially overlapped with the Raman beams visually by viewing the image from the microscope's camera. The temporal overlap between the photoexcitation pump and the Raman probe is determined by finding the position of the time delay stage at t_0.

2.4.2 Finding Zero Time Delay t_0

The time at which the photoexcitation pump interacts with the sample is assigned as t_0, while the times before and after this interaction are the negative and positive time points respectively. The time delays between the Raman pulses and the photoexcitation pump are determined by the position of the time delay stage (along green path in Figure 2.8).

To find t_0, the cross-correlation between the photoexcitation pump and Raman probe is found using the optical Kerr effect, which accounts for the convolution or degree of overlap between the two beams. These two beams interact with the sample before they are directed to a photodiode instead of the detector. The sample the beams are passing through is usually cyclohexane because of its high Kerr constant.

A polarizer is placed before the photodiode to allow only *s*-polarized light to pass through and the polarization of the photoexcitation pump is circularly polarized as it goes through a quarter wave plate. When the photoexcitation pump passes through the sample, the electric field component of the beam changes the refractive index of the medium due to the optical Kerr effect. When the probe passes through the sample in absence of the photoexcitation pump, it leaves *p*-polarized and is not be detected by the photodiode. However, in the presence of the photoexcitation pump, the induced birefringence within the sample will cause the polarization of the Raman probe to have a *s*-component, which will be picked up by the photodiode. The full-width at half maximum (FWHM) of the cross-correlation curve gives the smallest time delay difference that can be resolved between the pulses (not the same as time resolution), while the

peak position gives the position of the time delay stage where t= 0 fs. The t_0 found with cyclohexane might be different for the TIPS-pn crystals due to differences in the refractive index and sample thickness.

2.4.3 Spatially-Offset FSRS

To study the dynamics of singlet fission, spatially-offset FSRS spectra are measured by displacing the photoexcitation beam away from the Raman pump and probe. Therefore, the excitation site and probing site are at a known distance from each other. The photoexcitation beam is displaced because it is non-trivial to shift both the Raman pump and probe without changing their overlap. Moreover, the alignment from the microscope to the detector is based on the Raman probe beam pathway, and changing the probe position would misalign the setup.

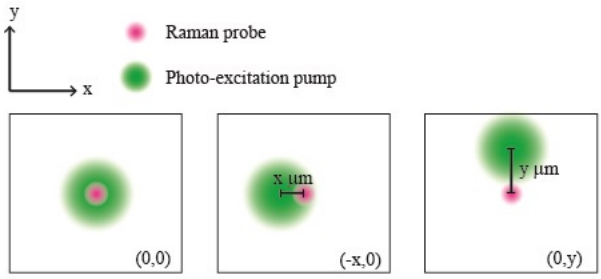

Figure 2.9: Spatial-Offset

The spatial offset is defined as the distance between the center of the probe beam and the center of the photoexcitation beam. The spatial offset is assigned values on the x and y axes as shown in Figure 2.9, with units in microns. The axes are arbitrarily assigned as the horizontal and vertical axes of the images collected from the microscope. Based on the image collected by the microscope camera, the estimates of the beam diameters are 2 μm and 10 μm for the Raman probe and photoexcitation beams respectively. The spot size of the photoexcitation pump is larger because its focal point is slightly different than that of the probe beam. As a result, the photoexcitation pump is more dispersed

and can excite a wider region of molecules. The Raman probe and photoexcitation beams are assumed to have 2D Gaussian profiles, and the degree of overlap between them can be calculated by integrating the volumes under their curves numerically.

2.5 Isolating Stimulated Raman Features from Other Four-Wave Mixing Processes

One difficulty constantly encountered in interpreting FSR spectra is that Raman features may be difficult to distinguish from other four-wave mixing processes, such as transient absorption features or cross-phase modulation. Thus, to counter this problem, I worked with other lab members to develop dual-frequency Raman pump FSRS, inspired by shifted excitation Raman difference spectroscopy (SERDS). Our work has been published in the Journal of Physical Chemistry A, where my main contributions were setting the technique experimentally and writing the algorithm used to reconstruct a background free Raman spectra. The following paragraphs have been adapted with permission from reference [71]. Copyright 2019 American Chemical Society.

Our goal was to present a new and effective method to distinguish transient Raman peaks from other nonlinear spectral features in FSRS using a SERDS inspired technique with minimal complexity and no moving parts. SERDS is based on the principle that Raman features are excitation frequency dependent, whereas fluorescence spectra are independent of slight changes in excitation frequency. Therefore, small changes in the excitation wavelength result in equivalent shifts of the Raman peaks, whereas the fluorescence background remains unchanged. [72–79] By subtracting Raman spectra obtained with two different but close in frequency ($\sim$5-10 cm^{-1}) excitation wavelengths, dispersive-shaped Raman features are obtained and all other spectral contributions such as fluorescence [77,80] are removed from the wavelength-dependent Raman peaks. [81] A background-free Raman spectrum can then be recovered using curve fitting and integration algorithms. [72,74,77,78,81–86] The choice of reconstruction method is application

dependent and can range from being relatively simple to complicated integration algorithms requiring user intervention to manually specify the limits. [77, 82, 87]

To more easily produce simultaneous yet spectrally different Raman pump pulses for a SERDS-inspired approach to FSRS, we took inspiration from the work of Kearns et al., who built a simple frequency comb generation setup for vibrational sum frequency generation (VSFG) experiments. [83] To collect two different VSFG spectra simultaneously, Kearns et al. used a pair of mirrors to divide the Ti:Sapphire fundamental output into two visible beams in a grating filter. [83] This simple addition of two mirrors in the grating filter produced two visible pulses that were spectrally separated but spatially and temporally overlapped resulting in two different VSFG signals for multiplex detection. Given that a standard FSRS approach uses a grating filter to generate the picosecond Raman pump pulse, we utilize a similar design here.

To generate the dual-frequency Raman pump, we passed 460 mW of the 800 nm fundamental output through our home-built grating filter to generate a 2.1 ps narrowband Raman pump. [3] In our grating filter, the fundamental diffracts off a grating and is then focused onto a slit with a cylindrical lens, which selects a portion of the input bandwidth to be reflected back through the lens to the diffraction grating. To generate two Raman pump pulses, we inserted a 1 mm thick rectangular silver mirror, shown in bold inside the red dotted box in Figure 2.10a, after the focusing lens, which reflects the red portion of the dispersed input bandwidth onto a second slit and mirror. We used the second slit to select a portion of this spectral bandwidth to generate the second Raman pump pulse, which is reflected back through the lens to the grating, as shown in Figure 2.10a. We collected the combined reflections from both mirrors after the grating with a D-shaped pickoff mirror. The output beam consisted of two narrowband pulses separated in wavelength by 1.6–3.0 nm. The two Raman pump pulses are overlapped in space and time at the sample. We mounted the slits on translational stages to adjust the frequencies required for the two Raman pump pulses. This allows us to switch between the two Raman pump wavelengths without changing any other

experimental parameters. Figure 2.10b illustrates the fundamental principle of SERDS, in which Raman features are shifted by known frequencies relative to the two excitation wavelengths and non-Raman features overlap.

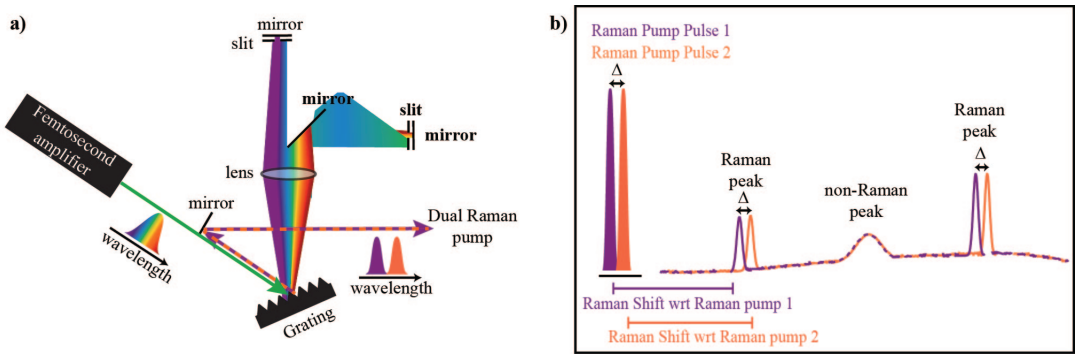

Figure 2.10: (a) Diagram of the modified grating filter setup to generate Raman pump pulses at two wavelengths. A mirror, indicated by the red dashed box, is added to send half of the diffracted light to another mirror–slit pair to generate the second Raman pump pulse. (b) Schematic explaining the principle of SERDS, where the Raman signals shift in frequency upon a shift in the Raman pump excitation wavelength, and the non-Raman signals remain unchanged.

To demonstrate that dual-frequency Raman pump FSRS can discriminate Raman peaks from non-Raman peaks and background spectra, we first used this setup to measure the ground-state stimulated Raman spectra of cyclohexane. As cyclohexane is a well-known Raman standard, we were able to verify if our technique could effectively isolate Raman peaks from the other signals. We converted the stimulated Raman spectra of cyclohexane taken separately with the Raman pump pulses at 803.1 nm and 806.1 nm to a common scale through z-normalization [77] so as to make their background spectra similar in Figure 2.11a. Based on the 3 nm difference between the two Raman pump frequencies, the Raman signals taken with the 806.1 nm Raman pump should be upshifted by 46 cm^{-1} (Δ) with respect to the Raman signals taken with the 803.1 nm Raman pump. Comparing the two spectra in Figure 2.11a, we observe that the frequencies of the six Raman peaks of cyclohexane shift by the expected amount. We can also confirm that the two peaks observed in the 600-800 cm^{-1} region are not Raman peaks

as they are independent of the Raman pump wavelength. These non-Raman peaks are likely signatures of cross-phase modulation between the Raman pump and probe pulses.

To reconstruct a background-free cyclohexane Raman spectra, we first subtracted the z-normalized Raman spectra from one another to obtain a difference spectrum *D(v)* and plotted it with respect to the 803.1 nm Raman pump pulse (Figure 2.11b). If the backgrounds of the 803.1 nm and 806.1 nm Raman spectra are identical, *D(v)* will eliminate the background contribution entirely and leave behind Raman peaks that appear as derivative-like features. However, we see that *D(v)* still bears a non-vanishing background likely derived from differences in the cross-phase modulation of the two Raman pump pulses. Next, we fit the difference spectrum *D(v)* from its ith index point to its *(i+n)*th index point to a pair of Gaussian functions shifted by Δ:

$$f(v) = A_1 \left(e^{\frac{-(v-v_0)^2}{2c^2}} - A_0 e^{\frac{-(v-v_0-\Delta)^2}{2c^2}} \right) + v_1 \tag{2.17}$$

where A_0 is the scaling factor (A_2/A_1), A_1 and A_2 are the amplitudes of the positive and negative Gaussian functions in the difference spectrum, v is the wavenumber, v_0 is the peak center of the positive Gaussian peak in wavenumbers, Δ is the SERDS shift, c is the standard deviation and v_1 is the baseline. The positive and negative Gaussian peaks correspond to peaks in the 803.1 nm and 806.1 nm Raman spectra in this case.

We fit across the entire difference spectrum with $f(v)$ using a range of $n = 150$ points and the following constraints: 1) both the positive and negative Gaussian peaks have the same FWHM, 2) the FWHM cannot be higher than 50 cm^{-1}, 3) the peak position $v0$ is fixed at the v value in the middle of the fitting range, and 4) A_0 and Δ values are determined from experimental conditions and held constant throughout the fit.

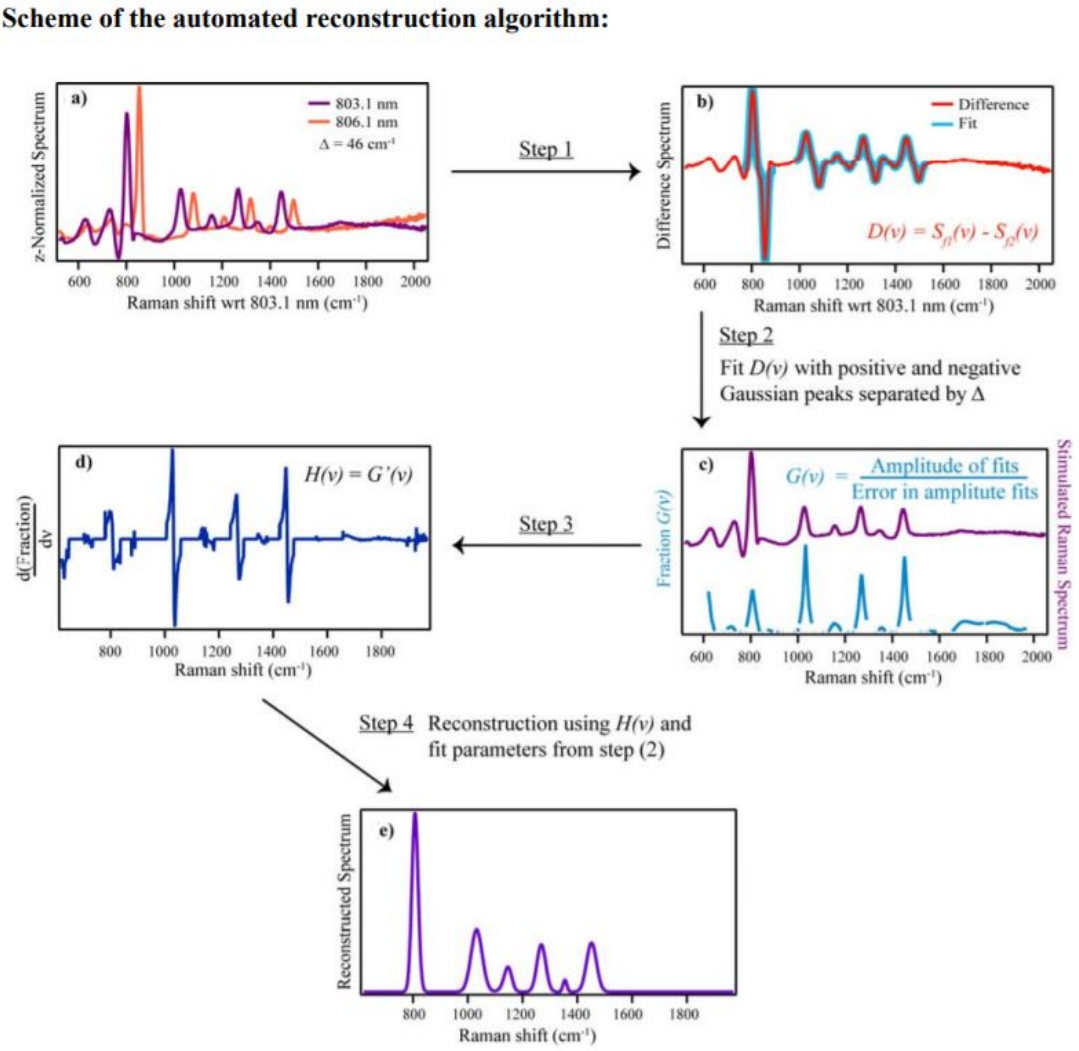

Figure 2.11: Scheme of the automated reconstruction algorithm. (a) z-normalized Raman spectra of cyclohexane at Raman pump frequencies of 803.1 nm and 806.1 nm. (b) Fit the difference spectrum $D(v)$ to a pair of positive and negative Gaussian peaks. Examples of the fit functions (blue) at the Raman peak positions. (c) Measured the ratio of the amplitude of the fits in (b) to the error in the fits and obtained Fraction $G(v)$. (d) Used an algorithm to process $H(v)$, the derivative of $G(v)$, to identify the Raman peak positions. (e) Reconstructed Raman spectrum from plotting sum of Gaussian functions with the fit parameters corresponding to the peaks identified in (d).

A_0 is set as the ratio of the output power of the two Raman pump pulses, while Δ is the difference in frequencies of the two Raman pump pulses. We chose $n = 150$ because its range covers each Raman peak function with little to no overlap with the subsequent Raman peaks in cyclohexane. In our constraints, we assumed that the FWHM of the two peaks are the same because they arise from the same cyclohexane sample under very similar experimental conditions. We set the upper limit of the FWHM to be 50 cm^{-1} because we noted that the FWHM of the Raman peaks were less than 30 cm^{-1} in the initial Raman spectra shown in Figure 2.11a. We fixed v_0 to the center of the fitting range so that we account for all possible peak positions. As a result, we only needed to extract the amplitude A_1 and FWHM of the Raman peaks from our fitting algorithm.

After we fit the difference spectrum with $f(v)$, we obtained the amplitude A_1 of the fits at each point across the entire spectrum. We then divided the amplitude of the fits A_1 by its error at each point in the spectrum, which we denote as fraction $G(v)$ and overlaid it with the 803.1 nm Raman spectrum in Figure 2.11c. Due to the constraints imposed in our fitting algorithm, we expect good fits only when v_0 coincides with a Raman peak position. At all other positions with no Raman peaks, the fit amplitudes would have large errors and thus $G(v)$ approaches zero. We can see in Figure 2.11c that the resulting $G(v)$ spikes at regions with Raman signal, very clearly highlighting the Raman peak positions. Next, we took the derivative of fraction $G(v)$, referred to as $H(v)$, shown in Figure 2.11d, and ran the following algorithm to search for the exact positions of the Raman peaks. In order to be considered the position of a Raman peak, the mth point of $H(v)$ must meet these two criteria:

a. $H(m) > 0$ and $H(m+1) < 0$, representing a peak in $G(v)$ where its slope changes sign.

b. $\Sigma_{m-p}^{m} H(v)$ is larger than a *threshold* value, where p is the number of points prior to the inflection point, to eliminate any oscillatory noise.

For all m that fulfilled these criteria, we retrieved the fit parameters of the difference spectrum $D(v)$ and computed the corresponding Gaussian functions. The reconstructed

spectrum is a sum of all of these Gaussian functions, that produces a background-free spectrum. We used $p = 10$ and threshold $= 1.4$ for the automated reconstructed cyclohexane Raman spectrum in Figure 2.11e.

We have also applied this experimental approach and automated data analysis technique to time-resolved studies. The introduction of the photoexcitation pulse can give rise to more non-Raman signals, such as a strong transient absorption background, which can make it more challenging to resolve Raman features associated with excited-state dynamics. Thus, having a technique that can reliably help to distinguish Raman features from non-Raman features is a big improvement.

In summary, by adding a second arm to our grating filter, we have developed this technique, which we call 'dual-frequency Raman pump FSRS' to obtain ground- and excited-state Raman data. We have also developed an automated reconstruction method to distinguish Raman features from background features in transient FSR spectra. Although our technique does not remove all scientific evaluation needed in interpreting FSRS spectra, it serves as a valuable tool to help decipher complex FSRS data, widening the range of systems we can understand through FSRS. This work provides insights into how a simple and economical approach is capable in removing unwanted non-Raman effects from Raman spectra in spontaneous and time-resolved Raman spectroscopy.

2.6 Conclusion

In this chapter, I laid the theoretical groundwork for exciton transport and FSRS. I also covered how FSRS and SO-FSRS are ideal techniques to study charge generation and transport mechanisms in singlet fission, a process that has huge potentials in photovoltaic applications. I also discussed dual-frequency Raman pump FSRS, a complementary tool that can help us distinguish Raman features from other four-wave mixing processes in SO-FSR spectra.

Chapter 3

Advancements in Singlet Fission Chromophore Design Enabled by Vibrational Spectroscopies

To date, there have been many reviews and perspectives published on singlet fission, covering a wide range of topics such as the nature of the correlated triplet pair and computational methods. However, none has directly placed the spotlight on the spectroscopic techniques used to study singlet fission. Spectroscopic techniques can be broadly classified as electronic, vibrational and magnetic in nature and each of them provides us with a unique lens to study singlet fission. Our understanding of singlet fission progresses with improvements in our collective toolkit, thus Dr. Kajari Bera and I published a singlet fission perspective as co-first authors to highlight the importance of various experimental techniques and specifically focus on advances in singlet fission driven by vibrational spectroscopic techniques. The full text of the perspective has been reproduced in this chapter. Reprinted with permission from reference [88]. Copyright 2020 American Chemical Society.

3.1 Overview

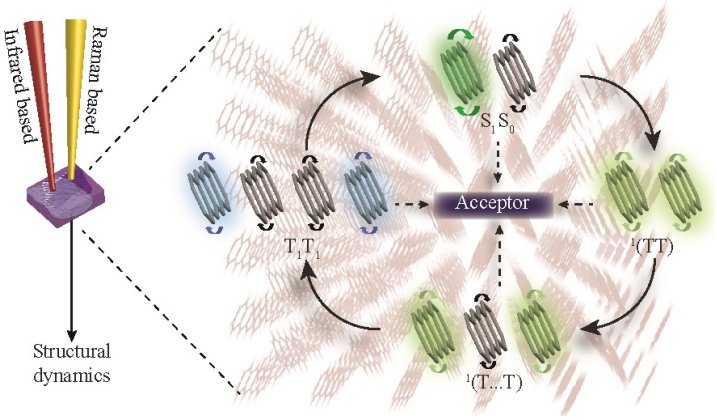

Figure 3.1: Vibrational spectroscopies drive advances in singlet fission.

Singlet fission leads to the formation of two separate triplet T_1 excitons from an initial singlet S_1 exciton through ^{1}(TT) and ^{1}(T...T), multiexcitonic intermediates that retain singlet character. Its ability to achieve external quantum efficiencies higher than 100% made it an attractive candidate for optoelectronic device applications. However, singlet fission has not been applied widely despite having been investigated by a myriad of spectroscopic methods, in part due to our poor understanding of how to optimize molecular structure and packing in chromophores well-suited to large-scale production. Vibrational spectroscopies provide a solution, because they directly probe nuclear motions, allowing us to monitor evolving structural changes in molecules undergoing singlet fission, thus providing us with roadmaps to design molecules suitable for optoelectronic applications. This Perspective reviews the contributions and analyzes the future directions of vibrational spectroscopies to the advancement in our knowledge about the mechanisms and rational designing of chromophores undergoing efficient singlet fission.

3.2 Introduction

Singlet fission (SF), a photophysical process where an initially excited singlet state S_1 evolves into two low-lying triplet states T_1, has been shown to attain external quantum efficiencies higher than 100% in photovoltaic devices. [15] Although this phenomenon had first been observed in the early 1960s [89, 90] and known to have potential to overcome the Shockley-Queisser limit, [14,91] it only regained interest in the past decade after it was shown to be feasible in wider classes of molecules, [92] including dimers, [93] showing promise for future applications in photovoltaics and photocatalytic processes. However, working solar cells based on SF have delivered a maximum power conversion efficiency of only 5.1% as opposed to the theoretical limit of 45%. [94] Some challenges to improve efficiency include poor environmental stability and high energy losses during charge generation and transport in the currently known classes of SF chromophores. Therefore, we need rational design principles to develop SF materials that are capable of achieving the power conversion efficiency much closer to the theoretical limit.

Following light absorption, SF is generally accepted as a three-step process that involves the formation of two intermediates

$$S_1 + S_0 \longrightarrow {}^1(TT) \longrightarrow {}^1(T\cdots T) \longrightarrow T_1 + T_1 \tag{3.1}$$

where both ^{1}(TT) and ^{1}(T...T) are multiexcitonic intermediates that retain singlet character, making SF a spin-allowed process. The correlated triplet pair, ^{1}(TT), consists of two excited triplet states that are electronically coupled and spincorrelated. When ^{1}(TT) loses its electronic coupling but still retains its spin coherence, it forms ^{1}(T...T), the separated correlated triplet pair. Eventually, ^{1}(T...T) loses its spin coherence to generate two individual triplet states T_1, which can be harvested for optoelectronic applications. Spatial separation of triplets in the ^{1}(TT) state followed by decoherence has been suggested as a pathway to form the electronically decoupled triplets. [45,46,95] The detailed mechanism of SF dynamics, and the electronic energetics and molecular

packing and coupling requirements for chromophores to undergo efficient SF, have been covered by many reviews over the past decade. [1, 45, 95–100]

The major hindrance to the optimization of SF-based photovoltaics is the scarcity of known molecules undergoing efficient SF that are photochemically stable, solution processable, and oriented in the correct geometries in their crystalline forms. The most commonly studied SF chromophores are acenes and their derivatives, although carotenoids and polymers have also been investigated for their SF properties. [100] However, identifying new classes of molecules capable of undergoing SF is challenging in part due to the limited knowledge about material design principles, such as modifying existing molecules for desired crystal packing structure and ideal chemical substituents, for chromophores undergoing near-unity SF efficiency. Additionally, the photophysics of the SF mechanism is not fully understood and is widely debated: whether the generation of ^{1}(TT) from S_1 follows a direct mechanism – where the S_1 state couples with a neighboring S_0 state to directly form ^{1}(TT) with no observable intermediates [8, 101] or a charge-transfer mediated mechanism where an observable charge-transfer intermediate is formed before it generates ^{1} (TT). [49, 52] Thus, the limited number of SF chromophores compounded with the complex convolution of the spin dynamics and the interactions between the electronic and vibrational states during SF makes it difficult to achieve consensus on a generic SF theory and molecular design principles. A promising approach would be to determine how exactly nuclear coordinates impact the mechanism and yield of SF, and thus, vibrational spectroscopies lead to advances in the SF field by probing structural changes following light absorption. This Perspective emphasizes the unique contributions and strengths of vibrational techniques to enhance our understanding of the designing principles for SF-based chromophores.

Historically, SF has been examined through a combination of electronic, photoemission, magnetic, and computational techniques. Ultrafast vibrational techniques are a relatively recent addition to the experimental toolbox for investigating SF. Currently,

these techniques include time-resolved midinfrared and infrared (IR) spectroscopy, resonance Raman (RR) spectroscopy, impulsive stimulated Raman spectroscopy (ISRS), and femtosecond stimulated Raman spectroscopy (FSRS). Since vibrational motions are determined by the interplay of the nuclear coordinates and are highly sensitive to local environments, vibrational spectral features, such as bandwidth, frequencies, and intensity, evolve as the molecules transit from the S_0 state to the S_1, ^{1}(TT), ^{1}(T...T), and T_1 states. This sensitivity of the molecular vibrations to their local environment provides a unique way to investigate the influence of molecular structure and morphology on the processes that occur within the system during the different steps in SF. This can give vibrational techniques an edge over electronic spectroscopies for studying SF, because electronic features tend to be broad and overlapped due to the isoenergetic nature of the excitonic states and the existence of an equilibrium between them. Time-resolved vibrational spectroscopies are particularly powerful tools to study photochemical and photophysical processes, because they can directly determine the nuclear motions driving SF and hence provide unique information about the structure, dynamics, and properties of short-lived species. A better understanding of the molecular structural changes will in turn guide the strategic design of SF materials for efficient photovoltaic systems.

In this Perspective, we review the significant contributions of vibrational spectroscopies to our understanding of the SF process, with a focus on translating mechanistic insight into practical design considerations for new chromophores. We describe key examples from the literature, starting with acene studies using IR and mid-IR time-resolved spectroscopy, followed by detailing the importance and role of vibronic coherence in SF, and then moving through Raman-based studies, which helped in formulating design guidelines for efficient SF chromophores. We conclude with comments on promising future applications of vibrational spectroscopy to guide SF materials design, including magneto-vibrational spectroscopies, terahertz approaches, and microscopic techniques to map vibrational contributions to exciton transport.

Before we detail the specific contributions vibrational spectroscopies have made in

understanding SF, we briefly describe the key highlights from electronic, magnetic, and computational studies. Electronic spectroscopies such as timeresolved photoluminescence (TR-PL), transient absorption (TA), two-dimensional electronic spectroscopy (2DES), and time-resolved two-photon photoemission (TR-2PPE) have been used to study SF. TR-PL provides information about the bright states, [102] TA can probe both bright and dark states, [55, 103, 104] 2DES identifies quantum coherent superposition of electronic states and couplings, [105] and TR-2PPE provides the energies of the excitonic states during the SF process. [43,106] In addition to the optical techniques, the magnetic field-based techniques, such as time-resolved electron paramagnetic resonance (TREPR), provide insights about the spin dephasing and the triplet and quintet states involved during SF. [107, 108] While each technique is specific in the information it can provide, all techniques complement each other and support each other to unravel the complex and complicated view of the SF process.

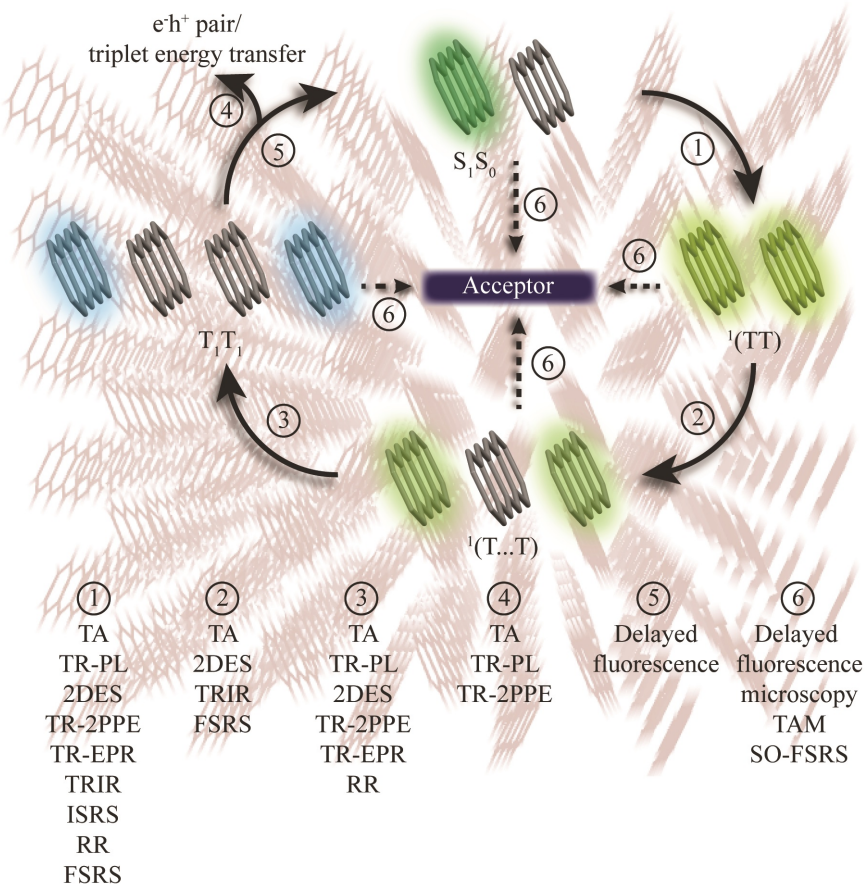

Figure 3.2: Schematic depicting SF and the spectroscopic techniques that have been applied to understand the corresponding steps in the process. (1) Formation of the correlated triplet pair that retains an overall singlet character. (2) Formation of the ^{1}(T...T) state after the correlated triplet pair loses its electronic coherence. (3) Formation of the individual triplet states after the ^{1}(T...T) loses its spin coherence. (4) Generation of free electron and hole charge carriers after the triplets are harvested at an acceptor substrate. (5) Triplettriplet annihilation to form singlet states. (6) Exciton transport within the crystal or film so that the excited states can eventually reach an acceptor substrate. Acronyms: TA transient absorption. TR-PL time-resolved photoluminescence. TR-2PPE time-resolved twophoton photoemission. 2DES two-dimensional electronic spectroscopy. TR-EPR time-resolved electron paramagnetic resonance. TRIR time-resolved infrared spectroscopy. ISRS impulsive stimulated Raman spectroscopy. RR resonance Raman spectroscopy. FSRS femtosecond stimulated Raman spectroscopy. TAM transient absorption microscopy. SO-FSRS spatially offset FSRS. A list of references corresponding to each step and technique is summarized in the Supporting Information.

In Figure 3.2, we summarized how each experimental technique has guided our knowledge about the mechanisms and energetics of each step in the SF process, from the generation of the ^{1}(TT) state to the harvesting of triplets. Step 1 refers to the formation of ^{1}(TT) from S_1. As this step is easily photoinitiated, it has been characterized by a wide range of electronic, magnetic, and vibrational techniques. Step 2 refers to the separation of ^{1}(TT) to form ^{1}(T...T). Our understanding of ^{1}(T...T) as a distinct intermediate is relatively recent, and thus this step of the SF process has only been studied by TA, 2DES, TRIR, and FSRS. As slight changes in the molecular structure, such as rotation or torsion across a bond, can occur during the formations of ^{1}(TT) and ^{1}(T...T), TRIR and FSRS are sensitive enough to pick up shifts in the local environment of the nuclear motions, making them suitable to study the mechanisms of steps 1 and 2. The limiting factor in probing the ^{1}(T...T) state is that it has similar spectral features to those of ^{1}(TT), making it challenging to distinguish them from one another. Step 3 refers to the formation of individual triplets T1 and is the second most commonly studied step, because SF is not considered complete until individual triplets are formed. After the individual triplets are formed, they can either be harvested by triplet energy transfer or electron hole pair generation (step 4) or undergo triplettriplet annihilation to reform the excited singlet S_1 or hot S_0 states (step 5). Step 4 requires the presence of an acceptor material and has only been studied by TA, TR-PL, and TR2PPE. Meanwhile, step 5 has only been studied by delayed fluorescence, which specifically probes the fluorescence of the singlets formed by triplettriplet annihilation. Step 6 refers to the movement of singlet and triplet excitons toward an acceptor material, where these photoinduced charged species can be harvested, and it can occur simultaneously with all other steps of SF. Although exciton transport is not a process unique to SF, understanding and improving the efficiency of the exciton movement is crucial for SF-based optoelectronic applications. Currently, FSRS and TRIR have yet to be utilized for steps 3 and 4, not because they are incapable of probing those processes, but because they have traditionally not been used to study processes that last for nano- or microseconds.

If equipped with time delay stages that probe into the time scales where steps 3 and 4 occur, FSRS and TRIR can be as versatile as TA. We compiled a comprehensive list of literature from year 2000 onward in the Supporting Information, which provides references for the studies and their corresponding techniques used to examine each step in the SF process.

Besides the experimental techniques, computational studies also help us interpret complex experimental results, predict what molecules can undergo SF, and investigate the role of a molecular structure in facilitating SF as detailed in these reviews. [109,110] For example, Morrison et al. found that the strong coupling of intramolecular modes in the range of $1400 - 1600$ cm^{-1} to the $S_1 \rightarrow {}^1(TT)$ transition helped to explain the temperature independence of SF rates in tetracene. [111] In another study, Shizu et al. found that twisting between tetracene dimers led to stronger vibronic coupling, which in turn led to higher rates of formation of ${}^1(TT)$. [112] These computational studies highlight the importance of understanding the roles of molecular structure and vibrations in facilitating SF, advocating for more experimental probes into the structural evolution of molecules during SF.

3.3 Structural Dynamics during Singlet Fission

3.3.1 IR-Based Techniques

Time-resolved IR spectroscopy can be used to monitor the structural changes within molecules by tracking the vibrational features that are sensitive to the identity of electronic states. Ultrafast TRIR has been used to study the dynamics of the intermediates ${}^1(TT)$ and ${}^1(T...T)$ formed during SF in a variety of acenes such as hexacene, 6,13-bis(triisopropylsilylethynyl) (TIPS)-pentacene, tetracene derivatives, and xanthene-based dimers. By probing transient structures with molecular specificity, TRIR has been used to identify structural intermediates, as well as distinguish between direct and mediated SF mechanisms.

To examine the structural dynamics of the intermediate electronic states in SF, Deng et al. used femtosecond transient infrared (fsIR) spectroscopy to observe unique vibrational signatures corresponding to S_1 and ^{1}(TT) states in addition to a transient spectral evolution of the ring-stretching modes of hexacene at $\sim$1600 cm^{-1}. [113] Complementing their experimental results with ab initio calculations, they identified the reaction coordinate and learned that the direct $S_1 \rightarrow$ ^{1}(TT) transition is predominantly driven by a few ring-stretching normal modes around 1600 cm^1. This novel study provides insights into the specific nuclear motions that drive the evolution of the excited-state potential energy surface during SF in hexacene.

In addition to identifying the vibrational motions that result in shuttling the molecules into the ^{1}(TT) states, mid-IR transient absorption has also provided insights into the much debated one-step or two-step mediated mechanism for the formation of ^{1}(TT) during SF. For the efficient harvesting of ^{1}(TT), it is necessary to examine the dynamics of its formation during the SF process. However, because of spectral overlap between the ^{1}(TT) and the separated triplets, it is challenging to study the dynamics unique to that of the ^{1}(TT) intermediate. To address this, Chen et al. employed ultrafast mid-IR spectroscopy to characterize the spectral features of the ^{1}(TT) state in a covalently linked slip-stacked terrylene3,4:11,12-bis(dicarboximide) (TDI) dimers. [114] Their fsIR spectroscopy results identified the spectral feature of ^{1}(TT), which displayed some characters of the T_1 and charge transfer states in the carbonyl stretch and the C=C stretch regions, respectively. The simultaneous presence of vibrational characteristics of both the triplet and charge transfer states indicated the formation of ^{1}(TT) in TDI dimers via a chargetransfer-mediated SF process. In a similar study, Margulies et al. used time-resolved spectroscopy in the vis-NIR (NIR = near-infrared) and IR regions to elucidate the effect of chemical substituents on SF in a series of cyano-substituted tetracenes. [115] They observed distinct vibrational frequencies for the CN stretch mode in the singlet and triplet states. By monitoring the dynamics of the vibrational band of the cyano group (CN), they found evidence of charge transfer species mediating ^{1}(TT) formation

in one system. Therefore, these vibrational dynamical studies suggest the first step in SF is the charge-transfer-mediated mechanism of ^{1}(TT) formation as opposed to the direct mechanism. The direct observation of a charge transfer intermediate using vibrational spectroscopies highlights the role of the two-step charge transfer mechanism for efficient SF. These investigations demonstrate that the distinct narrow vibrational features are sensitive to the electronic states of the chromophores and can be used to assign the dynamics corresponding to each electronic state, unique to vibrational spectroscopy.

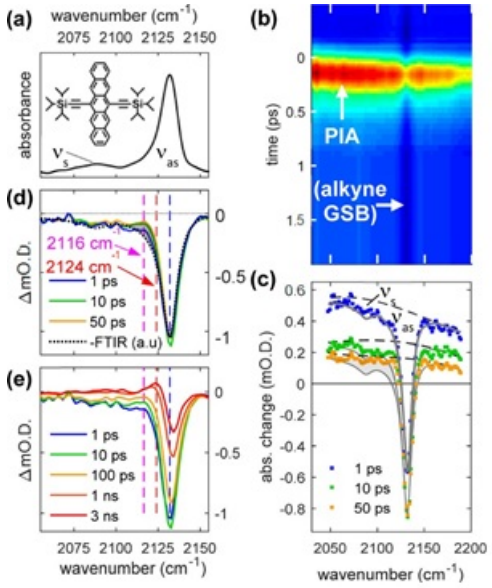

Figure 3.3: (a) Molecular structure and FTIR spectrum of the alkyne stretch mode in TIPS-pentacene thin films. (b) Mid-IR transient absorption spectra after photoexciting to the S1 state. Ground-state bleach (GSB) and photoinduced absorption (PIA) resulting from correlated triplet pairs intermediates. (c) Spectral slices from (b) at various time intervals highlighting the alkyne stretch mode and broad photoinduced absorption from correlated triplet pairs. (d) Background-subtracted data from (c), where marked arrows correspond to the vibrational features of the triplet excitons (2116 cm^{-1}) and hot ground-state (S_0*) molecules (2124 cm^{-1}). (e) Transient plots at longer time delays displaying vibrational dynamics during SF. Reproduced with permission from American Chemical Society, Copyright 2017. [7]

Ultrafast mid-IR spectroscopy has also been employed to provide mechanistic information during the subsequent steps of the SF process. Grieco et al. used ultrafast mid-IR transient absorption and nanosecond-to-microsecond time-resolved IR spectroscopy to identify the spectral signatures of ^{1}(TT) and ^{1}(T...T) in TIPS-pentacene thin films as depicted in Figure 3.3. [7,116] They probed the asymmetric alkyne (C≡C) stretch of the side groups to follow the dynamics of the correlated triplet pair separation during SF. The mid-IR transient absorption spectra consisted of a narrow alkyne stretch at 2132 cm^{-1} superimposed on a broad electronic photoinduced absorption (PIA) feature, which corresponded to the excited-state absorption from the S_1 and ^{1}(TT) as shown in Figure 3.3c. By analyzing the dynamics of the PIA spectra in Figure 3.3d,e, they assigned the alkyne shift from 2132 to 2116 cm^{-1} to the ^{1}(T...T) state and found that TIPS-pentacene molecules transitioned within 3.4 ps from the ^{1}(TT) to the ^{1}(T...T) state. The authors also suggested that the complete dissociation of the ^{1}(T...T) state into the T_1 states occurs on a nanosecond time scale. This study demonstrates the strength of directly probing vibrational modes, where it led to the identification and characterization of the ^{1}(T...T) state, an otherwise difficult-to-isolate state, using electronic spectroscopies. Additionally, they observed an absorption feature at 2124 cm^{-1} corresponding to the hot ground state (S_0*), which reached half its final population within 50 ps. This fast time scale of populating the S_0* states was attributed to the excess energy distribution after vibrational cooling from the initially photoexcited S_0 states. This study thus highlights the utility of probing vibrational motions to provide insights about the energy dissipation pathways within the electronic states along the SF process. Monitoring the energy flow movement during SF will open the opportunity to understand its influence on the rate and yield of generation of the separated triplets for their harvesting in optoelectronic devices.

In addition to thin films, Grieco et al. also used mid-IR transient absorption to examine SF in solution by probing the local molecular environments in TIPS-pentacene. [117] They monitored the temporal evolution of the C≡C stretch of the side group and the

CH stretch motions of the alkyl chains in the side group in a TIPS-pentacene solution. This study showed that the TIPS-pentacene molecules form aggregates through their side groups that break the molecular symmetry, enabling rapid and efficient SF rather than diffusive interactions of the excitons in solution as previously thought. This study highlights the structural insights gained from vibrational motions to better comprehend the intermolecular interactions and symmetries that mediate SF.

TRIR spectroscopy has thus emerged as a new technique capable of examining the excited-state dynamics, structure, and nature of electronic states in SF chromophores through vibrational spectra. It has helped to identify the vibrational signatures of the intermediates ^{1}(TT) and ^{1}(T...T) and the triplet excitons in acene systems. It has provided insights toward elucidating the charge-transfer-mediated SF process, nuclear motions driving the formation of triplets, competition between relaxation pathways and triplet harvesting from ^{1}(TT), and the effect of intermolecular coupling and molecular symmetry on SF in acenes. Given that all chromophores undergoing SF possess native vibrational modes, TRIR spectroscopy offers an approach to examine electronic states involved throughout all the steps of SF in a variety of molecular systems. As many functional groups directly absorb in the IR region, TRIR will be sensitive to the vibrational evolution in many classes of SF molecules, making it a versatile technique to explore the structural origins of electronic states for the development of future SF-based optoelectronic devices. Furthermore, understanding how SF intermediates interact with the IR region of the solar spectrum can provide insights on how to maximize the utility of these photons in SF-based photovoltaic applications.

3.3.2 Raman-Based Techniques

Steady-state and time-resolved Raman spectroscopies can probe conformational changes by monitoring the inherently narrow vibrational Raman bands and their sensitivity to changes in molecular structure during SF. Steady-state Raman spectroscopy is useful in unambiguously assigning the structure of long-lived triplet states. Picosecond and

femtosecond Raman spectroscopies have been used to characterize triplet states and illustrate SF in acenes and biological systems, study the role of vibronic coherences in driving the photophysics, identify specific nuclear motions along the SF reaction coordinate, and provide design guidelines to modify the molecular structure for efficient SF in acene-based chromophores.

Steady-state resonance Raman spectroscopy has been applied to determine the structure of the long-lived triplet states generated by the SF process, useful in quantifying reorganization energies and identifying molecular structural changes between S_0 and T_1 states. For example, Angelella et al. probed the resonance Raman spectra of both the ground and triplet state of perylene bis(dicarboximide) (PDI) dimer. [118] They assigned the 1324 (CH in-plane bends), 1507 (perylene core I), and 1535 and 1597 (perylene core II) cm^{-1} bands to T1 signatures and noticed that they were redshifted with respect to the corresponding bands in the S_1 states. Chen et al. also measured the resonance Raman spectra of triplet states of tetramer and hexamer oligothiophenes, showing that the T1 excitation is delocalized at least over five rings. [119] Llansola-Portoles et al. used transient absorption and resonance Raman measurements to prove that lycopene crystalloids extracted from tomatoes undergo SF, the first time SF has been observed in a biological structure. [120] In the steady state they observed a power-dependent Raman band at 1128 cm^{-1} , corresponding to CC stretches, which have been previously shown to be fingerprints of carotenoid triplet excited states. These examples show that ground-state resonance Raman studies provide an easy alternative to extract spectroscopic information on triplet states without the need for triplet sensitization or pulsed lasers.

Adding a time component to resonance Raman, picosecond time-resolved resonance Raman (TRRR) spectroscopy, a pumpprobe technique that detects transient spontaneous Raman signatures, is an effective tool to quantify the triplet yields during SF. Wang et al. implemented TRRR to prove that zeaxanthin aggregates undergo SF with

$\sim$90-200% quantum yield [121, 122] and observed distinct vibrational features corresponding to the ground S_0, S_1, and T_1 states, with a triplet rise time of $\sim$4 ps. Although TRRR can identify different electronic states associated in SF through vibrational modes, its temporal resolution is limited to 12 ps, much longer than the ultrafast (<100 fs) time scale of the relevant nuclear motions to map out the excited-state reaction coordinate during SF. Nonetheless, the resonance condition enhances the Raman signal greatly, providing the ability to track structural evolution in SF systems with weaker Raman cross sections that may otherwise not be observable with other time-resolved Raman techniques. Additionally, resonance Raman intensity analysis could provide information on dimensionless displacements and initial excited-state dynamics out of the FranckCondon region, providing guidance on how to minimize energy losses caused by a structural rearrangement. Thus, resonance Raman spectroscopy is a promising technique that can be utilized in the future to provide insights into the early time dynamics of SF.

To understand SF enough to map out its potential energy surface, researchers require the knowledge of the evolution of the electronic states and the relevant nuclear coordinates as a function of time. Understanding the role of vibrational motions and vibronic couplings in the SF process has gained momentum recently, with many groups attempting to determine the contribution of vibronic coherence to the SF pathway. Stern et al. utilized TA and resonance Raman spectroscopy to reveal that certain vibrational modes in TIPS-tetracene drive the nuclear wavepacket originally generated in the S_1 state to the ^{1}(TT) potential energy surface, suggesting that ^{1}(TT) forms via a vibronic coherent process on an ultrafast time scale (<300 fs). [123] 2DES is an electronic technique sensitive to probing contributions of Raman active modes, and it is able to extract such information through vibronic coupling. Bakulin et al. used 2DES to identify the Raman bands in pentacene and its derivatives, suggesting that the mixing of the vibronic manifolds of the S_1 and ^{1}(TT) states plays a key role for pentacene and two of its derivatives to undergo SF on a sub-100 fs time scale with unit efficiency. [124]

The critical role of the vibronic coupling of states for a fast and efficient SF reveals the importance of nuclear degrees of freedom for optoelectronic devices based on SF. The coupling between electronic and vibrational states guides the photochemical reaction pathways in molecules. Identifying the coupled nuclear motions and its effect on the coupling between the states can allow us to synthetically modify existing molecules and design new molecules to tune the outcome of the ultrafast SF process.

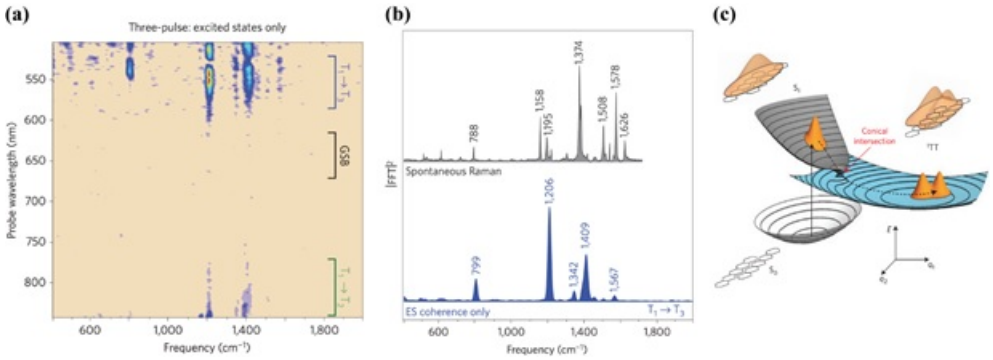

Figure 3.4: (a) Pump-dump-pulse experiment to observe vibronic coherence in the region of the excited-state absorption in the triplet manifold. (b) Integration of the frequency map in the dark blue bracket region in (a) generates the vibrational modes of the triplet exciton. Spontaneous Raman spectrum in gray is to compare the vibrational frequencies in the ground S0 and the triplet states (dark blue). (c) Schematic representation of the progress in SF mediated via a conical intersection. Reprinted by permission from ref [8]. Copyright 2015 Springer Nature.

To identify the importance and nature of vibronic coherence during SF, Musser et al. employed a pump-dump-probe technique to selectively depopulate the excited triplet states to measure the importance of vibronic coupling during SF in thin films of TIPS-pentacene. [8] Using the three-pulse experiment, they isolated the vibrational coherence in the final excited triplet states while removing the ground-state coherence, Figure 3.4a. Integration of the frequency map from the threepulse experiment in the excited-state absorption bands in the triplet manifolds and comparing it with the spontaneous Raman spectrum revealed the distinct vibrational modes of the triplet exciton in Figure 3.4b. This transfer of the initially generated wavepacket in the singlet excited state into

the separated triplet states is mediated through the correlated triplet pair indicating the presence of vibronic coupling between the S_1 and the ^{1}(TT) states. They thus proposed that the presence of such a strong vibronic coupling is evidence that SF in TIPS-pentacene undergoes the direct mechanism mediated by a conical intersection between the singlet and triplet manifolds, as shown in Figure 3.4c. Although this technique is unable to identify the specific nuclear motions driving the system toward the crossing, the presence of a conical intersection explains the high rate and efficiency of SF in TIPS-pentacene and helps to map a part of the complex potential energy surface. This model of the presence of a conical intersection mediating the SF process can thus be generalized to other ultrafast SF chromophores. The presence of mixed states based on a strong coupling between the nuclear and electronic degrees of freedom indicates that strong electronic couplings exceeding the energy difference between the S_1 and ^{1}(TT) are not required for an ultrafast SF process. Thus, the understanding of coherences can be used to effectively design new SF chromophores by modulating the strength of the vibronic coupling between the S_1 and ^{1}(TT) states. While other techniques such as TA also have the potential to identify vibronic coupling, this pump-dump-probe method is uniquely suited to investigate the role of vibronic coupling, because the "dump" pulse can be tuned to the absorption of the excited species of interest (in this case the $T_1 \rightarrow T_2$ transition), allowing the vibronic coherence of triplets to be isolated from the much stronger ground-state signals. Nonetheless, this method is only feasible if the dump pulse can be tuned to exclusively depopulate one excited species, which may not be possible in all SF systems.

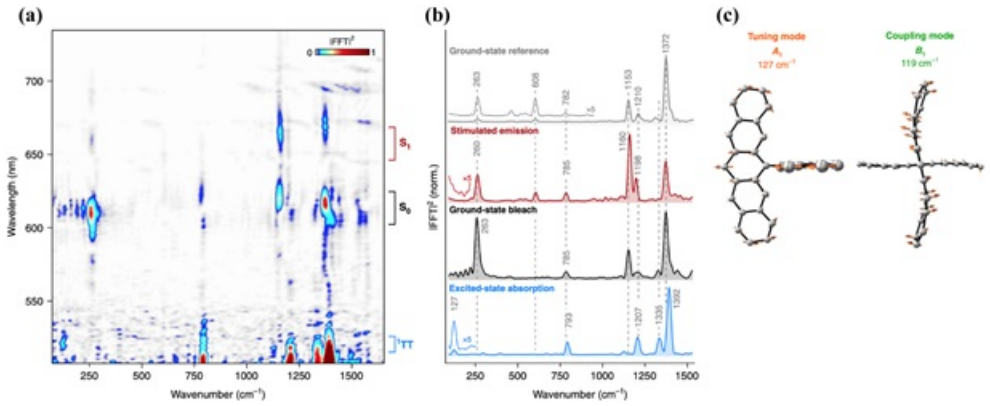

Figure 3.5: (a) Wavelength-resolved impulsive Raman spectra of pentacene dimer after impulsively populating the S_1 state. The marked regions represent the spectral map of the S_1, S_0, and ^{1}(TT) states. (b) Integrated region of the bracketed regions in (a) generates the impulsive Raman spectra of different species: stimulated emission (S_1), GSB (S_0), and excited-state absorption (^{1}(TT)). The off-resonant impulsive Raman spectrum in the ground state is in gray for comparison of the vibrational modes in the excited states. (c) Representative normal modes for the tuning and coupling modes during SF. Reprinted by permission from ref [9]. Copyright 2019 Springer Nature

In crystals, the coupling of individual molecular vibrations with the lattice also plays a role in driving SF-relevant photophysical processes. Impulsive stimulated Raman spectroscopy (ISRS) can observe the low-frequency modes of these excited electronic states without interference from Rayleigh scattering. Schnedermann et al. combined excited-state time-domain Raman spectroscopy and quantum mechanical simulations to probe the nature of the vibrational coherence in the ^{1}(TT) state and to identify the vibrational modes driving the SF process to construct a molecular movie of the ultrafast SF in real-time in a pentacene dimer. [9] Integrating the wavelength-resolved impulsive Raman data in a different spectral region, they obtained the vibrational modes unique to the S_0, S_1, and ^{1}(TT) states, as shown in Figure 3.5a,b. Their results demonstrated the roles vibrational modes with A1 symmetry and B1 or B2 symmetry, as shown in Figure 3.5c, play during SF. Vibrational modes with A1 symmetry do not mediate the coupling between S_1 and ^{1}(TT) states but, instead, modulate the pentacene core structure and act as tuning modes associated with in-plane ring deformation motions

during the SF reaction. Meanwhile, modes with B1 or B2 symmetry correspond to the coupling modes, which are associated with the twist around the pentacene-pentacene bond. Their real-space movie showed that the first 75 fs was dominated by inplane ring deformation, which positions the energy levels for efficient S_1 to ^{1}(TT) transition. The next 125 fs was dominated by the twist around the pentacene-pentacene bond, which drives the conversion of the S_1 to ^{1}(TT). However, the coupling modes were computationally predicted to be less intense than the tuning modes by an order of 2; hence, they were obscured and rarely observed experimentally. With a vibrationally sensitive technique, this study not only highlights the function of vibrational modes during SF in real-time but also identifies the driving motions for efficient ^{1}(TT) generation in real-time, which was previously unknown. Identifying those unique nuclear motions can then be used for either mode-selective excitation to facilitate the efficient ^{1}(TT) generation. Furthermore, their use of impulsive Raman to experimentally measure the intrinsic ^{1}(TT) spectrum is invaluable in studying this intermediate directly, rather than through inference from comparing S_1 and T_1 spectra. Information gained from this study can be used as guidelines to synthetically modify chromophores that can display those vibrations without attenuation for their use as efficient SF chromophores.

Femtosecond stimulated Raman spectroscopy (FSRS) is an ultrafast structurally sensitive technique used to study real-time transient structural evolution during SF. FSRS can provide vibrational structural information on a time scale that is comparable to the time period of the probed nuclear motions. It can have both high temporal (sub-50 fs) and spectral (10 cm^{-1}) resolution, while still obeying the Heisenberg uncertainty principle. What sets FSRS apart from other IR-based techniques is that it can simultaneously probe vibrational features over a wide spectral window of 3000 cm^{-1}. This is important, as the SF chromophores display numerous vibrational motions over a wide frequency range, and FSRS can probe them all together as compared to other ultrafast IR spectroscopies, which are typically limited to a narrower spectral region. Even

though the scattering cross sections are the same as for spontaneous Raman, the scattering signal is enhanced by 6 orders of magnitude in FSRS leading to high signal-to-noise ratios and shorter acquisition times. Additionally, FSRS is a nearly fluorescence-free technique due to the signal being detected in the small solid angle. This unique property of FSRS makes it well-suited to study SF chromophores, where fluorescence background can overwhelm the vibrational signatures of interest. Each of these unique qualities of FSRS helps to obtain the relevant changes in vibrational energies across the broader regions of the same molecules during SF, providing a more holistic view of structural change during SF.

To obtain structural information used to determine the mechanism of SF, Hart et al. used FSRS to study the triplet formation mechanism in crystalline pentacene. [125] From the FSR spectra of pentacene crystals, they observed a broad transient absorption background, which corresponded to spectral signatures of triplet states formed beyond $\sim$800 fs. Before the formation of the triplet states, they observed two excited-state Raman peaks, one upshifted and one downshifted by $\sim$525 cm^{-1} for each of the ground S_0 peaks. On the basis of the kinetics of the Raman vibrational modes and theoretical calculations, they assigned the split Raman bands to intermediates with charge transfer character, suggesting that SF in crystalline pentacene proceeds via the two-step charge transfer-mediated mechanism. Therefore, this study provides insights into the evolution of the intermediate charge transfer states on the highly anharmonic potential energy surfaces and suggests that anionic and cationic species could play a role in facilitating efficient SF. This work lays out the structural evolution in molecules during the early ^{1}(TT) formation step during SF, which can help in modifying existing materials for effective optoelectronic devices.

The ^{1}(TT) state must separate into triplets for efficient harvesting of solar energy, and thus further investigation of the structural reorganization during the separation of the ^{1}(TT) is needed. To gain insights into the molecular nuclear dynamics during the SF triplet separation process, Bera et al. studied the structural evolution in crystalline

rubrene with FSRS (Figure 3.6a). [10] Prior measurements with TA, 2DES, and TR-PL on crystalline rubrene reported the time scale of SF to vary from 30 fs to 100 ps and the lifetimes of triplets to be on the order of 10 ns-100 μs. [42,105,126] The observation of such a wide range of time constants is attributed to the presence of anisotropy in crystalline rubrene and also due to the fact that different techniques detect different steps during the SF process in crystalline rubrene, as depicted in Figure 3.2. However, these ultrafast techniques are useful to provide the time constants of various steps during SF in crystalline rubrene, which has been used in extracting structural information using FSRS. As shown in the time-resolved FSR spectra in Figure 3.6a, they observed not only a vibrational feature around 1660 cm^{-1} corresponding to the ^{1}(TT) state but also two Raman modes around 1430 and 1542 cm^{-1} that displayed large transient frequency shifts to higher frequencies. Analyzing the dynamics of these Raman peak frequencies, they found that these frequency shifts occur on the same time scale as the separation of ^{1}(TT) to ^{1}(T...T). On the basis of spontaneous Raman measurements on a rubrene derivative and density functional theory calculations on rubrene charged species, they attributed the blue shift of the Raman modes during the separation of the correlated triplet pair ^{1}(T...T) to a structural reorganization that shifts the electron density away from the tetracene core of the crystalline rubrene molecules. Given that the ^{1} (TT) $\rightarrow$ ^{1}(T...T) is associated with loss of electron density, they proposed that molecules that facilitate similar changes in core electron density will undergo efficient SF.

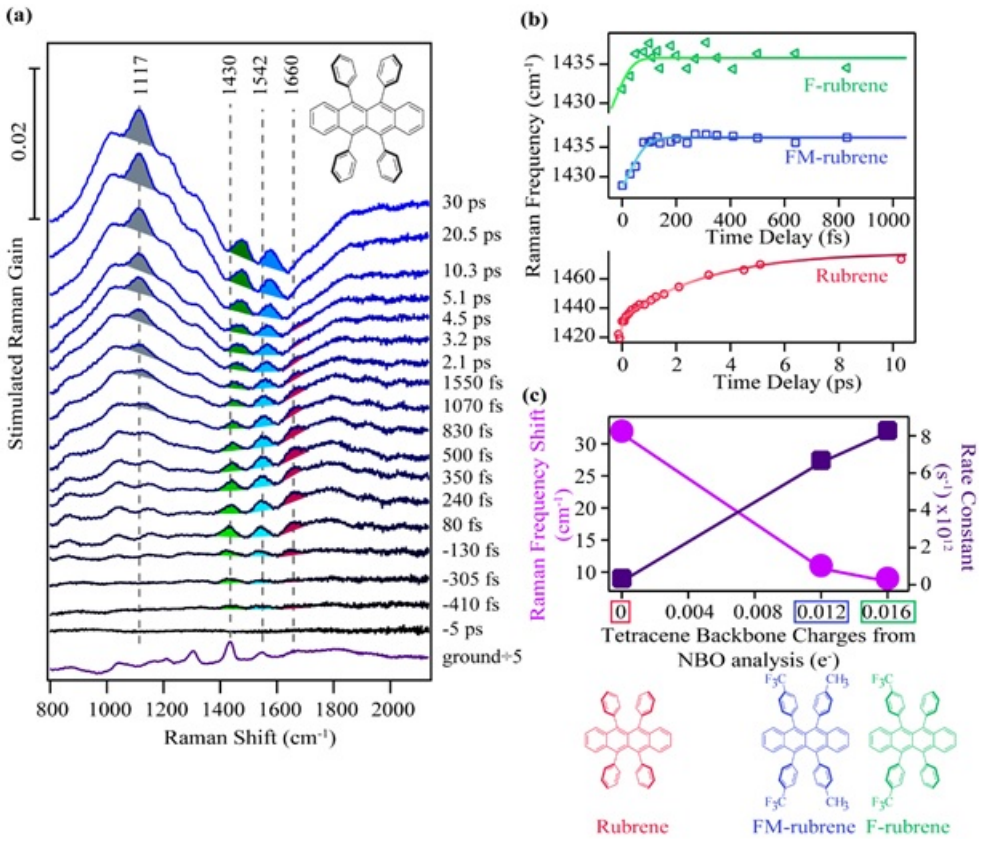

Figure 3.6: (a) Molecular structure and time-resolved FSR spectra in crystalline rubrene at different time delays after photoexcitation. (b) Transient time evolution of the 1430 cm^{-1} Raman mode displaying a blue shift during the ^{1}(TT) separation in rubrene, FM-rubrene, and F-rubrene. (c) Total shift of the 1430 cm^{-1} Raman mode and the associated rate constant for this peak shift as a function of total charge on the tetracene backbone calculated from natural bond orbital (NBO) population analysis in the rubrene derivatives series. Adapted with permission from American Chemical Society, Copyright 2017, refs [10] and [11].

Building on the structural evolution knowledge gained during crystalline rubrene SF, Bera et al. have successfully screened and designed fluorinated rubrene derivatives F-rubrene and FM-rubrene, with reduced core electron density, as shown in Figure 3.6c to study the prospects of spectroscopyguided rational designing of SF chromophores. [11] They observed similar blue-shifting of the transient Raman peak at 1430 cm^{-1} in the rubrene derivatives as they observed in unsubstituted rubrene, as summarized in Figure

3.6. However, the derivatives displayed lower frequency shifts on a much faster time scale compared to rubrene. Therefore, not only did they provide the first experimental evidence of SF in those rubrene derivatives but they also observed SF rates an order of magnitude higher in the derivatives than in nonsubstituted rubrene (Figure 3.6c). Using FSRS, they demonstrated that the fluorinated rubrene derivatives undergo less structural reorganization than rubrene, because the initially more electropositive tetracene core does not have to lose as much electron density to generate the ^{1}(T...T) state. [11] The knowledge of the structural evolution in regard to the electron distribution provides a new synthetic control over the ultrafast SF process. Therefore, this study bridges the gap between the spectroscopic results and its realization as practical application to devise principles for novel materials with better SF properties that go beyond the energy criteria. These studies by Bera et al. demonstrate the fulfillment of the long-harbored promise of spectroscopy-guided rational engineering design and syntheses formulations of future chromophores for efficient SF.

Thus, ultrafast Raman spectroscopy is ideally suited to investigate the influence of molecular structure on SF, with a unique combination of broadband probing, high temporal resolution, and compatibility with small sample volumes. It has been used to identify the vibrational signatures of the ^{1}(T...T) and charge transfer intermediate species, unique nuclear motions driving the photoexcited wavepackets to the triplet states, structural reorganization during the triplet formation, and insights into molecular designing principles. These advances provide means to implement the structural evolution knowledge into synthesizing new SF sensitizers.

3.4 Recent Developments and Future Directions

Vibrational spectroscopy is a well-equipped field to discern an underlying mechanism, vibronic couplings, and molecular structural changes across different steps in the SF process. TRIR and resonance Raman can identify intermediate chemical species by their

distinct vibrational signatures, multidimensional vibrational spectroscopy can identify vibronic coupling and the specific nuclear motions driving the SF process, and FSRS can provide insights into the conformational changes occurring in the molecular structure during SF. While we have discussed the unique capabilities of vibrational spectroscopy that advanced the SF field, vibrational techniques have yet to reach their full potential in helping us identify the design principles for making better chromophores for SF-based devices. In addition to the recent advancements in the SF community, vibrational spectroscopies can have multiple interesting avenues to explore, as we discuss in this section.

3.4.1 Magneto-Vibrational Spectroscopy

The coupling of two triplet states can result in triplet ^{3}(TT) and quintet ^{5}(TT) states in addition to the singlet ^{1}(TT) state. [127] Although quintet ^{5}(TT) states have been observed as SF intermediates in TREPR studies, [107, 108, 128] we do not understand their roles in SF well, because their electronic and vibrational spectral features are highly similar to that of the ^{1}(TT) state. Incorporating a strong magnetic field with a vibrational technique can make it possible to differentiate the vibrational features of ^{1}(TT), ^{3}(TT), and ^{5}(TT) intermediates and may help us understand whether strong ^{1}(TT), ^{3}(TT), and ^{5}(TT) coupling is desirable for an SF process. We can also learn if certain vibrational motions drive molecules toward any of the ^{1}(TT), ^{3}(TT), and ^{5}(TT) states and use that insight to optimize certain excitation pathways. While not yet utilized in an SF study, magnetoinfrared spectroscopy, where IR spectra were collected under magnetic fields of various strengths, was used to investigate magnetic transitions in single crystals of the anti-ferromagnet $[Cu(HF_2)(pyz)_2]BF_4$. [129] Musfeldt et al. observed red shifting of out-of-plane pyrazine ring deformation and out-of-plane CH bending modes at higher magnetic fields, revealing that the pyrazine ring was distorted to accommodate the fully polarized magnetic state. [129] If a similar magneto-vibrational technique were to be applied on SF systems, we would have a better understanding of

the dynamics involved with ^{3}(TT) and ^{5}(TT) during SF and if the three-step process in eq 3.2 is actually an accurate description of SF in all molecular systems. On the basis of this spectroscopic technique, molecular systems where the appropriate relative molecular orientations and vibrational motions can access the ^{3}(TT) and ^{5}(TT) can be designed for understanding SF from a mechanistic viewpoint.

3.4.2 Mode-Selective Excitation

Another exciting future possibility is the application of mode-selective excitation to drive or inhibit SF in organic chromophores in order to confirm the role of specific nuclear contributions in the SF process. Mode-selective excitation and inhibition of Raman or IR modes can be achieved by shaping femtosecond pulses to excite desired vibrational modes while suppressing others.56 For example, Grumstrup et al. made use of adaptive pulse shaping to increase triplet yield in tetracene films, leading to a 20% increase in the triplet absorption feature. [130] A computational study by Castellanos et al. also revealed that destructive interference between two coexisting charge-transfer-mediated fission pathways in a model pentacene dimer can be suppressed by intermolecular vibrations, leading to a more efficient SF process. [131] Recently, Paulus et al. identified excitedstate vibronic coherences in iron(II)-based chromophores and then synthetically modified the molecules to interfere with the vibrational modes associated with the coherences, which led to more than a 20-fold increase in the lifetime of the photoinduced excitons. [132] Similar studies could be done with SF chromophores, where it is possible to synthetically modify a molecular structure to affect the vibrational motions of interest that facilitate SF while simultaneously inhibiting other relaxation pathways, increasing exciton lifetimes and diffusion lengths, therefore improving the efficacy of SF-based photovoltaics.

3.4.3 Terahertz Spectroscopy

Analogous to vibronic coupling, phonon modes can couple to electronic states in thin films or crystalline chromophores undergoing SF. Terahertz (THz) spectroscopy is a vibrational technique that spans the electromagnetic spectrum between the microwave and the far-IR regions, matching the energies of crystalline phonon vibrations and intermolecular bonding. [133] Although not yet utilized in an SF study, it has been increasingly used to investigate carrier dynamics in photovoltaic materials. [134] In a recent example, Lan et al. used time-resolved multi-THz spectroscopy to probe coherent and incoherent charge carrier dynamics in a low-temperature orthorhombic phase of methylammonium lead iodide perovskite. [135] With the aid of computational calculations, they assigned excited-state THz spectral features to two distinct populations of free and bound excitons that appeared at different time scales. They also observed charge coupling to the low-energy phonon mode at 30 cm^{-1} , which likely arose from a mixed inorganic and organic sublattice motion. Employing THz spectroscopy to SF systems would help to decipher the roles that phonons or intermolecular interactions play during each step of the SF process. This will enhance our understanding further into the role and importance of lattice orientation and molecular packing contributions to efficient SF.

3.4.4 Exciton Transport

As our understanding of the SF mechanism improves, more studies emerge that are dedicated to optoelectronic device optimization. We believe that the next step forward, in addition to synthesizing newer classes of SF chromophores, is to minimize energy losses from transport by understanding how the charge carriers propagate. Previous studies have mainly employed electronic spectroscopic techniques such as TR-PL and TA to study the charge carrier transport and recombination dynamics during SF. For example, Akselrod et al. have imaged exciton transport in a tetracene crystal and thin film

by detecting the delayed fluorescence from triplettriplet fusion. [60] This study showed the importance of nanoscale morphology on exciton transport: the transit mode in crystals was random walk diffusion but was subdiffusion in thin films due to the presence of exciton traps. Meanwhile, Huang et al. utilized transient absorption microscopy (TAM) to simultaneously image singlet and triplet exciton transport and discovered the cooperative nature of their transport. [136] As singlet and triplet excitons have different TA bands, Huang et al. generated separate exciton maps to extract the diffusion lengths of singlet and triplet excitons in SF chromophores, respectively. Although these time-resolved spectroscopic techniques have provided valuable information about the exciton charge transport dynamics, they do not provide the influence of molecular structural properties on the transport process, making it harder to target specific functional groups to improve the transport properties of existing materials.

To extract molecular structural information during transport, Kwang et al. have recently developed spatially offset femtosecond stimulated Raman spectroscopy (SO-FSRS), which combines the strength of vibrational studies and exciton transport imaging. [12] As seen in Figure 3.7a, the photoexcitation pulse is raster-scanned across the Raman pump and probe pulses, which are held stationary with time. Thus, excitons need to propagate from the initial photoexcitation zone to the probing zone before they can be observed. Although SO-FSRS is still a technique in its infancy, it verified that the fast exciton transport axis is identical to that of free charge carriers in TIPSpentacene and that exciton transport is less anisotropic than free charge carrier transport. By tracking the Raman bleaching features of TIPS-pentacene at each photoexcitation location, they generated excited-state structural maps at multiple time delays as shown in Figure 3.7b, providing a visual representation of exciton transport over time. This allows us to observe how molecular structure evolves spatially as excitons travel through the material. As the vibrational analogue of TAM, SO-FSRS can help to identify specific molecular interactions that facilitate or hinder charge and exciton transport in SF systems for future studies. By offering valuable insight on how to design molecules that

both undergo efficient SF and have long-range energy transport efficiency, SO-FSRS helps to move closer to achieving commercialization of SF-based optoelectronic devices.

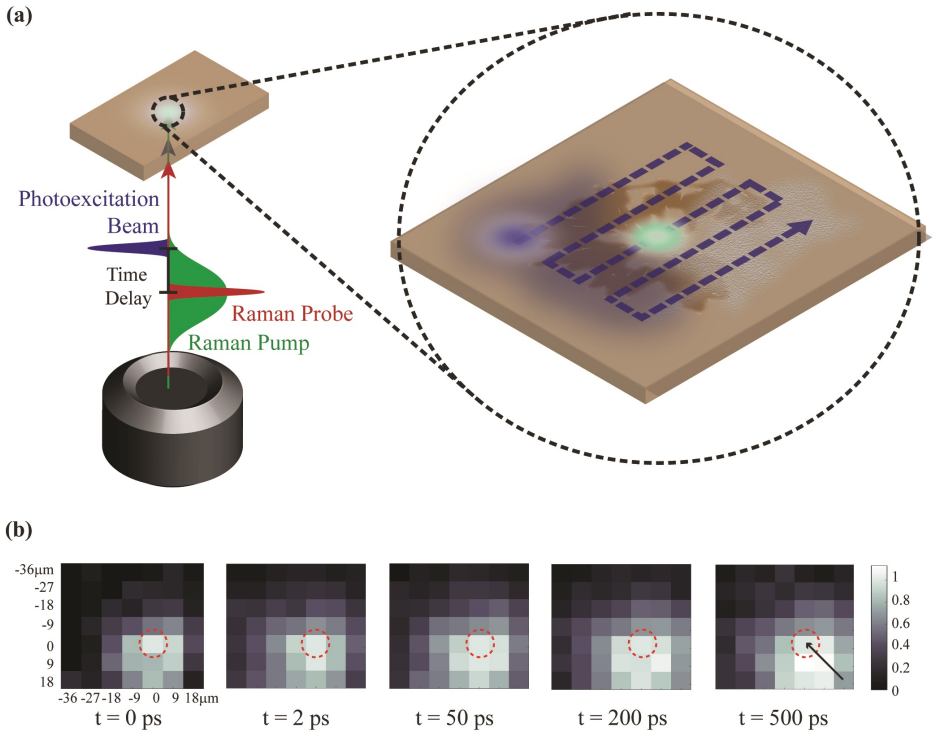

Figure 3.7: (a) Schematic representation of the pulse profiles and raster scan for SO-FSRS experimental setup. (b) Evolution of the 1386 cm^{-1} vibrational mode depletion in TIPS-pentacene at different photoexcitation positions over time. The dashed circle represents the position of the Raman probe pulse. The arrow in the rightmost panel represents the diffusion direction of the excitons generated in the bottom right photoexcitation position, which falls along the fast exciton transport axis in TIPS-pentacene. Adapted with permission from American Chemical Society, Copyright 2020. [12]

3.5 Conclusions

This Perspective demonstrates that vibrational spectroscopy has emerged as a technique capable of examining the influence of molecular structure and its evolution in chromophores to broaden the understanding of SF, as well as to give roadmaps on how to modify existing molecules to make them better suited for SF-based applications.

The importance of vibrational motions in SF research started with the realization that vibronic coupling mediates the SF process in many organic chromophores. Although vibrational studies typically require computational work to interpret the data, improvements in theoretical methods have made previously complex calculations feasible, giving a considerable amount of momentum for the employment of vibrational spectroscopy to understand the role of molecular structure of the materials on the electronic states and its influence on the SF efficiency. The sensitivity of vibrational features to local environments makes it possible to identify molecular interactions that facilitate or hinder progress in each step of the SF mechanism. Studies using time-resolved infrared spectroscopy have identified the specific nuclear motions driving the coherent SF process, thereby providing a tool to control photochemistry. Ultrafast Raman spectroscopy has successfully exhibited its strength in providing real-time structural reorganization knowledge of the excited electronic states and has guided the screening procedure and intelligent design principles for creating efficient SF chromophores. These techniques together help understand the SF pathway and provide roadmaps to design new molecules that are better suited for SF applications by modifying specific areas within existing molecules.

Chapter 4

Developing Spatially-Offset Femtosecond Stimulated Raman Spectroscopy

4.1 Utility of SO-FSRS

As established in the previous chapter, vibrationally sensitive techniques are crucial in helping us understand mechanisms of photo-processes and help drive progress in photovoltaic technology. One key challenge that photovoltaic or any molecular electronics faces is the lack of understanding on the mechanism of charge transport, where a lot of efficiency is lost. While FSRS is an incredibly useful technique to study charge transfer at a local scale, it lacks the spatial resolution to study charge transport. Since the Raman probe and pump pulses in FSRS need to be spatially and temporally overlapped to generate stimulated Raman spectra, it would make more sense to introduce the spatial component to the photoexcitation pulse. Fortunately, transient absorption microscopy provides an inspiration on how that can be achieved. By sending the photoexcitation

through a galvosystem before interacting with the system, one can raster scan the photoexcitation pulse and excite the system at controlled distances from the probing zone. Thus, only Raman spectra from charges that have propagated into the probing zone would be picked up, allowing us to look at charge transport through a vibrational lens.

4.2 Hardware

4.2.1 Rationale for Picking Thorlabs GVS012 Galvosystem

The first step to developing SO-FSRS is to purchase the right hardware. While there were many options, we narrowed it down to ThorLabs GVS012 and Cambridge Technology 6231H. I compared the specifications of these two galvoscanners in Table 4.1.

Table 4.1: Specifications comparison between GVS012 and 6231H. *70 μrad if using standard switch mode PSU(Power Supply Unit)

Galvomirrors	ThorLabs GVS012	Cambridge Technology 6231H
Repeatability (μrad)	15	8
Resolution (μrad)	15*	8
Max Beam Diameter (mm)	10	8 - 15
Wavelength Range	500 nm - 2.0 mm	350 nm - 12 mm
Scale Drift (PPM / °C)	40	50
Zero Drift (μrad/ °C)	10	15
Peak Current	10	20
Position Output Scale Factor (V/°)	1, 0.8, 0.5	0.5
Cost ($)	2935	5200

The specifications of Cambridge Technology 6231H are better than ThorLabs GVS012 in almost all cateogories. Furthermore, its repeatability and resolution of Cambridge Technology 6231H is about twice as good as that of ThorLabs GVS012. As a result, it costs significantly more than the ThorLabs GVS012 paired with GPS011, its compatible

power supply unit (PSU) (cost $<$ \$1000).

To figure out if Cambridge Technology 6231H is worth the extra cost, I did some simple calculations on the angle resolution we require using this simple diagram:

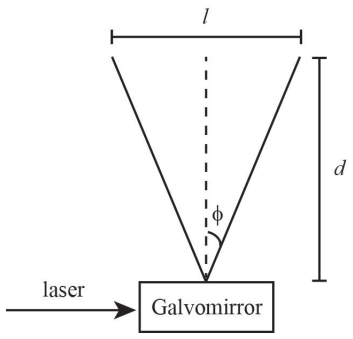

Using $l = 2d\tan(2\phi)$, where l is the spatial range of the sample and d is the distance between the galvoscanner (or galvomirror) and the sample, we estimate that the scan angle range is $\sim 83\,\mu$rad for $l = 50\,\mu$m and $d = 30\,$cm. As this calculation assumes the absence of a microscope objective, SO-FSRS experiment conducted with 40x or 60x microscope objectives will use a much larger angle scan. Thus, a resolution improvement of 15 μrad to 8 μrad may not be necessary.

Other than cost, the major advantage ThorLabs GVS012 has over Cambridge Technology 6231H is its comprehensive manual. Furthermore, Professor Libai Huang's group also uses GVS012 for their transient absorption microscopy setup, the TA analog of SO-FSRS, providing us with a consult reference should we need one.

I did a quick calculation to verify that our laser pulses are operating under the damage thresholds of the mirrors in GVS012. According to its manual, the damage threshold for the silver mirrors of GVS012 is $3\,\mathrm{J/cm^2}$ at 1064 nm, 10 ns pulse, which translates to $3 \times 10^8\,\mathrm{W/cm^2}$. Assuming an average power of $20\,\mu$W and a diameter of $10\,\mu$m, our photoexcitation pulse is hitting the silver mirrors at $20\,\mathrm{W/cm^2}$, way below the damage threshold.

Thus, we decided on purchasing ThorLabs GVS012 and its accompanying power supply unit GPS011 that improves the resolution from 70 μrad to 15 μrad.

4.2.2 Data Acquisition Cards

A data acquisition (DAQ) device is a device that converts digital information (from the computer) to analog electronic output (e.g. voltage, current) and converts analog

electronic input to digital information that the computer can process. As GVS012 responds to voltage commands to adjust the mirror angles, I needed a DAQ device that has 2 analog output, one for each axis (X and Y).

To achieve a 15 μrad resolution of GVS012 at 0.5 V/°scale factor, I needed a DAQ device that can reliably produce 430 μV of output. Looking at the manuals available, I calculated the absolute accuracy in the range of 89 μV to 520 μV for seven DAQ devices from National Instruments DAQ catalog, with the cost increasing at a disproportionate rate with improved accuracy.

Before committing to purchasing a new DAQ device, we obtained PCI-MIO-E-6 DAQ card, which is a legacy unit that is no longer sold on National Instruments, from the Chemistry Department electronic shop to test out our technique. As a peripheral component interconnect (PCI) card, PCI-MIO-E-6 is inserted into the only PCI slot of the lab computer, and then connected to SCB-68, a shielded connector block that serves as an interface between the PCI card and any electronic connections. SCB-68 has 68 screw terminals arranged in the manner shown in Figure 4.1. To connect to the DAQ pins, one needs to screw down open wire ends to the corresponding screw terminals tightly to ensure good electrical contact.

As the voltage output resolution of this DAQ device is only $\sim$2 mV, using PCI-MIO-E-6 alone would be insufficient to achieve good spatial resolution for SO-FSRS experiments. I overcame this limitation using a voltage divider, which is covered in more details in Section 4.2.4.

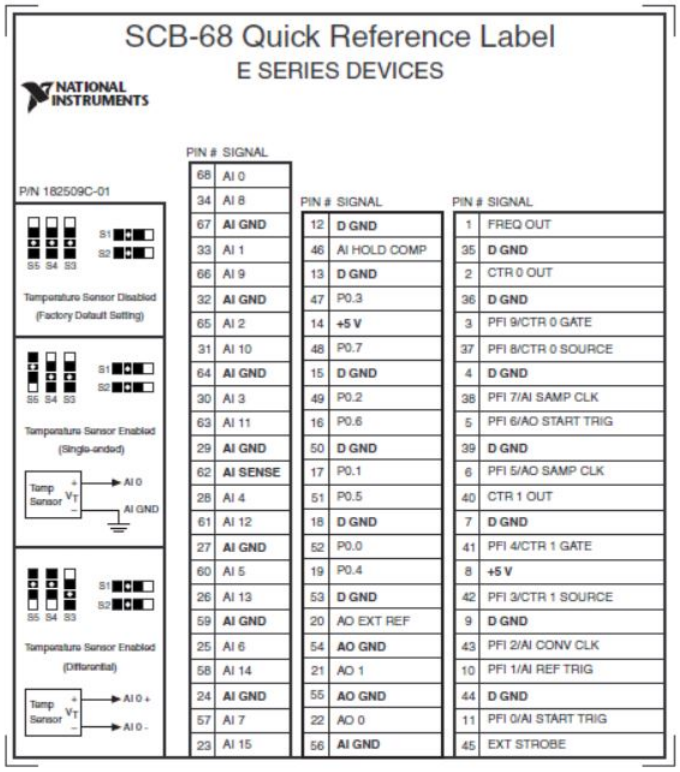

Figure 4.1: SCB-68 quick reference label on which screw terminal corresponds to which signal input/output.

4.2.3 ThorLabs GVS012

GVS012 came with the following components:

- 2D galvomirror
- 2 servo drivers, one for each mirror (X and Y)
- covers for the servo drivers (ordered separately)
- 2 mating connector bodies for J7, with pin 1 and 2 (command inputs) crimped
- 2 mating connector bodies for J6
- numerous crimps (22-26 AWG (American wire gauge, a measure of wire thickness))

- 2 power cables to connect each servo driver to an external power supply unit (not in use because we are using GPS011 instead)

The GPS011 power supply unit came with the following components:

- GPS011 unit (select 115V, can be changed easily on the unit)
- 2 power cables to be connected to each servo driver
- power cable that connects the GPS011 to the power supply

Figure 4.2 shows the electrical components of a single servo driver. JP4 is for external enabling and is not relevant to our SO-FSRS experiments. To connect GPS011 power supply unit to our servo driver, I inserted one of the provided power cables into the J10 connector. The connector "latches" on comfortably when the cable is inserted correctly. If the connection is incorrectly inserted by 180°, the servo driver will not be powered up. Next, I connected a cable attached to the 2D mirror (labeled either as X or Y) and established a connection with the servo driver through connector J9. More details on what individual pins in JP4, J9 and J10 are for can be found in the GVS012 manual. [137]

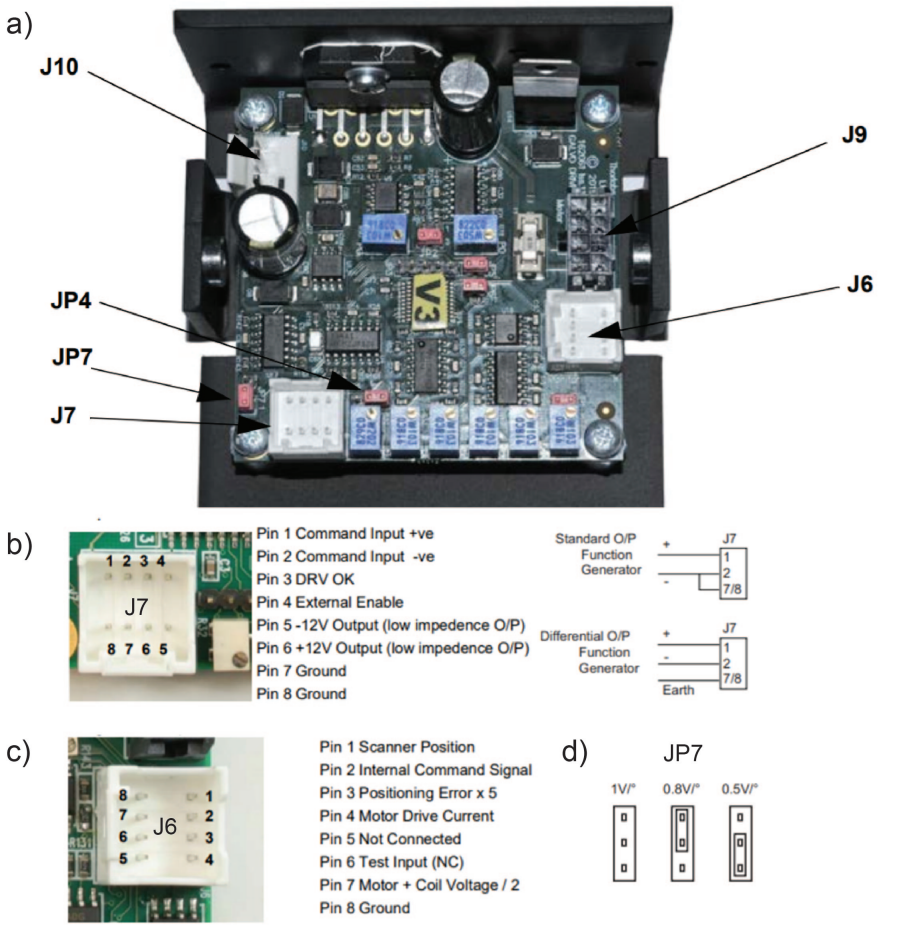

Figure 4.2: (a) GVS012 servo driver connector identification. JP4 - only used if external enabling is required. J6 - diagnostics connector. J7 - command input connector. JP7 - pins to set volts/° scaling factor. (b) J7 command input connector pin identification. J9 - connector that links to one mirror on the 2D galvomirror. J10 - power supply connector for the servo driver, connected to GPS011.(c) J6 diagnostics connector pin identification. (d) Different volts/° scaling factors are set based on how the pins at JP7 are connected.

As mating connector bodies for J6 and J7 are not fully equipped with crimped wires, my next step was to crimp the wires and insert them into the mating connector bodies. Figure 4.3 shows a schematic that provides examples of an optimal crimp, as well as common errors found in sub-optimal crimps. Sub-optimal crimps are either insecure

(i.e. the wire can be easily detached from the crimp) or provide poor electrical contact with the wire. With the help of an appropriately sized crimping tool borrowed from the E-shop, I managed to crimp enough wires and plugged them into the respective mating connector bodies as demonstrated in the simple schematic on the right.

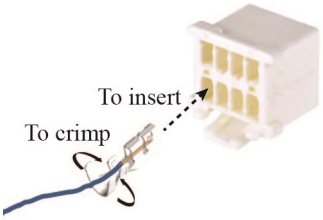

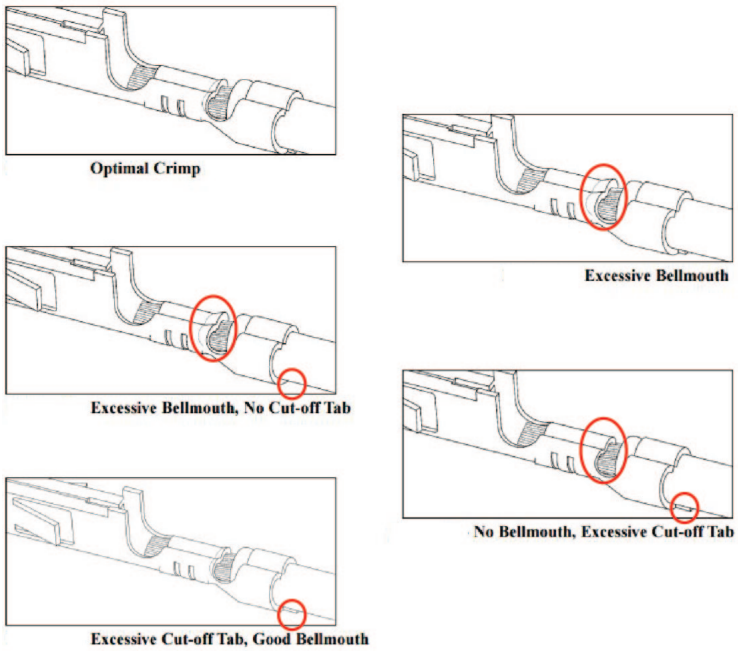

Figure 4.3: Examples of an optimal crimp, as well as common errors found in sub-optimal crimps.

From Figure 4.2b, the most important pins for running SO-FSRS are pins 1, 2, and 7/8, which correspond to the positive voltage command input, negative command input and ground connections respectively. Since the DAQ device that I am using is a differential output function generator, pins 7 and 8 are connected to the ground state, while pins 1 and 2 are connected to the voltage positive and negative input terminals respectively. Pin 3 (DRV_OK) is an open collector output that is low when the board is operating normally and floating (high voltage value) if a fault occurs. To use it as

a fault indicator, I connected it to a pull-up resistor that's connected to a +5V from the DAQ card and an analog voltage input. Currently, this analog input has yet to be programmed to be continually monitored and checked for fault (high voltage value). I did not connect pins 4-6 to anything because they are irrelevant to our experiment. Next, we can see from Figure 4.2c that all pins in J6, other than the pin 8 ground, provide voltage signals, which can be directed to an oscilloscope for analysis or connected to an analog voltage input reader. While not required for running SO-FSRS experiment, J6 provides an avenue for us to perform diagnostics and troubleshooting if GVS012 is not operating as intended. Chapter 5 - Troubleshooting of the GVS012 manual provides instructions on how to use diagnostic information from J6 to figure out how to diagnose and fix the problem encountered from running GVS012. [137] As the output from J6 pins are analog voltages, I connected each of the J6 pins to different analog voltage input to the PCI-MIO-E-6 DAQ card via the SCB-68 block. Last but not least, JP7 is a series of 3 pins that can control the voltage/° scaling factor based on how they are connected as shown in Figure 4.2c. The default setting is 0.5V/°, which means that the angle of the X or Y mirror is rotated by 1° for every 0.5V increase in its voltage input. I kept the scaling factor at 0.5V/° because this setting allows us to have the smallest angular step size possible.

4.2.4 Electrical Connections

To improve the voltage resolution achievable in our experiment with PCI-MIO-E-6, I came out with the idea of using a voltage divider. A voltage divider depends on two very simple principles:

- when resistors are connected in series, the voltage across them are split proportionally based on their resistance values.
- when a component is connected in parallel to another component, they will experience the same voltage.

Before I constructed a permanent fixture for the voltage divider, I made use of a test circuit breadboard. First, I placed a 1kΩ and 100kΩ resistor in series on the breadboard. I used a free form wire to connect the analog voltage output (AO 0) from the DAQ device (via the SCB terminal block) across both resistors. Then I attached the pins 1 and 2 from J7 (pins to accept voltage command) of the x-axis servo driver across the 1kΩ resistor. I then repeated the above with a separate pair of 1kΩ and 100kΩ resistors with AO 1 and the y-axis servo driver.

In order to test that the voltage divider is working as intended, I made use of the PCI-MIO-E-6 test panel available in National Instruments Measurement & Automation Explorer (NI MAX) to control the voltage output by the PCI DAQ card. To access the test panel, I first selected PCI-MIO-E-6 under "Devices and Interfaces" on the left panel of the NI MAX program. The center panel would now display "Settings", "External Calibration" and "Self-Calibration" information about the PCI DAQ card. The test panel can be found on the right of a row of icons above "Settings".

Once the test panels are open, there would be four tabs: 'Analog Input', 'Analog Output', 'Digital I/O' and 'Counter I/O'. I went to the 'Analog Output' tab and selected AO 0 as the channel that I wanted to test. After updating the output value using the 'Voltage DC' mode, I used a multimeter to measure the voltage output by the DAQ card and the voltage registered across pins 1 and 2 of the J7 connector of the x-axis servo driver. I repeated this for multiple voltage values and repeated the test for AO 1 and the y-axis servo driver. The results of this test is plotted in a Voltage Command (V) vs Voltage Output (V) graph as shown in Figure 4.4.

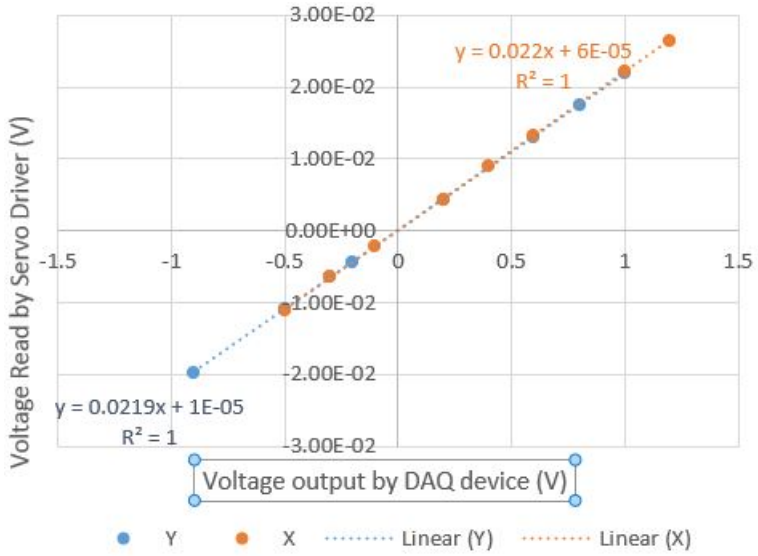

Figure 4.4: Graph demonstrating how the voltage divider reduces the voltage read by the servo drivers for the X- and Y- axis mirrors.

Thus, it is demonstrated that the voltage divider that I constructed reduced the voltage command sent to the x-axis and y-axis servo drivers by 45.45× and 45.66× respectively. I built a more permanent voltage divider setup by soldering the connections using a non-contact breadboard.

Eventually, the first complete circuit connection is shown in Figure 4.5. After all the connections were in place, I screwed the servo drivers' covers on to minimize dust accumulation on to the servo drivers' electronics. As the openings provided by the servo covers were small, there was a lot of tension imposed on the cables and wires. Thus I decided to remove the front panel of the servo drivers' covers such that it provides protection of dust from the top, while leaving enough rooms for the wires and cables to 'breathe'. While the connections from J6 has remained unchanged since the first version, there had been a few changes to the voltage divider set up as I fine-tuned it to better suit our experimental goals.

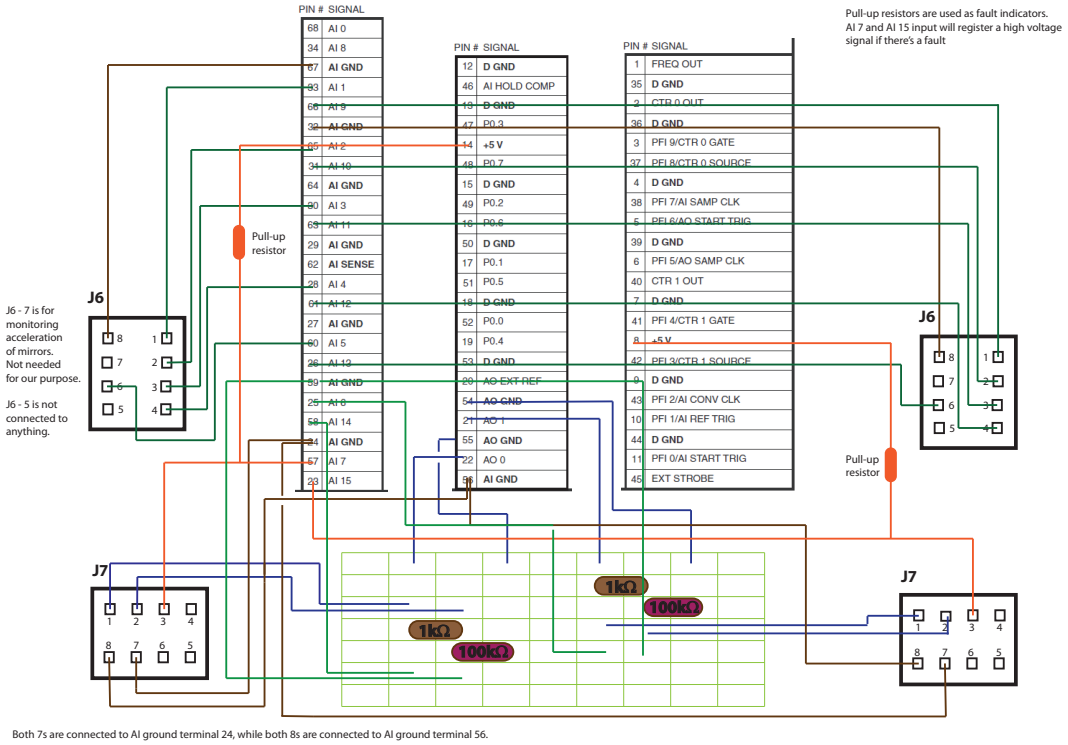

Figure 4.5: Schematic showing how the servo driver connectors are connected to the PCI-MIO-E-6 DAQ card via the SCB-68 screw terminal block.

The first tune-up I introduced to the voltage divider was to connect J7 pins 1 and 2 across the 100 kΩ resistors instead of the 1 kΩ resistors. This allows us to use the 2D galvomirrors for aligning the photoexcitation beam, making the system more user-friendly. More details on the rationale are found in a later Section 4.4.

After the publication of the first SO-FSRS paper (see Chapter 5), I decided to tune-up the voltage divider again to improve the spatial resolution of SO-FSRS. Using a circuit simulator at `https://falstad.com/circuit/`, I simulated different modifications to introduce coarse and fine adjustments of voltage sent to our servo drivers, allowing us to use the coarse setting for alignment and fine setting for raster scanning.

When I finalized the design of the voltage divider, I purchased the following items:

- USB 6001 DAQ device $\times 1$
- 10 ft USB 2.0A to USB Mirco B cable $\times 1$
- 1 kΩ resistors $\times 2$
- 10 kΩ resistors $\times 2$
- 1 MΩ resistors $\times 6$
- 1597-12640BD Breadboard $\times 1$

The USB 6001 is very portable and is powered by the main computer through a USB cable. Its terminals are screw terminals so wires can be directly screwed on to establish contact. I decided to use the USB 6001 DAQ device for the fine adjustment because PCI-MIO-E-6 is an old device that has not been calibrated in years and is more likely to be less accurate. The breadboard I purchased has two sets of 17x5 terminals, where the terminals in the same column are connected to one another at all times. As this breadboard is solder-free and only requires the wires or resistors to be inserted into the terminals, it is very easy to reconfigure and to switch out resistors to adjust the extent of voltage dividing. I show the electronic connections of this upgraded voltage divider in Figure 4.6. Based on these connections, the voltage read by the galvo servo drivers will be the sum of voltages across the 1 MΩ resistor V_{PCI} and the 1/10 kΩ resistor $V_{divided,USB6001}$ on the right of Figure 4.6. When using the PCI coarse control to align the photoexcitation beam, $V_{USB6001}$ will be set to 0. Once the alignment is complete, V_{PCI} will not be changed for the rest of the experiment. When running SO-FSRS scans, only $V_{divided,USB6001}$ will be altered to scan the photoexcitation beam in a raster manner.

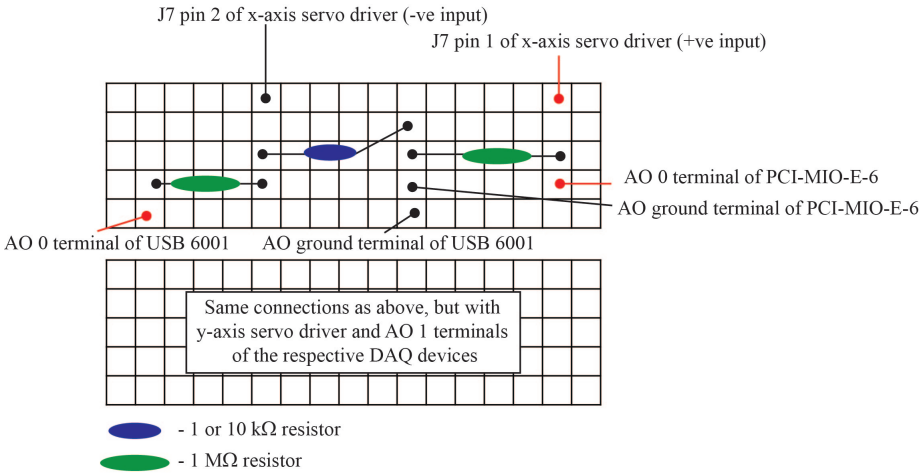

Figure 4.6: Schematic showing how the voltage divider is put together on a breadboard. All the slots within the same column of the breadboard are connected and connections in the same column are connected in series. The PCI-MIO-E-6 voltage output is sent to a 1 MΩ resistor, which serves as a coarse adjustment for aligning the 2D galvomirrors. The USB 6001 voltage out is shared between a 1 MΩ and 1 or 10 kΩ resistor in series.

4.3 LabView Code for Data Acquisition

4.3.1 Read code speed

In order to communicate with the DAQ cards through LabView, I downloaded the NI-DAQmx drivers available on Ni.com website. Fortunately for us, NI-DAQmx is very user-friendly and we use the 'DAQ assist' vi in LabView to help configure our system. The DAQ assist generates a DAQ assist vi that will produce a constant analog voltage output (in Volts) that is equivalent to the numerical indicator when the LabView program calls for it. The output will change only when another LabView command overwrites the previous value or if the computer is turned off. This vi can be converted to a string of LabView code by right-clicking it and selecting the 'generate code' option. While the speed at which the DAQ assist vi and the generated code executes is probably similar and almost instantaneous, I wanted to test out which is faster because small amounts of time saved for each command may accumulate to a significant amount for

long SO-FSRS experiments. To do so, I place the code to be timed in a flat sequence between two 'Tick Count (ms)' vi. Each tick count vi returns the microsecond value of the computer's internal clock, and the difference between the values returned before and after executing the code is the time (in microseconds) it took to execute the code.

I timed the execution of 4 different variations of the code: DAQ assist vis, DAQ assist vis nested within a sub vi, generated code, and generated code nested within a sub vi. I ran each code 10 times and recorded the execution times as summarized in Table 4.2.

We can see that the first execution time is significantly longer than subsequent ones for all scenarios except the generated code that communicates with the DAQ card directly. This is because the first execution involves initializing the program, which subsequent executions did not need to do. There is no initial lag time for the generated code since it does not need to jump through any LabView hierarchy before communicating directly with the DAQ card. Subsequent executions average 2-3 ms, thus there were hardly any differences for each of the 4 versions. In the end, I decided to use the generated code in sub vi version because it is slightly faster than the DAQ assist options, but is neater than the generated code on its own. I find the ability to keep the overall LabView code neat a very valuable feature because it is very easy for LabView codes to get messy and unreadable.

Table 4.2: Time (ms) it takes to generate an analog output command based on different LabView codes.

	DAQ Assist	DAQ Assist sub VI	Generated Code	Generated Code sub VI
	36	49	3	35
	3	3	2	3
	3	3	3	3
	3	2	2	2
	2	3	2	3
	3	3	3	3
	3	2	2	2
	3	2	3	2
	3	2	3	3
	3	3	2	2
average	6.2	7.2	2.5	5.8

4.3.2 Incorporating DAQ LabView Drivers onto Existing Data Acquisition Program

There were 2 ways to go about acquiring SO-FSRS spectra - one to run a FSRS experiment at each photoexcitation position before moving on to the next photoexcitation position in a raster scan manner, or to measure the FSR spectra of all photoexcitation positions at a set time delay before moving to the next time delay. Since it takes significantly less time to adjust the 2D galvomirror angles (on the order of mrad) than to move the time delay stage of the photoexcitation pulse (on the order of 10 mm), I decided to go with the latter.

The existing LabView code runs a FSRS experiment with a six-frame stacked sequence: a) move the time delay stage to the corresponding time delay between the

photoexcitation pulse and the Raman probe pulse, b) open the shutter in the photoexcitation beam path, c) set the file path to 'directory\name_time point_exe+set number' and acquire the data, d) close the shutter, e) write the acquired data into 3 columns (Raman gain, probe spectrum with Raman pump off, probe spectrum with Raman pump on) and save it as a file in the path set in (c), f) subtract the ground state spectrum from the excited state spectrum and display the subtracted spectrum in the graph in the main data acquisition window, g) calculate Raman gain between two cursors for the graph shown in (f).

I modified the code to add a frame between frames (a) and (b). I then inserted the sub_vi for controlling the analog outputs of the DAQ card in this new frame, i.e. set the photoexcitation after the time delay is set but before the shutter is opened. For the voltage divider that only involved PCI-MIO-E-6, the file path in frame (c) was set to 'directory\name_voltage across x-axis+voltage across y-axis_time point_exe+set number'. For the latest voltage divider with 2 DAQ cards, the file path was set to 'directory\name_ x pixel number+y pixel number_time point_exe+set number'. All other codes remained the same.

As SO-FSRS experiments take hours or days to complete, the LabView program takes up a lot of memory on the computer and significantly slows it down. For example, a 3000 image acquisition that should take 3s to acquire could take longer than 20s. Furthermore, when the acquisition is done, the LabView program will crash when the 'exit' button is clicked to shut down the program. Thus, I further modified the code to split the acquisition into multiple sessions, with the computer restarted in between sessions so that the memory could reset.

4.4 Incorporating Galvosystem onto Existing Laser Setup and How to Align It

Figure 4.7 depicts a chronological evolution of the laser table setup as I worked on figuring out the alignment. I used setups (a) and (b) with a laser pointer for safety reasons because the galvomirrors could send the beam out of the containment zone during the initial setup phase. I wanted to ensure that the alignment was contained before turning on the ultrafast laser. In all arrangements, the photoexcitation beam gets reflected off the y-axis mirror first before being sent towards the microscope through the x-axis mirror.

From (a)-(c), I attempted to align the galvomirrors without adjusting the V_x and V_y analog outputs and I was only using the mirrors prior to the galvomirrors for the alignment. When working with setup a, I thought that one issue was that the mirrors were a little far from the microscope, and a small change in mirror angles led to larger change in the spatial position of the photoexcitation beam. Thus, I moved on to setup b, where the galvomirrors were a lot nearer to the microscope. However, the photoexcitation beam was sent into the microscope at an angle as opposed to being sent in at 90° like the Raman probe and pump pulses. One issue I kept running into on setup b was the constant clipping of the photoexcitation beam at the 1" mirrors of the periscope used to guide the laser pulses into the microscope. Furthermore, I noticed that adding so much path length to the photoexcitation beam meant that the t_0 position on the time delay stage will be larger to compensate for this additional length. This meant that we would be unable to probe larger time delays after photoexcitation, which might prevent us from looking at exciton diffusion that occurs on a timescale of hundreds of picoseconds.

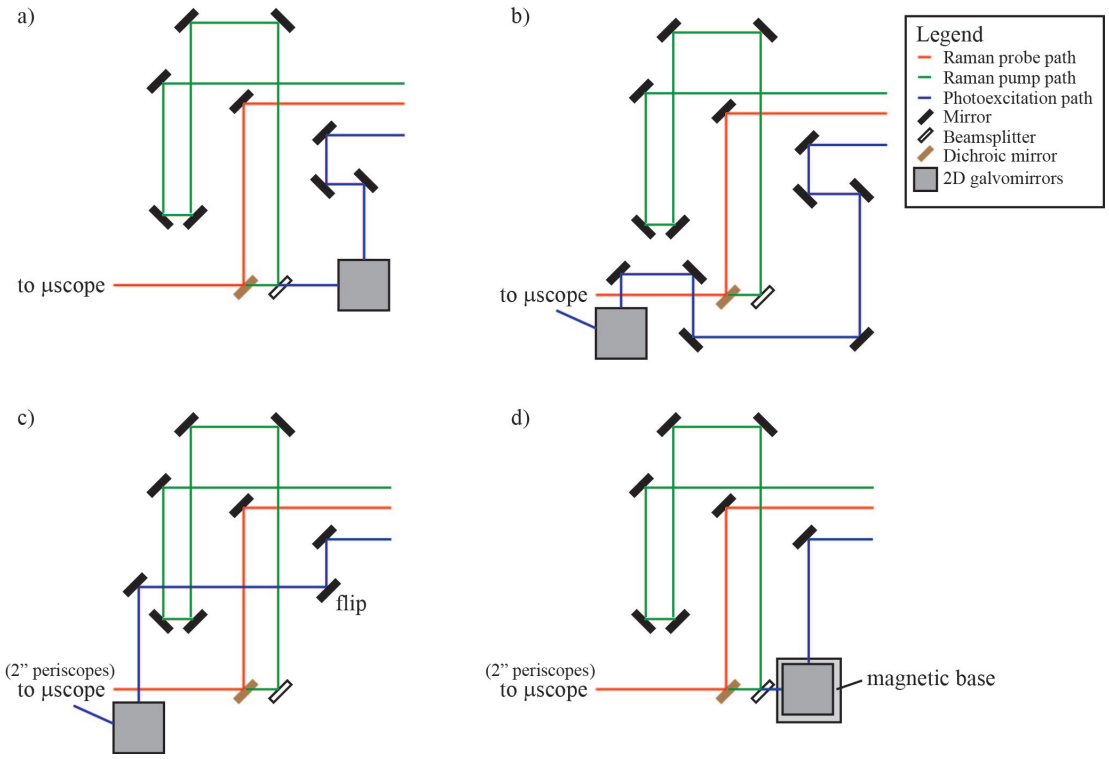

Figure 4.7: Different arrangements tested out for aligning the galvomirrors in chronological order. Schematics are not drawn to scale. (a)-(c) were problematic for these reasons:(a) the mirrors were too far from the microscope (b) the path length of the photoexcitation beam has been increased by too much (c) Insufficient degrees of freedom. (d) The final arrangement where the galvomirrors are placed on a magnetic base as close as possible to the microscope while being relatively collinear with the Raman probe and pump paths. The galvomirrors were directly used to help align the photoexcitation pulse to spatially overlap with the other two pulses.

Thus, for setup c, I decided to change the periscope mirrors to 2" mirrors to provide more space for the photoexcitation beam to navigate before entering the microscope. I also shortened the beam path by inserting a flip mirror that cuts into the photoexcitation beam path for standard FSRS experiments. Through this setup, I managed to get the photoexcitation beam to be in the vicinity of the Raman probe. However, each time the beam would start clipping before I can get it fully overlapped with the Raman probe. Things that I have tried include checking the dimensions of the galvomirror and

setting the height of the x-axis mirror to be at the same height as all other mirrors (5") and placing two irises between the mirrors and periscope to ensure that all beams are entering the microscope straight. When the spatial overlaps became close but not close enough, I was tempted to adjust both the Raman probe and pump positions to accommodate the photoexcitation beam. However, I did not do so because the key to collecting FSR spectra is the Raman probe spectrum. If I changed the Raman probe position to match the photoexcitation beam, the Raman probe would no longer be entering the microscope straight and there would be no guarantees that the spatial alignment of all three beams would stay constant at different focusing distances.

Therefore, I moved on to setup d, where I set the galvomirrors on a magnetic base so it could be switched out easily with a silver mirror used in standard FSRS experiment. I placed the galvomirrors as close to the microscope as possible while ensuring that the photoexcitation beam was relatively collinear with the other two beams. I also made modifications to the voltage divider (see Section 4.2.4) such that I would use the LabView code to directly control the galvomirrors like mirror knobs to align the photoexcitation beam in a standard FSRS experiment. The voltage setting for the x- and y-axis mirror is no longer 0 V at the origin position i.e. $V_{x,0}$ and $V_{y,0} \neq 0$. With this, the photoexcitation could now be reliably aligned spatially with the Raman probe and pump for the galvomirror setup.

4.5 How does t_0 Change with Spatial Position

While it is unlikely for the t_0 and time resolution to change when the photoexcitation beam position is changed, I wanted to confirm that experimentally. In this scenario, the time resolution refers to the smallest time step that can be distinguished between the photoexcitation pulse and the Raman probe and is measured by the FWHM of the Kerr measurement detailed in Section 2.4.2. Thus, I measured the t_0 and the time resolution in a 5×5 grid, where $V_{x,0}$ = -0.248 V and $V_{y,0}$ = 0.256 V. V_x and V_y were scanned

from -0.258 V to -0.238 V and 0.246 V to 0.266 V respectively in step sizes of 5 mV. Details on how t_0 is defined and how it is measured are covered in Section 2.4.2. The results are summarized in Tables 4.3 and 4.4.

Table 4.3: Time delay stage position (mm) at t_0 in a 5×5 grid. The top row shows the coordinates along the y-axis while the left column shows the coordinates along the x-axis. Two values are listed when a secondary peak is distinguishable from the primary one.

	-2	-1	0	1	2
-2	101.499/101.515	101.499	101.499	202. 497	101.498
-1	101.499/101.517	101.499	101.500	101.498	101.501
0	101.499/101.519	101.501	101.499	101.501	101.503
1	101.503/101.520	101.501	101.501	101.502	101.503/101.521
2	101.504/101.521	101.503/101.521	101.502	101.505/101.521	101.503/101.522

Table 4.4: Time resolution (fs) in a 5×5 grid. The top row shows the coordinates along the y-axis while the left column shows the coordinates along the x-axis.

	-2	-1	0	1	2
-2	198	204.6	211.2	217.8	211.2
-1	204.6	198	158.4	198	211.2
0	204.6	198	165	217.8	211.2
1	204.6	198	198	204.6	204.6
2	198	204.6	211.2	211.2	198

From both tables, we can see that while the optical Kerr effect measurement did not yield identical results, the t_0 and time resolution varied by only small amounts. When dealing with exciton transport that occurs at longer time scales, this is unlikely to cause much issue in the data analysis. Thus, I decided that it is not a requirement to measure the t_0 across multiple photoexcitation locations for each SO-FSRS experiment and doing that measurement once at the origin position should be sufficient.

4.6 Normalizing SO-FSR Spectra with respect to Photoexcitation Power

While the changes in t_0 and time resolution may be negligible for different photoexcitation positions, the same cannot be said for the photoexcitation power. When I was running SO-FSRS experiments in 3×3 to 7×7 grids, it was feasible to measure the power of the photoexcitation beam at all positions. I would tape a power meter head at the sample position on the microscope stage, set the power meter to measure the average power over 1-10s and take ∼5 sets of measurements for each position.

However, for larger acquisitions such as a 15×15 grid, I only measured the powers at 9 positions (origin and the edges) and extrapolated the power for the other positions. Sometimes, I would do the same for 3 time delays, usually 0ps, 100ps and 500ps, to ensure that the power does not change much at different time delays. If the change is significant, I would also extrapolate the power of each position for each time delay.

To normalize the SO-FSR spectra with respect to photoexcitation power, I divide the intensities of the fitted Raman peaks by the corresponding photoexcitation power to get a unit of 'Raman gain/μW.

4.7 Processing and Analyzing SO-FSRS data

To process the SO-FSRS data, I wrote and edited LabView, Python and Igor codes. To keep the data organized, I have a main folder named after the sample and the grid size of the SO-FSRS experiment. Within this folder are five sub folders - raw data, batch, average, subbed, ta - where the raw data were directly written into the 'raw data' folder.

After a SO-FSRS experiment, I used 'SO-FSRS Analysis 3.0.vi' to process the raw data. Figure 4.8 shows the first panel of this code. The first step is to load the calibrated x-axis and list of time delays in the 'shiftx' and 'time points' portion at the top right corner. Next, the experimental parameters, such as 'file name' and number of sets, are

entered in the right of the panel. If the 'file name' is too long, a shorter string can be typed into the 'shorter name' indicator. If not, an identical string as the 'file name' should be typed in.

Next, I set the 'Main folder' to the raw data folder. After some loading time, the list beside the first graph will show a list of all the raw data files. To visualize any of the raw data, I would select the file of interest in the 'File Names' drop box and click load. The graph would then display three spectra on top of one another - the Raman gain, Raman probe spectrum with Raman pump off, and Raman probe spectrum with Raman pump on. Each of these three spectra are saved as a column of data in the raw data file.

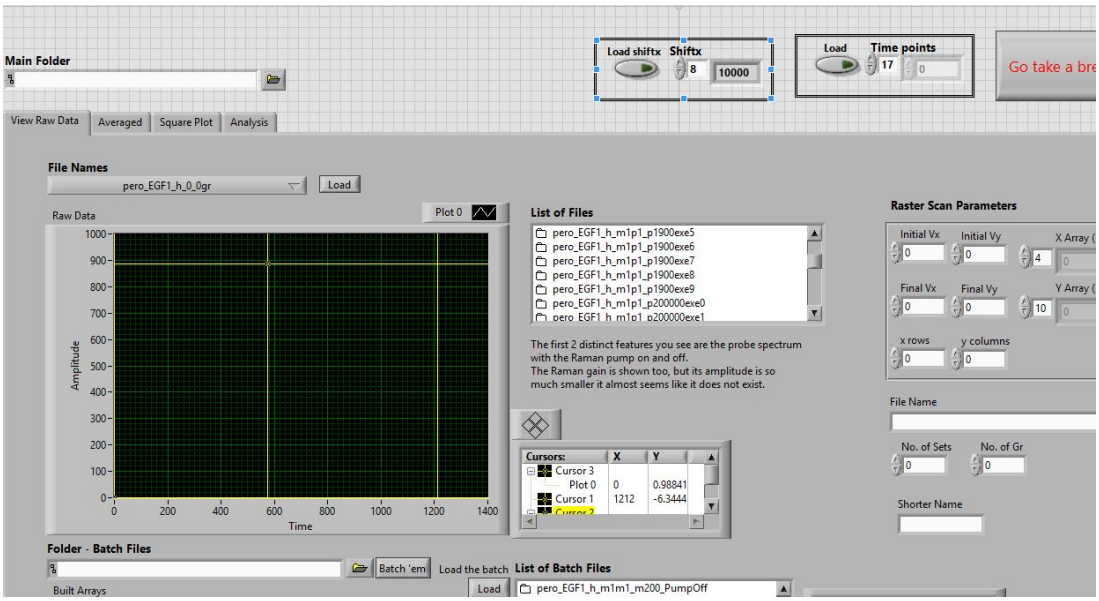

Figure 4.8: First panel of the 'SO-FSRS Analysis 3.0.vi'. Things that can be done in this panel include defining the initial parameters (x-axis calibration, time delays, experimental parameters etc.), visualize raw data and creating batch files.

To prepare the raw data files for analyses, I need to separate each column and group them with repetitions of the same time delay and photoexcitation position (e.g. put all ground state Raman gain spectra in a single file). To do so, I first set the 'Folder -

Batch Files' to the 'batch' folder mentioned earlier. Next, I will click on 'Batch 'em'. This will generate 3 files for each time delay and photoexcitation position, where

- file name_PumpOff = sets of Raman probe spectra with Raman pump off
- file name_PumpOn = sets of Raman probe spectra with Raman pump on
- file name_RG = sets of Raman gain spectra.

These files are automatically saved in the 'batch folder'.

Next, I would exclude any spectra that are outliers, such as flipped spectra or blanks, within each of these 'batched' file, and get the average of the remaining spectra to improve signal-to-noise ratio of the spectra to be analyzed. This step is done through Python and the resulting averaged files are saved in the 'average' folder.

Next, I return to the LabView program and go to the second panel as shown in Figure 4.9. After setting the folder indicators in LabView to 'average', 'subbed' and 'ta' respectively, I clicked on the rectangular 'Subtract' boolean to generate one-to-one subtractions of the ground state spectrum from each excited spectra. The subtracted spectra are saved and written as individual files in the 'subbed' files. Next, by clicking on the rectangular 'TA' boolean, I would generate the transient absorption spectra at each time delay and photoexcitation position. To visualize either an averaged spectrum or a subtracted file, I would scroll down and select the file of interest, and click 'Load'. The corresponding spectrum will be shown in the graphs plotted against the calibrated x-axis in cm^{-1}. This concludes the initial processing of SO-FSR spectra.

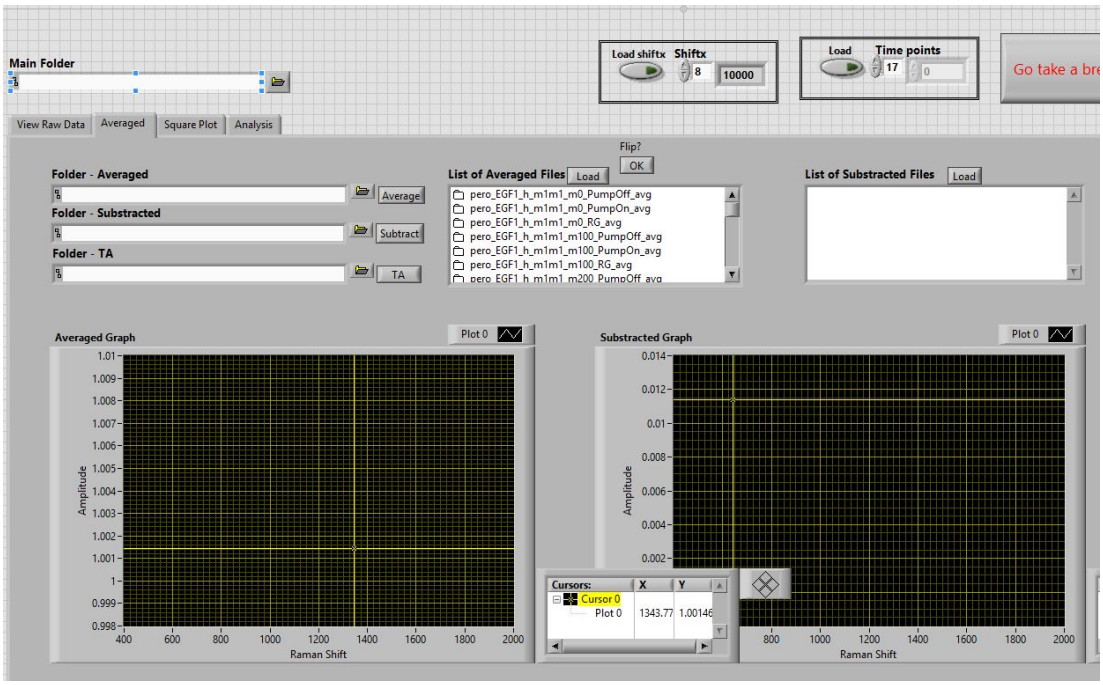

Figure 4.9: Second panel of the 'SO-FSRS Analysis 3.0.vi'. This panel is used to generated subtracted excited state and transient absorption spectra.

To look at a rudimentary Raman image at selected Raman shift value and time delay, I go to the third panel of the LabView program as shown in Figure 4.10. The Raman shift value can be set by typing in its corresponding pixel position while the time delay can be selected in the drop box at the top of the panel. After initializing this portion of the code with the 'start' button, I would generate an intensity map and a 3D maps on the left and right graph panels respectively. As this Raman map is generated from the excited state spectra prior to any peak fitting, it only provides a general idea on if there are any exciton transport observed.

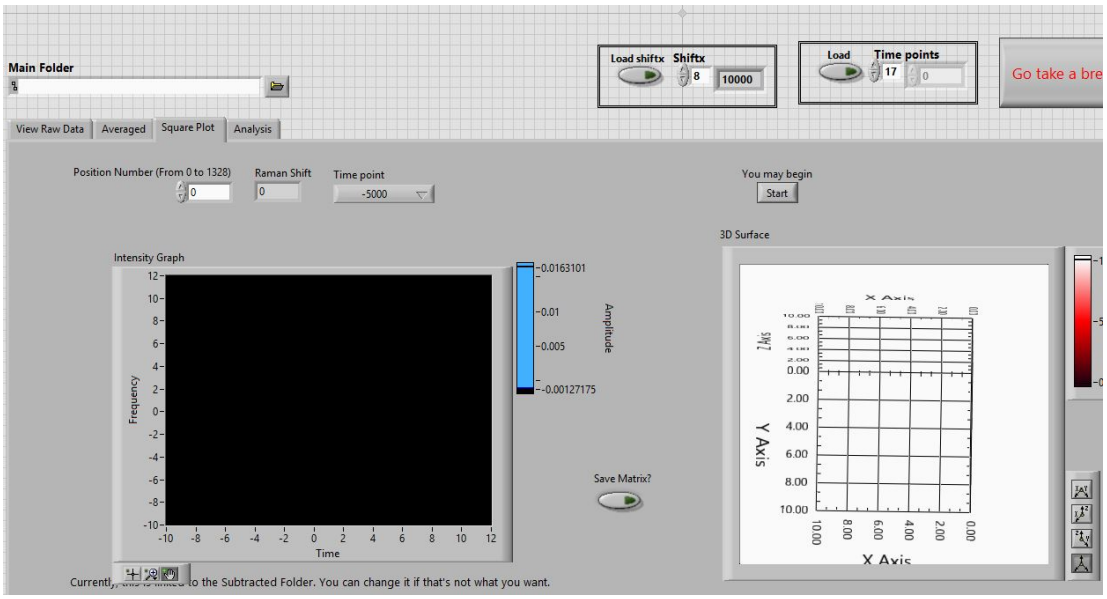

Figure 4.10: Third panel of the 'SO-FSRS Analysis 3.0.vi'. This panel is used to generate a rudimentary Raman image at the selected Raman shift value and time delay.

To analyze the SO-FSR spectra, I would import the subtracted spectra into Igor and use modified Igor macros to perform standard FSRS analysis. If Raman features are observed on top of a strong background, I would fit the background with an appropriate polynomial before removing it, and repeat the procedure using the same parameters for all spectra. Afterwards, the Raman features would be fitted to gaussian functions. As the intensities of the Raman features reflect the populations of either the ground or excited state, I would plot their intensities against the time delays to observe how the population dynamics evolve over time. How these graphs can be interpreted would be covered in more details in the next chapter.

4.8 Conclusion

In summary, I have walked through the development of SO-FSRS in this chapter, from hardware selection to data analysis. Developing a brand new experimental technique involves a lot of learning, failing, and learning from the failures. I hoped to have provided a glimpse of that journey as I hit each milestone in the development of SO-FSRS. Being the first vibrationally sensitive technique that can image exciton movement, SO-FSRS is a much needed addition to the existing toolkit that studies the mechanisms of exciton transport.

Chapter 5

Spatially-Offset Femtosecond Stimulated Raman Spectroscopy: Observing Exciton Transport through a Vibrational Lens

In the previous chapter, I covered the development of SO-FSRS. Now that SO-FSRS has finally reached the point where it can be used to run imaging experiments. SO-FSRS debuted to the scientific community in a *Journal of Physical Chemistry* letter, where I demonstrated its utility on TIPS-pn, a model system that has been well-studied. The full text of the letter has been reproduced in this chapter.

5.1 Overview

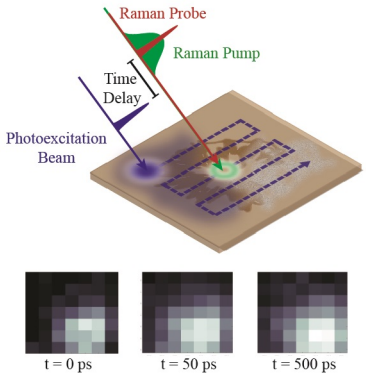

Figure 5.1: Table of content figure.

To design better molecular electronic devices, we need a strong understanding of how charges or excitons propagate, as many efficiency losses arise during transport. Exciton transport has been difficult to study because excitons tend to be short-lived, have short diffusion lengths, and can easily recombine. Here, we debut spatially offset femtosecond stimulated Raman spectroscopy (SO-FSRS), a three-pulse ultrafast microscopy technique. By offsetting the photoexcitation beam, we can monitor Raman spectral changes as a function of both time and position. We used SO-FSRS on 6,13-bis(triisopropylsilylethynyl) pentacene, a well-studied organic semiconductor used in photovoltaics and field-effect transistors. We demonstrated that the fast exciton and free charge carrier transport axes are identical and observed that exciton transport is less anisotropic by a factor of $\sim$3. SO-FSRS is the first technique that directly tracks molecular structural evolution during exciton transport, which can provide roadmaps for tailor-making molecules for specific electronic devices.

5.2 Introduction

Molecular electronics research is exciting because it provides new routes toward nanoscale electronics, [138–142] allowing us to keep up with Moore's law [143–146] or seek alternative photovoltaic technologies. [147–152] Regardless of types or applications, what all molecular electronics have in common is their ability to transport and transfer electrical charges, be it in the form of excitons (bound electronhole pairs) or free charge carriers. Exciton transport is particularly challenging to study because excitons cannot be generated simply by inserting electrodes into the material but instead are generated by external means such as heat or light. Furthermore, excitons have short lifetimes [17, 18] and short diffusion lengths, [19] making their transport difficult to detect. Despite theoretical predictions as early as 1938, [153] exciton transport was only directly observed for the first time in 1984. [154] Because excitons serve as the charge carriers for many semiconductor applications, decoding the mechanism of exciton transport can inspire new avenues for tailor-making unique molecules for specific electronic functions.

In recent years, transient absorption microscopy (TAM), also known as pump–probe microscopy or white light spectro-microscopy, has achieved the subpicosecond temporal and submicrometer spatial resolutions necessary to directly image exciton transport in organic semiconductors, [61, 136, 155–157] perovskites, [158–161] nanowires, [162–165] and other inorganic semiconductors. [166–170] These measurements gave us new physical insights, such as the cooperative nature of singlet and triplet exciton transport [155] and how exciton traps impact transport. [159, 163] However, it is difficult to span a sufficiently wide region of the electromagnetic spectrum to be on resonance with all excited and intermediate electronic states, making some of them invisible to TAM. Even when detected, electronic features can be very broad and challenging to assign to specific excited states. Furthermore, electronic spectroscopies struggle to identify key molecular motions or structural changes involved with excited state processes, making it challenging to provide insight into how to modify molecular potential energy surfaces to

improve performance. Some electronic techniques, such as two-dimensional electronic-vibrational spectroscopy and two-dimensional electronic spectroscopy, can identify vibronic couplings that strongly couple to electronic excitation, but have not yet been used to examine transport. [171, 172] Thus, molecular structural insight is needed to make use of synthetic modifications to improve function. [173]

Femtosecond stimulated Raman spectroscopy (FSRS) is a technique that provides molecular structure information about reacting photoexcited species on the ultrafast time scale. [3, 4, 174, 175] FSRS consists of three spatially overlapped laser pulses: the femtosecond photoexcitation or actinic pulse, the picosecond Raman pump pulse, and the femtosecond broadband Raman probe pulse. The photoexcitation pulse is used to generate the excited state population, after which the Raman pump and probe pulses provide stimulated Raman spectra as a function of time following photoexcitation. New Raman features that show up only in the excited state spectra can shed light on the vibrations and structures of molecules in higher-energy states, [10, 125, 176–178] while ground state Raman depletion or bleaching represents all non-ground state populations, including that of dark states that would otherwise be invisible. Following these transient Raman dynamics allows us to single out nuclear rearrangements [179–181] and vibronic couplings [175, 182] within the molecular systems studied.

Such a useful technique has yet to have its TAM counterpart. Thus, we have developed the spatially offset femtosecond stimulated Raman spectroscopy (SO-FSRS) technique to provide vibrational information complementary to that from TAM. In SO-FSRS, the positions of the Raman pump and probe beams (probing site) are held constant while we raster scan the photoexcitation beam (excitation site) as represented by a schematic in Figure 5.3. At each photoexcitation position, we collect a complete FSRS data set, which can then be processed to generate a Raman map of excited state features. As we can assign Raman features to specific vibrational motions in the molecules, [4, 70] we can track vibrational motions in both space and time with

SO-FSRS. Observing how excitons navigate through their local and heterogeneous environments, such as grain boundaries and interfaces between different materials, may help us identify specific molecular interactions or vibrational coherences that hinder or facilitate exciton transport.

5.3 Experimental Method

5.3.1 TIPS-pn crystal growth

We used $\geq$ 99.9% TIPS-pn crystals from Sigma Aldrich to prepare a 5% wt solution in toluene. We waited for the recrystallization of TIPS-pn via slow evaporation [124, 183–185] before sealing the crystals in Loctite Epoxy Instant Mix 5 Minute adhesive between two cover slips to minimize oxidation and photodamage.

5.3.2 Experimental Set-up for SO-FSRS

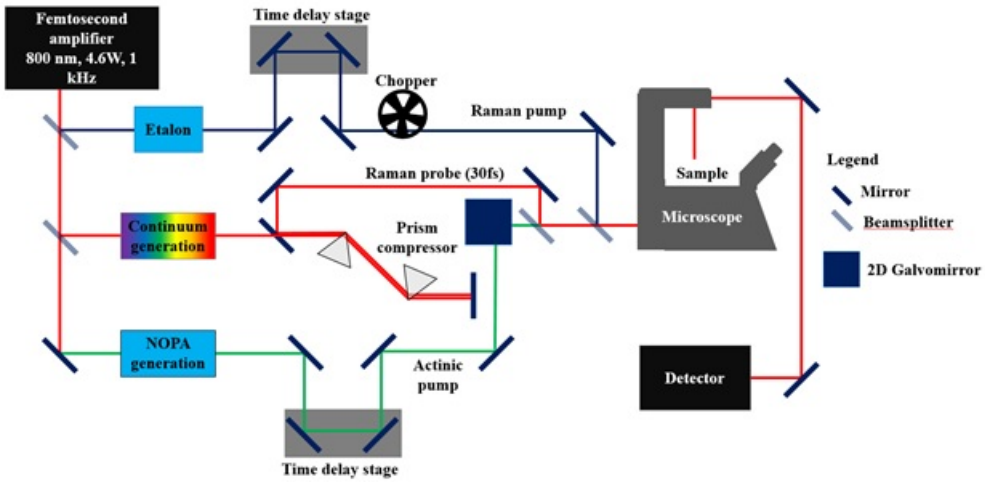

Figure 5.2: Schematic of SO-FSRS setup.

We built the SO-FSRS setup as presented in Figure 5.2 upon a home-built FSRS setup (Coherent Libra-F-1K-HE) reported in earlier works. [5, 186] We passed 2.5 mW of the

fundamental beam through a 2 mm sapphire crystal, then through a RG830 long pass filter and a fused silica prism compressor to generate the broadband femtosecond Raman probe pulse. We generated the 2.1 ps 805 nm Raman pump pulse with a full-width at half-maximum (FWHM) of 0.80 ± 0.5 nm by passing 440 mW of the fundamental beam through a custom Fabry-Perot etalon (TecOptics) setup. [5] The remaining fundamental output beam were used to generate the photoexcitation pulse by passing it through a home-built non-collinear parametric amplifier (NOPA). We generated a white light seed continuum by passing some of the output through another 2 mm sapphire crystal and a 400 nm pump pulse via frequency doubling through the beta barium borate (BBO) crystal. These two pulses are then mixed in a 1 mm BBO crystal to produce the photoexcitation pulse through non-collinear parametric amplification. The photoexcitation pulse was passed through an acousto-optic programmable dispersive filter (Dazzler, Fastlite) [187, 188] and a SF10 prism compressor to compensate for temporal chirp. We tuned the central wavelength of the photoexcitation pulse to 532 nm with a Gaussian spectral shape and a FWHM of 13.00 ± 0.1 nm. The Raman probe (5.8 μW), Raman pump (49.3 μW) and photo-excitation beam (28 μW) were sent through an inverted Olympus IX-73 microscope and focused on the sample in a non-collinear fashion using an Olympus Plan $40\times/0.65$ objective. We define the time delays as the duration between the interactions of the Raman probe and the photoexcitation beam with the sample. The cross-correlation at the sample position between the Raman probe and photo-excitation beam was 152 fs. The central position of the photoexcitation beam is controlled by a ThorLabs GVS012 galvomirror paired with a National Instrument PCI-MIO-16E-4 data acquisition card. By placing the ThorLabs GVS012 2D galvomirror on a magnetic base, we could easily switch back and forth between the FSRS and SO-FSRS setup. The 2D galvomirror consists of an x-axis and a y-axis mirror, each connected to a separate servo-driver. The servo-drivers are then connected to a National Instrument PCI-MIO-16E-4 data acquisition (DAQ) card via a National Instrument screw terminal block. Analog voltage outputs generated by the DAQ card signal the servo-drivers to

rotate the x- or y- mirrors by angles determined by the 0.5V/° ratio. A home-built LabView program is used to raster scan the photoexcitation beam and collect FSR spectra at each photoexcitation location. The FSR signal were directed out of the Olympus IX 73 microscope into a 1/3 m Instruments SA, Inc (now renamed to Horiba) 10-320 spectrograph and collected on a Princeton Instruments PIXIS 100F CCD array.

We wrote a home-built LabView program to collect the FSR spectra (average of 8 data sets) at various time delays in a randomized order for 3 seconds. We obtained the Raman gain spectra by dividing the probe spectra with the Raman pump on over the probe spectra with the Raman pump off. We also obtained the transient absorption spectra from the transmittance of the probe spectrum when the Raman pump was blocked by the chopper blade. We collected the SO-FSR spectra of TIPS-pn at 48 time delays from -5 ps to 500 ps in a 7×7 grid, with V_x values ranging from -235 mV to -205 mV and V_y values ranging from 29 mV to 59 mV, translating to a 9 μm step size in both directions. All data presented in this paper were collected from a single TIPS-pn crystal, albeit at different locations of the same crystal. We performed our data analysis using a combination of self-written LabView, Igor and MatLab codes.

5.4 Results and Discussion

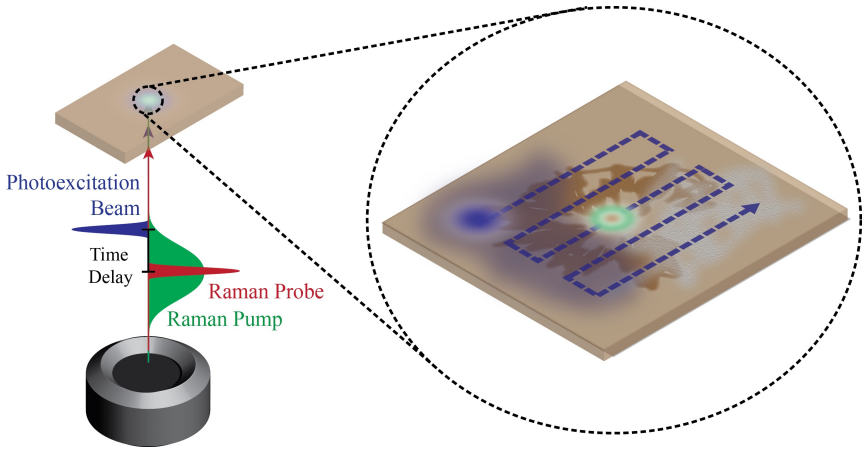

Figure 5.3: Schematic of a raster scan performed by SO-FSRS across a heterogeneous surface. The photoexcitation beam is scanned across the surface while the probing region remains fixed to monitor exciton diffusion.

To demonstrate the utility of this new technique, we monitored exciton transport dynamics in 6,13-bis(triisopropylsilylethynyl) pentacene (TIPS-pn). TIPS-pn is a useful test case because it has been well-studied for its field-effect transistor applications, [189–195] is known to exhibit charge transport anisotropy, [194–196] and undergoes singlet fission that generates long-lived triplet states. [7, 116, 197–200] Moreover, polarized Raman measurements have been useful for identifying how the TIPS-pn molecules are oriented within a microscopic crystal, [189, 191, 201, 202] allowing us to identify the fast charge transport axis easily without running charge mobility experiments. Here we demonstrate that we have successfully developed SO-FSRS and gained new physical insight into exciton transport in TIPS-pn. We show that while the fast exciton transport and fast free charge carrier transport axes are identical in TIPS-pn, excitons display less anisotropy in transport than do free charge carriers.

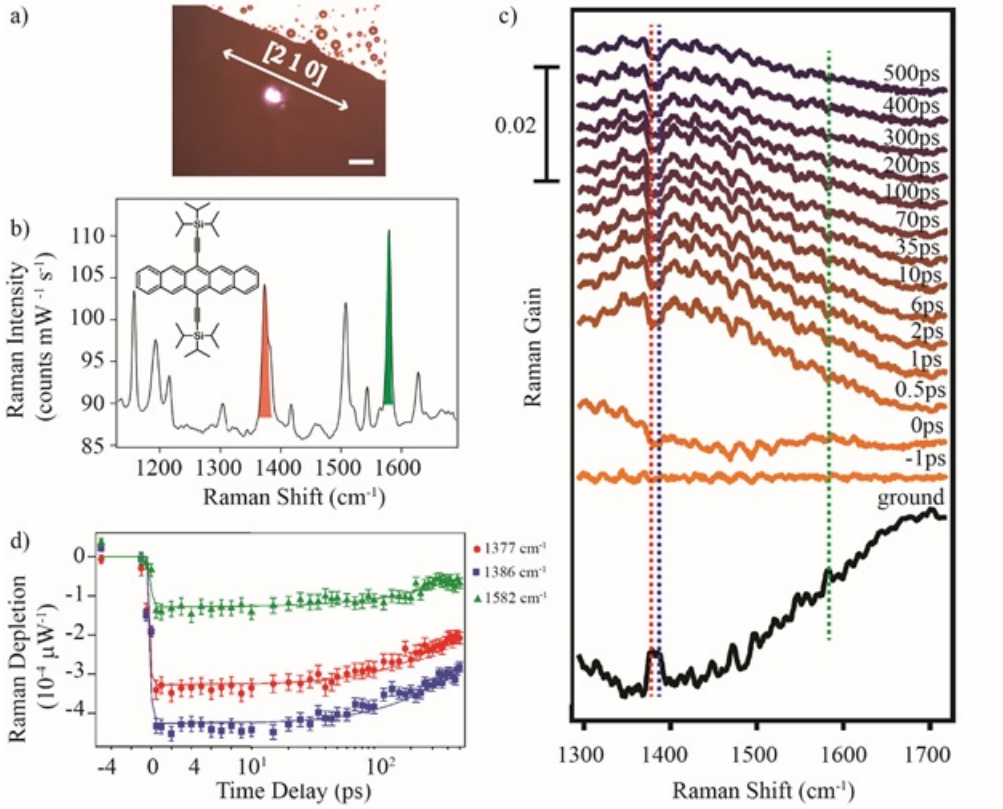

Figure 5.4: (a) Optical image of the TIPS-pn crystal used for all measurements. The scale bar depicts 100 μm. (b) Spontaneous Raman spectrum of TIPS-pn at 240° laser polarization with respect to the laboratory horizontal axis. The intensities of the 1373 (red) and 1578 cm^{-1} (green) modes are sensitive to the laser polarization and can be used to determine the crystal axis orientation. The inset shows the chemical structure of TIPS-pn. (c) Excited state FSR spectra of the TIPS-pn crystal at multiple time delays at the central (0, 0) position, where the spatial overlap between the photoexcitation and Raman probe pulse is maximal. The spectra are offset from one another for the sake of clarity. Laser pulses used to generate these spectra are p-polarized. (d) Raman depletion dynamics of three ground state peaks at the central (0, 0) position in terms of unitless amplitude per microwatt of photoexcitation power. The x-axis is linear from 5 to 10 ps and logarithmic from 10 to 500 ps.

We show spectroscopic characterization of the TIPS-pn crystal used for SO-FSRS in Figure 5.4, including an optical image in Figure 5.4a. Figure 5.4b displays a spontaneous Raman spectrum of TIPS-pn collected at 240° laser polarization relative to the

horizontal laboratory axis. As the 1373 (red) and 1578 cm^{-1} (green) modes correspond to C=C molecular vibrations along the short and long axis of the pentacene backbone, respectively, their intensities are sensitive to laser polarization. [189,191,201,202] By tracking their intensity dependences on the laser polarization angle, we identified the [210] crystallographic axis to be parallel to the long side of our TIPS-pn crystal, as shown in Figure 5.4a. Details can be found in Figure B.1. The [210] axis, which matches the crystallographic a axis of TIPS-pn, [203] has been demonstrated to be the fast charge transport axis for TIPS-pn due to favorable π-π interactions between the pentacene backbones. [194, 195, 202] As those studies were conducted with free charge carriers, we did not want to assume that excitons will behave identically. [204–206] Nonetheless, because exciton transport boils down to intermolecular electronic energy transfers, [207,208] the strong π-π interactions, which arise from decreased distances between the pentacene backbones, will increase the probability of energy transfer through quantum tunneling.

Equipped with some basic information about our crystal, we proceeded with our SO-FSRS experiment at 532 nm photoexcitation. The photoexcitation beam was raster scanned in a 7 $\times$ 7 grid, with each grid position representing the central position of the photoexcitation beam and being 9 μm apart from the next. We sealed the TIPS-pn crystal in epoxy to minimize photodamage during the measurement. The Raman probe position relative to the [210] axis under 10$\times$ magnification is shown in Figure 5.4a. As the beam diameters of the three pulses are larger than the step size of 9 μm under 40$\times$ magnification, we defined the (0, 0) position as the location with maximum spatial overlap between the photoexcitation and Raman probe pulses. We used a 2D galvomirror to control the position of the photoexcitation beam while holding the positions of the other two beams constant. This is the opposite of the TAM convention where the pump is held constant because it is not trivial to simultaneously change the positions of both the Raman pump and probe pulses while ensuring that their overlap stays the same. Therefore, we are always probing the same location in SO-FSRS and waiting for

excitons generated outside the probing region to migrate into it. We performed eight sets of measurements under 40× magnification with a 1 kHz repetition rate Ti:sapphire laser at 48 time delays at each photoexcitation position, accumulating 19.5 h in data acquisition time for a complete SO-FSRS data set.

Figure 5.4c shows the excited state FSR spectra obtained at the (0, 0) position, while corresponding time-resolved spectral data sets obtained at (2, 4) and (2, 2) are shown in Figure B.4 for comparison. We present these spectra after one-to-one subtraction of the ground state spectrum to keep from overwhelming the excited state signal with the signal from the residual ground state molecules. The relative intensities of Raman peaks observed in the stimulated ground state Raman spectrum in Figure 5.4c are different than its spontaneous Raman counterpart in Figure 5.4a due to differences in laser polarization. Although we do not observe new Raman features in the excited state spectra, the Raman depletions or ground state bleaches contain a wealth of information because they represent the dynamics of all non-ground state populations. We argue that Raman depletions have not been given enough attention within the FSRS community; our subsequent analyses rely only on Raman depletions, yet we extracted and gained new physical insights into exciton transport in TIPS-pn. Looking closely at Figure 5.4d, we see that the 1377, 1386, and 1582 cm^{-1} Raman depletions are the most negative at around 0.5 ps, indicating the time when the excited state population generated at the (0, 0) position region peaked. This likely corresponds to the generation of a mixture of excited singlet and correlated triplet pair excitons through singlet fission in TIPS-pn. [136, 197, 209–211] The Raman depletions become less negative at later time delays because the excited states either propagate out of the (0, 0) probing region or decay back to the ground state. We also observe that more than half of the initially excited molecules have yet to return to the ground state even 500 ps after photoexcitation because the singlet fission-induced excitons eventually convert to long-lived triplet states with lifetimes of up to a few microseconds. [209] We fit the ground state depletion dynamics to a single-exponential decay convoluted with the cross correlation between the

photoexcitation beam and the Raman probe. The time decay constants are 0.91 ± 0.06, 1.12 ± 0.05, and 0.58 ± 0.06 ns for the 1377, 1386, and 1582 cm^{-1} modes, respectively, consistent with long triplet lifetimes observed in TIPS-pn. [136, 192, 197, 209–211]

To better explain how depletion dynamics can reflect exciton diffusion, we made a simple schematic in Figure 5.5 based on three hypothetical situations: when the spatial overlaps between the photoexcitation beam and the Raman probe pulse are maximal, along the fast exciton transport axis, and along the slow exciton transport axis. The Raman pump pulse, which is always spatially and temporally overlapped with the Raman probe pulse, is not depicted in Figure 5.5. Calculations on how we estimated the initial exciton density can be found in the Supporting Information. In all scenarios represented in Figure 5.5, an initial exciton population is generated within the photoexcitation region at t = 0 ps. After some time, the excitons either return to the ground state or diffuse out of the initial photoexcitation region, with a larger portion migrating along the fast transport axis. In the first scenario where there is maximum overlap between the probing and the excitation regions, the number of excitons within the probing region decreases steadily with respect to time, corresponding to a gradual ground state population recovery as observed in the dynamics in Figure 5.4d. When the excitation and probing regions are partially overlapped, the initial excited state population "seen" by the Raman probe is smaller despite there being the same number of excitons generated by the photoexcitation beam. As some of the excitons generated outside the probing region will migrate into it over time, it appears as if the excited state population is decaying at a slower rate or even growing initially if the overlap is along the fast transport axis. As SO-FSRS keeps the probing region constant, the direction of all perceived exciton transport, as indicated by the blue arrows, is toward the (0, 0) central position and not vice versa.

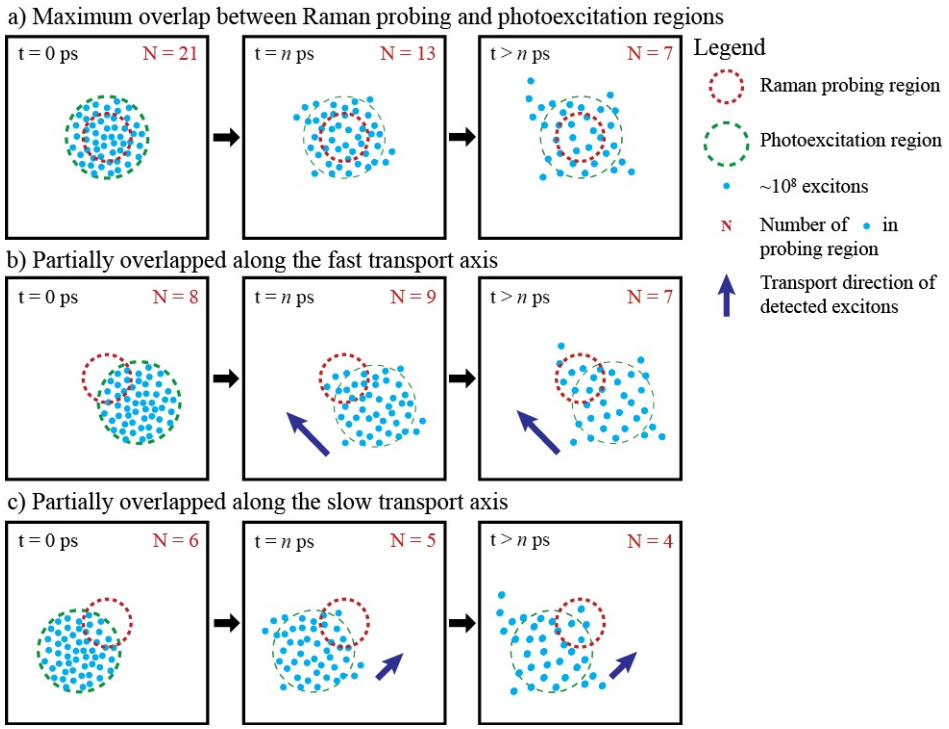

Figure 5.5: Schematic showing the evolution of the excited state population within the probing region when the spatial overlap between the photoexcitation beam and Raman probe is (a) at a maximum, (b) along the fast transport axis, and (c) along the slow transport axis. In addition to diffusing out of the initial photoexcitation region, the total number of excitons present in each panel decreases as time passes because excitons are also decaying back to the ground state. Only excitons within the probing region are observed in our SO-FSRS experiments.

Keeping Figure 5.5 in mind, we identified the fast and slow exciton transport axes in TIPS-pn by comparing the time decay constants of the 1377, 1386, and 1582 cm^{-1} modes at the central (0, 0) position with those of its eight neighboring positions as shown in Table 1. For each photoexcitation position, we performed the same data analysis as described for Figure 5.4d and obtained the time decay constants by fitting the Raman depletion dynamics to a single-exponential decay convoluted with the cross correlation between the photoexcitation and Raman probe pulses. We see that in almost all cases, the spatially offset positions yield a longer decay time constant. This suggests that

charges generated outside the probing region are indeed migrating into the probing region, increasing the lifetime of the collective excited states as new states are replenishing those that have returned to the ground state or propagated away. In all of the ground state peaks analyzed, the (1, 1) position had the largest time decay constant, meaning that excitons generated in that position had migrated most quickly into the probing region. Referencing Figure 5.4a, we see that (1, 1) is along the [210] axis, indicating that the fast exciton transport axis matches the fast free charge carrier transport axis as expected. On the basis of our data in Table 5.1, the lifetimes of the collective excited states increased an average of 30 $\pm$ 10% and 90 $\pm$ 30% along the slow and fast exciton transport axes, respectively, which is lower than a charge mobility anisotropy of $\sim$10 observed for free charge carriers in TIPS-pn. [194, 195] In fact, Zhu et al. previously observed qualitatively similar exciton transport anisotropy in TIPS-pn with TAM, although they did not comment on it. [136] This implies that while an increased number of π–π interactions along the [210] crystallographic axis facilitates transport for both free charge carriers and excitons in TIPS-pn, they play a smaller role in exciton transport, leading to only a 3-fold instead of a 10-fold improvement along the fast transport axis when compared to the slow axis. One possible explanation is that excitons can be delocalized over multiple molecules, [20, 212] resulting in a smaller difference between the strengths of π-π interactions along the [210] axis and its perpendicular axis.

Table 5.1: Time Decay Constants (in nanoseconds) of 1377, 1386, and 1582 cm^{-1} Depletion at Positions (1, 1) to (1, 1).

1377 cm^{-1}			
	y position -1	y position 0	y position
x position -1	2.3 ± 0.5	0.91 ± 0.07	1.06 ± 0.07
x position 0	0.93 ± 0.08	0.91 ± 0.06	1.24 ± 0.08
x position 1	1.07 ± 0.10	1.04 ± 0.07	1.8 ± 0.17
1386 cm^{-1}			
	y position -1	y position 0	y position
x position -1	0.99 ± 0.5	0.83 ± 0.03	1.41 ± 0.08
x position 0	1.00 ± 0.05	1.12 ± 0.05	1.58 ± 0.09
x position 1	1.24 ± 0.07	1.32 ± 0.07	2.12 ± 0.17
1582 cm^{-1}			
	y position -1	y position 0	y position
x position -1	0.9 ± 0.3	1.0 ± 0.5	1.0 ± 0.5
x position 0	0.77 ± 0.11	0.58 ± 0.06	0.81 ± 0.11
x position 1	0.76 ± 0.08	1.17 ± 0.17	1.6 ± 0.3

Another interesting observation we made from the dynamics data in Table 5.1 was that the excitons generated from the (1, 1) position seem to propagate to the probing region more rapidly than those from the (1, 1) position despite both being located along the fast transport axis. To investigate if this trend is observed for all positions, we normalized the depletion of all positions with respect to the depletion value at the (0, 0) position at each time delay. Figure 5.6a shows how the normalized fraction of the excited state population changed as time progressed, using data derived from the depletion of the 1386 cm^{-1} feature. Taking a closer look at the depletion dynamics of the 1386 cm^{-1} mode at positions (0, 0), (2, 4), and (2, 2) in Figure 5.6b, we found the ground state population recovered more slowly when the initial photoexcitation occurred

at position (2, 4) or (2, 2) than at position (0, 0) because excited states generated outside of the probing region migrated into the probing region. The excitons generated at the (2, 2) position propagated toward the (0, 0) position so rapidly that the excited state population grew and peaked only around 300 ps. We once again see that the (4, 4) to (2, 2) axis is indeed the fast exciton transport axis as the depletion dynamics observed in Figure 5.6b mirrors what we demonstrate in Figure 5.5. We repeated the analysis for 1377 and 1582 cm^{-1} modes and found similar observations as depicted in Figure B.5.

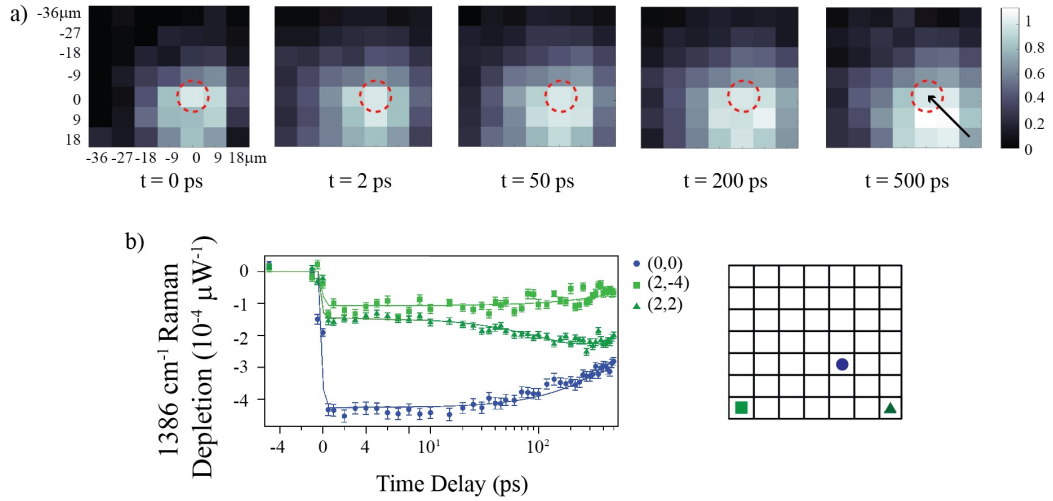

Figure 5.6: (a) Evolution of the 1386 cm^{-1} depletion magnitude normalized with respect to the depletion at the (0, 0) position over time. The dashed circle represents the Raman probe pulse and the (0, 0) position. The arrow in the rightmost panel represents the diffusion direction of the excitons generated in the (2, 2) position, which falls along the fast exciton transport axis. (b) 1386 cm^{-1} Raman depletion dynamics at three photoexcitation locations. The x-axis is linear from 5 to 10 ps and logarithmic from 10 to 500 ps. The grid on the right serves as a visual guide for the positions of each coordinate in relation to one another and the [210] axis.

These distance-dependent results are surprising because they suggest a preference for unidirectional transport along the same axis. From Figure 5.6a, we see an asymmetrical spread in excited state population over time and notice that the position with the strongest depletion has shifted from (0, 0) to (1, 0) or (1, 1). Figure B.6 shows SO-FSRS data collected from the same crystal but at a different location with a stronger

unidirectional transport characteristic. These observations were made after accounting for laser excitation power at each photoexcitation position. We did not test if laser polarization plays a role in unidirectional transport due to limitations in the transient Raman signal magnitude in polarization-dependent studies. Our current hypothesis is that we are observing preferential charge movement from a thinner region of the crystal to its thicker counterpart. However, a future study on a more carefully prepared gradient sample needs to be conducted to carefully probe this phenomenon.

5.5 Conclusion

To conclude, we have successfully developed a new technique, SO-FSRS, that allows us to follow structural evolution after photoexcitation in both space and time. We tested our technique on TIPS-pn and confirmed that its fast exciton transport axis is identical to that of free charge carriers, although increased – interactions between the pentacene backbones may play a smaller role in exciton transport. We also revealed the fast exciton transport axis of triplets in TIPS-pn, which is potentially useful in determining molecular orientation in devices that rely on triplet energy transfer, such as silicon photovoltaics sensitized by singlet fission molecules. In comparison to other techniques such as TAM, SO-FSRS has a higher chance of photodamage of the samples due to the use of low-repetition rate lasers. However, SO-FSRS possesses the molecular structural specificity lacking in many other techniques. Thus, despite the current limitations of using a low-repetition rate laser, such as longer acquisition times and higher risks of photodamage, SO-FSRS fills a crucial knowledge gap in our understanding of exciton and charge transport. Future applications of our technique include studying how excitons transfer across interfaces between different materials and exploring if any phonon modes couple with specific vibrations to drive exciton transport. We look forward to applying SO-FSRS to many more systems to discover the vibrational secrets they hold.

Chapter 6

Future Directions

In the previous two chapters, I have documented the development of SO-FSRS and demonstrated its utility using TIPS-pentacene as a model system. In this chapter, I will discuss future directions of SO-FSRS and what systems it can be used to study.

6.1 TIPS-pentacene Thickness Dependence Study

From Chapter 5 Figure 5.6a, one observation that we did not expect from the SO-FSR spectra of TIPS-pentacene was the shifting of the position with strongest depletion because it suggests a preference for unidirectional transport along the same axis. We also observed similar observations in Figures B.5 and B.6. It is obvious from Figure B.6a that the thickness of the TIPS-pentacene crystal is not uniform and that the region showing faster transport is thinner than the region with slower transport along the same axis. Given that it is exciton transport within the same crystal, the only difference between the thinner and thicker regions are the surface-to-bulk ratios. Our hypothesis is that molecules found in thinner regions of the crystal have less option to transport their energy in- and out-of-plane and are perhaps more likely to propagate in the fast transport axis. That is plausible because the SO-FSRS setup is only probing for lateral transport and does not account for transport in- or out-of-plane. While thickness

dependence of charge mobility has been observed in thin film transistors, [213–215] it has yet to be observed at a bulk level. It is exciting that we saw the possibility of thickness dependence exciton transport on a bulk level with SO-FSRS.

To test out this hypothesis, we need to perform more careful experiments and vary the thickness of TIPS-pentacene in a controlled manner. Fortunately, there are existing techniques to deposit thin films in a controlled manner to create a gradient thickness [216, 217]. It would thus be possible to modify those methods to have TIPS-pentacene films of a gradient thickness.

The thickness of the films can be characterized with atomic force microscopy before they are sealed by epoxy in preparation for SO-FSRS experiments. Spontaneous Raman imaging can then be used to link the intensities of various Raman peaks to the sample thickness.

When setting up the SO-FSRS experiment, the origin position could be set at the thicker end to minimize risk of photodamage since this position will be exposed to many hours of Raman probe and pump pulses. If there indeed is thickness-dependent preferences for excitons to migrate from the thinner to the thicker region within TIPS-pentacene, we should see the shift of the position with strongest Raman depletion towards the thinner regions of the film as observed in Figures 5.6, B.5 and B.6.

If the hypothesis is proven right, it would mean that unidirectional molecular electronics, such as photodiodes, can be designed simply by varying the thickness of TIPS-pentacene in a controlled manner. It would also be interesting to see if similar results can be replicated in other types of organic semiconductor systems.

6.2 Other Systems to Investigate

Other than TIPS-pentacene, SO-FSRS can be applied to other systems, especially if excited state Raman peaks can be observed because they can directly provide insights into the structures of excitons or intermediates.

6.2.1 Acenes

Similar to TIPS-pentacene, many acenes also undergo singlet fission. Using transient absorption microscopy, Wan et al. showed that exciton transport in single tetracene crystals occurs through the cooperation between singlet and triplet excitons as they undergo singlet fission, triplet-triplet fusion and exciton annihilation. [61] To observe what structural evolution is taking place during this cooperative transport, rubrene and pentacene are good candidates for SO-FSRS experiments.

Bera et al. showed using FSRS that triplet separation is accompanied by loss of electron density from the tetracene core in rubrene. [10] Other than looking for evidence of cooperative transport as well, it would be interesting to follow how the electron density within the tetracene core will vary during exciton transport. In another example, Hart et al. demonstrated the existence of short-lived charge-transfer intermediates in pentacene singlet fission with FSRS. [125] It would be interesting to observe how huge of a role these charge-transfer intermediates play in exciton transport within pentacene.

6.2.2 Perovskites

Since SO-FSRS is designed to track exciton transport, it is suited to study transport in photovoltaic materials. Amongst photovoltaic materials, perovskites, with formula ABX_3, are very promising contenders as their solar cell efficiencies increased rapidly from 3.8% in 2009 to 25.5% in 2021. [16, 218]

With diffusion lengths on the orders of microns, [219, 220] and high charge carrier mobility, [221, 222] charge transport in perovskites have been studied in many transient absorption-based microscopy techniques. [159, 223–227] Thus, it would be interesting to use SO-FSRS to study perovskite to look for structural insights that may be elusive to other techniques. We decided to start with methylammonium lead iodide ($MAPbI_3$) since it is one of the first perovskite materials discovered and there are theoretical and experimental spontaneous Raman information to refer to. [228–232]

Sample preparation

I prepared $MAPbI_3$ thin films and single crystals using the following methods.

I first sonicated square coverslips in distilled water, then acetone and then isopropyl alcohol for 10 minutes each to clean their surfaces. In the meantime, I prepared ∼0.75M methylammonium iodide (MAI) and lead iodide (PbI_2) in 1mL of 4:1 v/v dimethylformamide (DMF) and dimethyl sulfoxide (DMSO). I pipetted 50μL of the resulting solution on the coverslip and spincoated it at 2500 rpm for 30s. At the 5s mark, I added 200μL of toluene as antisolvent. I repeated the spincoating process 5 times to attempt to grow thicker films. After spincoating, I annealed the thin films at 80°C for 10 minutes under ambient conditions. I then sealed the film with Loctite quick set 5 minute epoxy.

Another method I tried made use of a two-step spincoating method. [224] I spincoated 50μL of 1M PbI_2 in DMF at 3000 rpm for 5s then immediately at 4500 rpm for 5s. Afterwards, I spincoated 200μL of 0.25M MAI in IPA on top of the PbI_2 film at 4000 rpm for 20s. I then annealed the resulting thin films in a DMF atmosphere at 100°C for an hour. To generate a DMF atmosphere, I covered the thin films with a petri dish while I dropped droplets of DMF around the edges of the petri dish for the vapor to enter the petri dish and surround the thin films.

To grow large $MAPbI_3$ crystals, I first prepared a ∼1.3M $MAPbI_3$ solution by dissolving 2.35g of PbI_2 and 0.8g of MAI in 3.85ml of gamma-butyrolactone. The solution is heated at 90°C and stirred with a magnetic stir bar at 300 rpm for approximately 4 hours. Using a syringe filter with 0.2μm pore size, I filtered out any undissolved residue and transferred the solution to a small beaker. The 1.3M solution is then heated to 130°C for about 2 hours, after which the crystals were separated from the solution. This method, known as inverse temperature crystallization, was first reported in reference [233] and has been adopted from reference [230].

Preliminary FSRS Data

As $MAPbI_3$ perovskites absorb the entire visible range of wavelength and up to ~850 nm, I was unable to obtain spontaneous Raman spectra of my samples as the wavelengths of available cw lasers were 532nm, 633nm and 785nm. Previous Raman spectrum published on $MAPbI_3$ utilized lasers in the infrared region (>1000nm). However, from the strong photoluminescence that saturates our CCD detector (even at 0.001s acquisition) on the continuous wave Raman table setup, it is likely that the synthesis was successful because neither MAI nor PbI_2 has such strong photoluminescence properties. Furthermore, the grey appearances and UV-vis spectra matched what had been published in literature.

When trying to run FSRS experiments on different $MAPbI_3$ samples, I ran into roadblocks. In summary, none of the samples showed stimulated ground state Raman features and only crystals are immune to photodamage under high magnification objectives (40× and 60×).

An example of a ground state stimulated Raman spectrum of a $MAPbI_3$ crystal is shown in Figure 6.1a. While it shows some peak-like features, none of their frequencies match any known ground state Raman features of $MAPbI_3$ as reported in literature. [230] One possibility is that the crystal is absorbing the Raman pump at 800-807nm, and the transient absorption is outcompeting the stimulated Raman process. Usually, transient absorption is not an issue as many photovoltaic materials, like acenes, do not absorb above 800nm at all. Another explanation is that the Raman cross sections of vibrations within the methylammonium ions are very low and any Raman signals are too weak to be picked up.

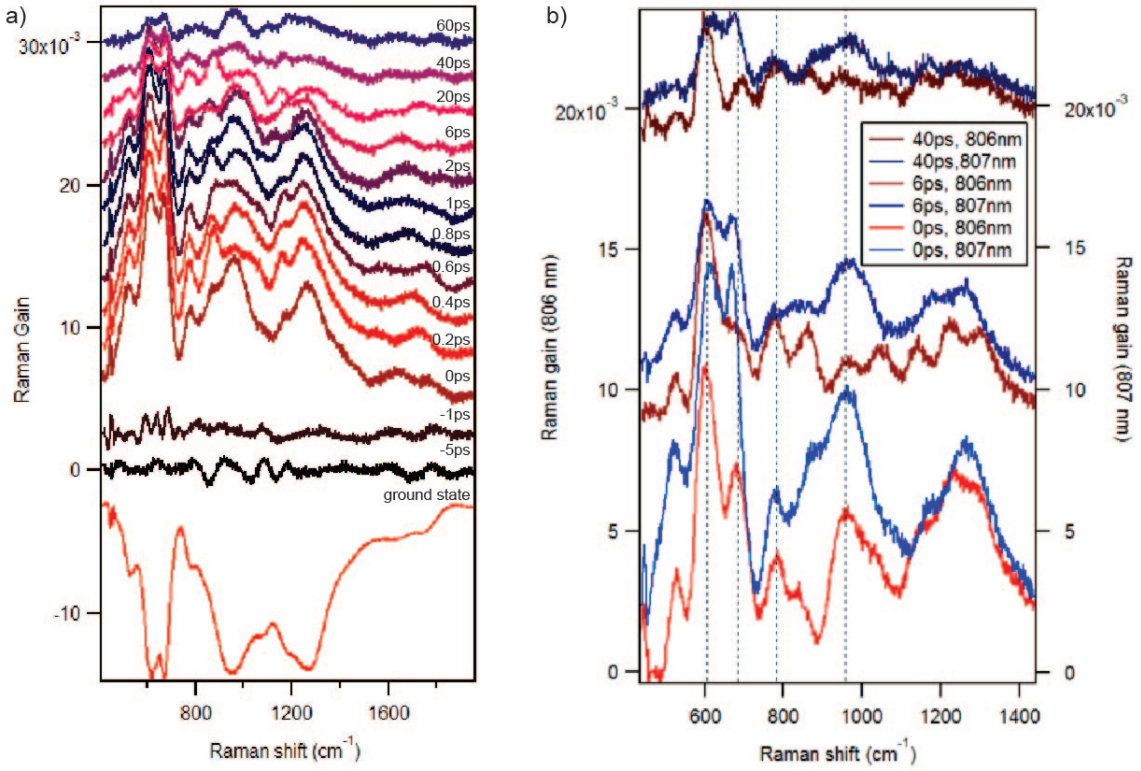

Figure 6.1: (a) FSR spectra of perovskite crystal (Raman pump = 807nm) at 530nm photoexcitation. The spectra were vertically offset for visual clarity. (b) Comparison of FSR spectra of perovskite crystal obtained from 806nm and 807nm Raman pump wavelength at 3 different time delays. Following the dashed lines, positive peaks at 602, 781 and 957 cm^{-1} are definitely not Raman features because they showed no changes in frequency at different Raman pump wavelengths. 680 cm^{-1} feature shifted by $\sim$10 cm^{-1} as expected, but also shows up in transient absorption spectra (not shown).

Since the absence of ground state stimulated Raman features does not signify the absence of Raman features in the excited state, I proceeded to run FSRS experiments at 530nm photoexcitation. For both thin films and crystalline samples, I observed qualitatively similar results as shown in Figure 6.1a. I observe narrow transient features that peak soon after photoexcitation and they start decaying within the first 50ps. As similar features also show up in the transient absorption spectra, there were unlikely to be Raman in nature. To verify that, I ran a dual Raman pump experiment on a

perovskite crystal using the method as described in Section 2.5. The Raman pump wavelengths used were 806nm and 807nm. If the features are Raman in nature, the peak frequencies would shift $\sim$11 cm^{-1} as observed in cyclohexane Raman peaks. If not, the frequencies would remain the same when plotted against the same calibrated x-axis.

Figure 6.1b shows the comparison of the excited state spectra of $MAPbI_3$ at 3 different time delays. Using the dashed lines as visual guides, it is clear that the 602, 781 and 957 cm^{-1} peaks are not Raman in nature and are likely transient absorption features. In contrast, 680 cm^{-1} feature shifted by $\sim$10 cm^{-1} and has the potential to be a Raman feature. However, this feature shows up with the same frequency shift in the transient absorption spectra despite the Raman pump wavelength having no impact on the transient absorption spectra. Qualitatively, the same 680 cm^{-1} feature also shifted by the expected amount when the dual Raman pump experiment was repeated for the same crystal at a different location with Raman pump wavelengths of 805 nm and 806 nm. This would mean that the 680 cm^{-1} peak is either vibronic in nature or an unexplained experimental artifact. Before $MAPbI_3$ proceeds to SO-FSRS, I need to be sure that I can observe Raman or vibronic features in the FSR spectra. More experiments or calculations need to be run to verify if the 680 cm^{-1} is an excited state vibronic feature or not.

Next Steps

A quick web-of-science search with the term 'perovskite' yields 91725 results. When the search term is specified to 'perovskite' and 'Raman', the results get lowered to 3750. If the search term is further narrowed to 'perovskite' and 'stimulated Raman', there are only 21 results. Looking at these 21 results, only 2 showed stimulated Raman spectra of perovskites. Ben-Uliel et al. managed to produce impulsive stimulated Raman spectra

of single $MAPbI_3$ crystal using continuous wave lasers.[a] [232] However, they did not provide any information on how they overcame the photoluminescence from $MAPbI_3$. Furthermore, the laser powers they were using were on the orders of mWs. If a similar power is achieved using our pulsed laser at 1 kHz rep rate, the peak power would be too high and even a crystal would be obliterated.

That brings us to the next example, where Kaminskii et al. managed to observe stimulated Raman signal from $Ba(Sn,Zr,Mg,Ta)O_3$ ceramics with cubic perovskite structure using picosecond Raman pulses. [234] Since this work's publication in 2007, there has yet to be any other stimulated Raman studies on perovskites using ultrafast lasers. It is unclear if this is due to a lack of interest from research groups familiar with SRS or that perovskites with similar cubic symmetry tend to anecdotally not produce stimulated Raman signals. Perhaps, if the perovskite projects is to be revisited with SO-FSRS, a $Ba(X)O_3$ perovskite would be a better system to target due to the presence of one precedent. However, this would mean that most of the Raman features expected will be under 1000 cm^{-1} and cyclohexane may not be the best standard to use for x-axis calibration.

6.3 Incorporating Compressive Sensing into SO-FSRS

Compressive sensing, or compressed sensing, is a sampling paradigm that allows one to reconstruct N pixels by only sampling M pixels randomly, where $M \ll N$. [235] For compressed sensing to work, it relies on two main assumptions - that the signals of interest are sparse and that M is a random sample of true space N.

In recent years, compressive sensing has been applied to a variety of spectroscopic techniques, such as magnetic resonance imaging [236], 2DIR [237] and transient absorption spectroscopy [238]. Compressive sensing can be applied to SO-FSRS in two manners - by taking less spatial positions and by measuring spectra at fewer time delays

[a] I only managed to access this paper through SciHub as it is not available through the University of Minnesota's library.

to reconstruct the ultrafast dynamics.

To apply compressive sensing to the ultrafast aspect of SO-FSRS, one can take inspirations from work by Adhikari et al. [238], who reconstructed time dynamics of transient absorption spectra using 16% of time points than they usually did, or from work by Dunbar et al. who managed to acquire over 200 spectra in less than 9 minutes. [237] To apply compressive sensing to the spatial aspect of SO-FSRS, one can refer to works done in ground state Raman imaging [239] and transient absorption microscopy. [240] In both cases, the research groups were able to reconstruct images with less than 10% of pixels.

If compressive sensing can be incorporated successfully with SO-FSRS, it would reduce data acquisition times significantly and reduce risk of photodamage to samples from long exposure to ultrafast high powered laser pulses.

Chapter 7

Conclusion

In conclusion, vibrational techniques are incredibly useful in helping us gain structural insights on how to improve chromophore designs to improve charge transport properties. With the successful development of SO-FSRS as documented in chapter 4, I have expanded the toolbox available to study the mechanism of charge generation and charge transport in photovoltaic systems.

When looking at the SO-FSR spectra of TIPS-pn, my analysis of the ground state depletion dynamics at various photoexcitation positions verified that the fast exciton transport axis in TIPS-pn is the same as the fast free charge carrier transport axis. However, the observed exciton charge mobility anisotropy was only $\sim 3\times$ as opposed to $\sim 10\times$ for free charge carriers, implying that while $\pi - \pi$ interactions facilitate charge transport, the effect is weaker for excitons.

After the TIPS-pn work has been published, I continued to improve SO-FSRS. With the addition of a second DAQ card, the galvomirrors now have a coarse and fine adjust for alignment and raster scan measurements respectively. This made spatial resolution of 50nm possible as long as the diameters of the Raman probe, Raman pump and photoexcitation pulses can be focused down to near their diffraction limit. In chapter 6, I outlined suitable systems for SO-FSRS to investigate. With the new structural

knowledge gained from studying exciton transport with SO-FSRS, we can gain insights on how to synthetically modify existing systems in order to optimize the efficiency of exciton transport.

References

[1] M. Smith and J. Michl, "Recent Advances in Singlet Fission," *Annual review of physical chemistry*, vol. 64, pp. 361–386, 2013.

[2] P. Hamm, "Principles of Nonlinear Optical Spectroscopy: A Practical Approach or: Mukamel for Dummies," 2005.

[3] D. McCamant, P. Kukura, S. Yoon, and R. Mathies, "Femtosecond Broadband Stimulated Raman Spectroscopy: Apparatus and Methods," *Review of scientific instruments*, vol. 75, no. 11, pp. 4971–4980, 2004.

[4] R. Frontiera and R. Mathies, "Femtosecond Stimulated Raman Spectroscopy," *Laser & Photonics Reviews*, vol. 5, no. 1, pp. 102–113, 2011.

[5] W. R. Silva, E. L. Keller, and R. R. Frontiera, "Determination of Resonance Raman Cross-Sections for Use in Biological SERS Sensing with Femtosecond Stimulated Raman Spectroscopy," *Analytical chemistry*, vol. 86, no. 15, pp. 7782–7787, 2014.

[6] W. Silva and R. Frontiera, "Excited State Structural Evolution during Charge-Transfer Reactions in Betaine-30," *Physical Chemistry Chemical Physics*, 2016.

[7] C. Grieco, E. R. Kennehan, A. Rimshaw, M. M. Payne, J. E. Anthony, and J. B. Asbury, "Harnessing Molecular Vibrations to Probe Triplet Dynamics During

Singlet Fission," *The journal of physical chemistry letters*, vol. 8, no. 23, pp. 5700–5706, 2017.

[8] A. Musser, M. Liebel, C. Schnedermann, T. Wende, T. Kehoe, A. Rao, and P. Kukura, "Evidence for Conical Intersection Dynamics Mediating Ultrafast Singlet Exciton Fission," *Nature Physics*, vol. 11, no. 4, pp. 352–357, 2015.

[9] C. Schnedermann, A. M. Alvertis, T. Wende, S. Lukman, J. Feng, F. A. Schröder, D. H. Turban, J. Wu, N. D. Hine, N. C. Greenham, *et al.*, "A Molecular Movie of Ultrafast Singlet Fission," *Nature communications*, vol. 10, no. 1, pp. 1–11, 2019.

[10] K. Bera, C. J. Douglas, and R. R. Frontiera, "Femtosecond Raman Microscopy Reveals Structural Dynamics Leading to Triplet Separation in Rubrene Singlet Fission," *The journal of physical chemistry letters*, vol. 8, no. 23, pp. 5929–5934, 2017.

[11] K. Bera, C. J. Douglas, and R. R. Frontiera, "Femtosecond Stimulated Raman Spectroscopy Guided Screening Leads to Efficient Singlet Fission in Rubrene Derivatives," *Chemical Science*, submitted.

[12] S. Y. Kwang and R. R. Frontiera, "Spatially Offset Femtosecond Stimulated Raman Spectroscopy: Observing Exciton Transport through a Vibrational Lens," *The Journal of Physical Chemistry Letters*, vol. 11, no. 11, pp. 4337–4344, 2020.

[13] Lawrence Livermore National Laboratory, "Estimated U.S. Energy Consumption in 2020: 92.9 Quads," 2020.

[14] W. Shockley and H. Queisser, "Detailed Balance Limit of Efficiency of *p-n* Junction Solar Cells," *Journal of Applied Physics*, vol. 32, no. 3, 1961.

[15] D. Congreve, J. Lee, N. Thompson, E. Hontz, S. Yost, P. D. Reusswig, M. Bahlke, S. Reineke, T. Van Voorhis, and M. Baldo, "External Quantum Efficiency above

100% in a Singlet-Exciton-Fission–Based Organic Photovoltaic Cell," *Science*, vol. 340, no. 6130, pp. 334–337, 2013.

[16] National Renewable Energy Laboratory, "Best Research-Cell Efficiency Chart," 2021.

[17] Z. Birech, M. Schwoerer, T. Schmeiler, J. Pflaum, and H. Schwoerer, "Ultrafast Dynamics of Excitons in Tetracene Single Crystals," *The Journal of chemical physics*, vol. 140, no. 11, p. 114501, 2014.

[18] A. Teke, Ü. Özgür, S. Doğan, X. Gu, H. Morkoç, B. Nemeth, J. Nause, and H. O. Everitt, "Excitonic Fine Structure and Recombination Dynamics in Single-Crystalline ZnO," *Physical Review B*, vol. 70, no. 19, p. 195207, 2004.

[19] O. V. Mikhnenko, P. W. Blom, and T. Nguyen, "Exciton Diffusion in Organic Semiconductors," *Energy & Environmental Science*, vol. 8, no. 7, pp. 1867–1888, 2015.

[20] C. Bardeen, "The Structure and Dynamics of Molecular Excitons," *Annual review of physical chemistry*, vol. 65, pp. 127–148, 2014.

[21] Y. Takeuti, "On The Exciton Problem in Insulating Crystals," *Progress of Theoretical Physics*, vol. 18, no. 4, pp. 421–436, 1957.

[22] H. Pohl, "Theories of Electronic Behavior in Macromolecular Solids," in *Journal of Polymer Science Part C: Polymer Symposia*, vol. 17, pp. 13–40, Wiley Online Library, 1967.

[23] P. Petelenz, "Mixing of Frenkel Excitons and Ionic Excited States of a Linear Molecular Crystal with Two Molecules in the Unit Cell I. General Model," *physica status solidi (b)*, vol. 78, no. 2, pp. 489–500, 1976.

[24] B. Petelenz, P. Petelenz, H. Shurvell, and V. Smith, "Reconsideration of the Electroabsorption Spectra of the Tetracene and Pentacene Crystals," *Chemical physics*, vol. 119, no. 1, pp. 25–39, 1988.

[25] R. Schuster, M. Knupfer, and H. Berger, "Exciton Band Structure of Pentacene Molecular Solids: Breakdown of the Frenkel Exciton Model," *Physical review letters*, vol. 98, no. 3, p. 037402, 2007.

[26] H. Yamagata, J. Norton, E. Hontz, Y. Olivier, D. Beljonne, J.-L. Brédas, R. Silbey, and F. Spano, "The Nature of Singlet Excitons in Oligoacene Molecular Crystals," *The Journal of chemical physics*, vol. 134, no. 20, p. 204703, 2011.

[27] S. Yost, E. Hontz, S. Yeganeh, and T. Van Voorhis, "Triplet vs Singlet Energy Transfer in Organic Semiconductors: the Tortoise and the Hare," *The Journal of Physical Chemistry C*, vol. 116, no. 33, pp. 17369–17377, 2012.

[28] P. Atkins and J. de Paula, "Molecular Spectroscopy 2: Electronic Transitions," in *Atkin's Physical Chemistry 10th ed.*, pp. 484–485, Oxford University Press, 2014.

[29] A. Lewis, A. Ruseckas, O. Gaudin, G. Webster, P. Burn, and I. Samuel, "Singlet Exciton Diffusion in MEH-PPV Films Studied by Exciton–Exciton Annihilation," *Organic Electronics*, vol. 7, no. 6, pp. 452–456, 2006.

[30] S. Cook, A. Furube, R. Katoh, and L. Han, "Estimate of Singlet Diffusion Lengths in PCBM Films by Time-Resolved Emission Studies," *Chemical Physics Letters*, vol. 478, no. 1, pp. 33–36, 2009.

[31] R. Lunt, N. Giebink, A. Belak, J. Benziger, and S. Forrest, "Exciton Diffusion Lengths of Organic Semiconductor Thin Films Measured by Spectrally Resolved Photoluminescence Quenching," *Journal of applied physics*, vol. 105, no. 5, p. 053711, 2009.

[32] G. Vaubel and H. Baessler, "Diffusion of Singlet Excitons in Tetracene Crystals," *Molecular crystals and liquid crystals*, vol. 12, no. 1, pp. 47–56, 1970.

[33] S. Cook, L. Han, A. Furube, and R. Katoh, "Singlet Annihilation in Films of Regioregular Poly(3-hexylthiophene): Estimates for Singlet Diffusion Lengths and the Correlation between Singlet Annihilation Rates and Spectral Relaxation," *The Journal of Physical Chemistry C*, vol. 114, no. 24, pp. 10962–10968, 2010.

[34] S. Haan and R. Zwanzig, "Förster Migration of Electronic Excitation between Randomly Distributed Molecules," *The Journal of Chemical Physics*, vol. 68, no. 4, pp. 1879–1883, 1978.

[35] C. Gochanour, A. H.C., and M. Fayer, "Electronic Excited State Transport in Solution," *The Journal of Chemical Physics*, vol. 70, no. 9, pp. 4254–4271, 1979.

[36] T. Gadella, "FRET Basics," in *FRET and FLIM techniques*, vol. 33, p. 13, Elsevier, 2011.

[37] Z.-Q. You and C.-P. Hsu, "The Fragment Spin Difference Scheme for Triplet-Triplet Energy Transfer Coupling," *The Journal of chemical physics*, vol. 133, no. 7, p. 074105, 2010.

[38] S. Scully and M. McGehee, "Effects of Optical Interference and Energy Transfer on Exciton Diffusion Length Measurements in Organic Semiconductors," *Journal of applied physics*, vol. 100, no. 3, p. 034907, 2006.

[39] J. Wünsche, S. Reineke, B. Lüssem, and K. Leo, "Measurement of Triplet Exciton Diffusion in Organic Light-Emitting Diodes," *Physical Review B*, vol. 81, no. 24, p. 245201, 2010.

[40] R. Lunt, J. Benziger, and S. Forrest, "Relationship Between Crystalline Order and Exciton Diffusion Length in Molecular Organic Semiconductors," *Advanced Materials*, vol. 22, no. 11, pp. 1233–1236, 2010.

[41] P. Avakian and R. Merrifield, "Experimental Determination of the Diffusion Length of Triplet Excitons in Anthracene Crystals," *Physical Review Letters*, vol. 13, no. 18, p. 541, 1964.

[42] H. Najafov, B. Lee, Q. Zhou, L. Feldman, and V. Podzorov, "Observation of Long-Range Exciton Diffusion in Highly Ordered Organic Semiconductors," *Nature materials*, vol. 9, no. 11, pp. 938–943, 2010.

[43] W.-L. Chan, M. Ligges, A. Jailaubekov, K. L., L. Miaja-Avila, and X.-Y. Zhu, "Observing the Multiexciton State in Singlet Fission and Ensuing Ultrafast Multielectron Transfer," *Science*, vol. 334, no. 6062, pp. 1541–1545, 2011.

[44] J. Burdett and C. Bardeen, "Quantum Beats in Crystalline Tetracene Delayed Fluorescence due to Triplet Pair Coherences Produced by Direct Singlet Fission," *Journal of the American Chemical Society*, vol. 134, no. 20, pp. 8597–8607, 2012.

[45] K. Miyata, F. Conrad-Burton, F. Geyer, and X.-Y. Zhu, "Triplet Pair States in Singlet Fission," *Chemical reviews*, vol. 119, no. 6, pp. 4261–4292, 2019.

[46] N. Korovina, C. Chang, and J. Johnson, "Spatial Separation of Triplet Excitons Drives Endothermic Singlet Fission," *Nature chemistry*, vol. 12, no. 4, pp. 391–398, 2020.

[47] D. Griffiths, "The Zeeman Effect," in *Introduction to Quantum Mechanics (2nd edition)*, pp. 155–159,244–245, Pearson Prentice Hall, 2004.

[48] M. Born and E. Wolf, "Polarization Properties of Quasi-Monochromatic Light," in *Principles of Optics 6th ed.*, pp. 546–547, Pergamon Press Ltd., 1980.

[49] N. Monahan and X.-Y. Zhu, "Charge Transfer-Mediated Singlet Fission," *Annual review of physical chemistry*, vol. 66, pp. 601–618, 2015.

[50] P. Petelenz, M. Slawik, K. Yokoi, and M. Zgierski, "Theoretical Calculation of the Electroabsorption Spectra of Polyacene Crystals," *The Journal of chemical physics*, vol. 105, no. 11, pp. 4427–4440, 1996.

[51] A. Davydov, "The Theory of Molecular Excitons," *Soviet Physics Uspekhi*, vol. 82, pp. 393–448, 1964.

[52] D. Beljonne, H. Yamagata, J.-L. Brédas, F. Spano, and Y. Olivier, "Charge-Transfer Excitations Steer the Davydov Splitting and Mediate Singlet Exciton Fission in Pentacene," *Physical review letters*, vol. 110, no. 22, p. 226402, 2013.

[53] W.-L. Chan, T. C. Berkelbach, M. Provorse, N. Monahan, J. Tritsch, M. Hybertsen, D. Reichman, J. Gao, and X.-Y. Zhu, "The Quantum Coherent Mechanism for Singlet Fission: Experiment and Theory," *Accounts of chemical research*, vol. 46, no. 6, pp. 1321–1329, 2013.

[54] P. Zimmerman, C. Musgrave, and M. Head-Gordon, "A Correlated Electron View of Singlet Fission," *Accounts of chemical research*, vol. 46, no. 6, pp. 1339–1347, 2013.

[55] P. Zimmerman, Z. Zhang, and C. Musgrave, "Singlet Fission in Pentacene through Multi-Exciton Quantum States," *Nature chemistry*, vol. 2, no. 8, pp. 648–652, 2010.

[56] N. Renaud, P. Sherratt, and M. Ratner, "Mapping the Relation between Stacking Geometries and Singlet Fission Yield in a Class of Organic Crystals," *The journal of physical chemistry letters*, vol. 4, no. 7, pp. 1065–1069, 2013.

[57] A. Kühl and W. Domcke, "Multilevel Redfield Description of the Dissipative Dynamics at Conical Intersections," *The Journal of chemical physics*, vol. 116, no. 1, pp. 263–274, 2002.

[58] V. Coropceanu, J. Cornil, D. da Silva Filho, Y. Olivier, R. Silbey, and J.-L. Brédas, "Charge Transport in Organic Semiconductors," *Chemical reviews*, vol. 107, no. 4, pp. 926–952, 2007.

[59] M. Samiullah, D. Moghe, U. Scherf, and S. Guha, "Diffusion Length of Triplet Excitons in Organic Semiconductors," *Physical Review B*, vol. 82, no. 20, p. 205211, 2010.

[60] G. Akselrod, P. Deotare, N. Thompson, J. Lee, W. Tisdale, M. Baldo, V. Menon, and V. Bulović, "Visualization of Exciton Transport in Ordered and Disordered Molecular Solids," *Nature communications*, vol. 5, 2014.

[61] Y. Wan, Z. Guo, T. Zhu, S. Yan, J. Johnson, and L. Huang, "Cooperative Singlet and Triplet Exciton Transport in Tetracene Crystals Visualized by Ultrafast Microscopy," *Nature chemistry*, vol. 7, no. 10, pp. 785–792, 2015.

[62] C. Raman and K. Krishnan, "A New Type of Secondary Radiation," *Nature*, vol. 121, pp. 501–502, 1928.

[63] C. Raman, "A Change of Wave-Length in Light Scattering," *Nature*, vol. 121, p. 619, 1928.

[64] J. Van Vleck, "On the Vibrational Selection Principles in the Raman Effect," *Proceedings of the National Academy of Sciences*, vol. 15, no. 9, pp. 754–764, 1929.

[65] J. McLennan, "On the Raman Effect with Liquid Oxygen, Nitrogen and Hydrogen," *Transactions of the Faraday Society*, vol. 25, pp. 797–800, 1929.

[66] C. Raman, "Part II.—The Raman Effect. Investigation of Molecular Structure by Light Scattering," *Transactions of the Faraday Society*, vol. 25, pp. 781–792, 1929.

[67] D. Andrews, "The Relation Between the Raman Spectra and the Structure of Organic Molecules," *Physical Review*, vol. 36, no. 3, p. 544, 1930.

[68] D. Skoog and D. West, "Methods Based Upon Light Scattering," in *Principles of Instrumental Analysis*, pp. 247–253, Holt, Rinehard and Winston, Inc., 1971.

[69] J. White, "Stimulated Raman Scattering," in *Tunable lasers*, pp. 115–207, Springer, 1987.

[70] P. Kukura, D. McCamant, and R. Mathies, "Femtosecond Stimulated Raman Spectroscopy," *Annu. Rev. Phys. Chem.*, vol. 58, pp. 461–488, 2007.

[71] K. Bera, S. Y. Kwang, A. A. Cassabaum, C. C. Rich, and R. R. Frontiera, "Facile Background Discrimination in Femtosecond Stimulated Raman Spectroscopy Using a Dual-Frequency Raman Pump Technique," *The Journal of Physical Chemistry A*, vol. 123, no. 37, pp. 7932–7939, 2019.

[72] S. T. McCain, R. M. Willett, and D. J. Brady, "Multi-Excitation Raman Spectroscopy Technique for Fluorescence Rejection," *Optics Express*, vol. 16, no. 15, pp. 10975–10991, 2008.

[73] P. Mosier-Boss, S. Lieberman, and R. Newbery, "Fluorescence Rejection in Raman Spectroscopy by Shifted-Spectra, Edge Detection, and FFT Filtering Techniques," *Applied Spectroscopy*, vol. 49, no. 5, pp. 630–638, 1995.

[74] J. Zhao, M. M. Carrabba, and F. S. Allen, "Automated Fluorescence Rejection Using Shifted Excitation Raman Difference Spectroscopy," *Applied Spectroscopy*, vol. 56, no. 7, pp. 834–845, 2002.

[75] A. P. Shreve, N. J. Cherepy, and R. A. Mathies, "Effective Rejection of Fluorescence Interference in Raman Spectroscopy Using a Shifted Excitation Difference Technique," *Applied spectroscopy*, vol. 46, no. 4, pp. 707–711, 1992.

[76] K. Sowoidnich and H. Kronfeldt, "Fluorescence Rejection by Shifted Excitation Raman Difference Spectroscopy at Multiple Wavelengths for the Investigation of Biological Samples," *International Scholarly Research Notices*, vol. 2012, 2012.

[77] M. T. Gebrekidan, C. Knipfer, F. Stelzle, J. Popp, S. Will, and A. Braeuer, "A Shifted-Excitation Raman Difference Spectroscopy (SERDS) Evaluation Strategy for the Efficient Isolation of Raman Spectra from Extreme Fluorescence Interference," *Journal of Raman spectroscopy*, vol. 47, no. 2, pp. 198–209, 2016.

[78] J. B. Cooper, S. Marshall, R. Jones, M. Abdelkader, and K. L. Wise, "Spatially Compressed Dual-Wavelength Excitation Raman Spectrometer," *Applied optics*, vol. 53, no. 15, pp. 3333–3340, 2014.

[79] M. Maiwald, B. Sumpf, and G. Tränkle, "Rapid and Adjustable Shifted Excitation Raman Difference Spectroscopy Using a Dual-Wavelength Diode Laser at 785 nm," *Journal of Raman Spectroscopy*, vol. 49, no. 11, pp. 1765–1775, 2018.

[80] J. Zhao, H. Lui, D. I. McLean, and H. Zeng, "Automated Autofluorescence Background Subtraction Algorithm for Biomedical Raman Spectroscopy," *Applied spectroscopy*, vol. 61, no. 11, pp. 1225–1232, 2007.

[81] M. Maiwald, A. Müller, B. Sumpf, G. Erbert, and G. Tränkle, "Capability of Shifted Excitation Raman Difference Spectroscopy Under Ambient Daylight," *Applied optics*, vol. 54, no. 17, pp. 5520–5524, 2015.

[82] E. M. Grumstrup, Z. Chen, R. P. Vary, A. M. Moran, K. S. Schanze, and J. M. Papanikolas, "Frequency Modulated Femtosecond Stimulated Raman Spectroscopy of Ultrafast Energy Transfer in a Donor–Acceptor Copolymer," *The Journal of Physical Chemistry B*, vol. 117, no. 27, pp. 8245–8255, 2013.

[83] P. M. Kearns, Z. Sohrabpour, and A. M. Massari, "Frequency Comb SFG: a New Approach to Multiplex Detection," *Optics express*, vol. 24, no. 17, pp. 19863–19870, 2016.

[84] P. Matousek, M. Towrie, and A. Parker, "Fluorescence Background Suppression in Raman Spectroscopy Using Combined Kerr Gated and Shifted Excitation Raman

Difference Techniques," *Journal of Raman Spectroscopy*, vol. 33, no. 4, pp. 238–242, 2002.

[85] H. Ahmad, "Gold Substrates for SERS and SERS/SERDS Measurements in Seawater and Raman Measurements through Long Optical Fibers," 2014.

[86] H. Schmidt, D. P. Kaiser, and M. Maiwald, "Method for Generating and for Detecting a Raman Spectrum," 2012. US Patent 8,310,672.

[87] S. Guo, O. Chernavskaia, J. Popp, and T. Bocklitz, "Spectral Reconstruction for Shifted-Excitation Raman Difference Spectroscopy (SERDS)," *Talanta*, vol. 186, pp. 372–380, 2018.

[88] K. Bera, S. Y. Kwang, and R. R. Frontiera, "Advances in Singlet Fission Chromophore Design Enabled by Vibrational Spectroscopies," *The Journal of Physical Chemistry C*, vol. 124, no. 46, pp. 25163–25174, 2020.

[89] R. Kepler, J. Caris, P. Avakian, and E. Abramson, "Triplet Excitons and Delayed Fluorescence in Anthracene Crystals," *Physical Review Letters*, vol. 10, no. 9, p. 400, 1963.

[90] S. Singh, W. Jones, W. Siebrand, B. Stoicheff, and W. Schneider, "Laser Generation of Excitons and Fluorescence in Anthracene Crystals," *The Journal of Chemical Physics*, vol. 42, no. 1, pp. 330–342, 1965.

[91] M. Hanna and A. Nozik, "Solar Conversion Efficiency of Photovoltaic and Photoelectrolysis Cells with Carrier Multiplication Absorbers," *Journal of Applied Physics*, vol. 100, no. 7, 2006.

[92] I. Paci, J. Johnson, X. Chen, G. Rana, D. Popović, D. David, A. Nozik, M. Ratner, and J. Michl, "Singlet Fission for Dye-Sensitized Solar Cells: Can a Suitable Sensitizer be Found?," *Journal of the American Chemical Society*, vol. 128, no. 51, pp. 16546–16553, 2006.

[93] A. Müller, Y. Avlasevich, K. Müllen, and C. Bardeen, "Evidence for Exciton Fission and Fusion in a Covalently Linked Tetracene Dimer," *Chemical physics letters*, vol. 421, no. 4-6, pp. 518–522, 2006.

[94] M. Einzinger, T. Wu, J. Kompalla, H. Smith, C. Perkinson, L. Nienhaus, S. Wieghold, D. Congreve, A. Kahn, M. Bawendi, *et al.*, "Sensitization of Silicon by Singlet Exciton Fission in Tetracene," *Nature*, vol. 571, no. 7763, pp. 90–94, 2019.

[95] A. Musser and J. Clark, "Triplet-Pair States in Organic Semiconductors," *Annual review of physical chemistry*, vol. 70, pp. 323–351, 2019.

[96] M. K. Gish, N. A. Pace, G. Rumbles, and J. C. Johnson, "Emerging Design Principles for Enhanced Solar Energy Utilization with Singlet Fission," *The Journal of Physical Chemistry C*, vol. 123, no. 7, pp. 3923–3934, 2019.

[97] S. Ito, T. Nagami, and M. Nakano, "Molecular Design for Efficient Singlet Fission," *Journal of Photochemistry and Photobiology C: Photochemistry Reviews*, vol. 34, pp. 85–120, 2018.

[98] A. Rao and R. H. Friend, "Harnessing Singlet Exciton Fission to Break the Shockley–Queisser Limit," *Nature reviews materials*, vol. 2, no. 11, pp. 1–12, 2017.

[99] J. Xia, S. N. Sanders, W. Cheng, J. Z. Low, J. Liu, L. M. Campos, and T. Sun, "Singlet Fission: Progress and Prospects in Solar Cells," *Advanced Materials*, vol. 29, no. 20, p. 1601652, 2017.

[100] M. Smith and J. Michl, "Singlet Fission," *Chemical reviews*, vol. 110, no. 11, pp. 6891–6936, 2010.

[101] E. G. Fuemmeler, S. N. Sanders, A. B. Pun, E. Kumarasamy, T. Zeng, K. Miyata, M. L. Steigerwald, X.-Y. Zhu, M. Y. Sfeir, L. M. Campos, *et al.*, "A Direct

Mechanism of Ultrafast Intramolecular Singlet Fission in Pentacene Dimers," *ACS central science*, vol. 2, no. 5, pp. 316–324, 2016.

[102] D. Guo, L. Ma, Z. Zhou, D. Lin, C. Wang, X. Zhao, F. Zhang, J. Zhang, and Z. Nie, "Charge Transfer Dynamics in a Singlet Fission Organic Molecule and Organometal Perovskite Bilayer Structure," *Journal of Materials Chemistry A*, vol. 8, no. 11, pp. 5572–5579, 2020.

[103] J. Guo, H. Ohkita, H. Benten, and S. Ito, "Near-IR Femtosecond Transient Absorption Spectroscopy of Ultrafast Polaron and Triplet Exciton Formation in Polythiophene Films with Different Regioregularities," *Journal of the American Chemical Society*, vol. 131, no. 46, pp. 16869–16880, 2009.

[104] M. T. Trinh, A. Pinkard, A. B. Pun, S. N. Sanders, E. Kumarasamy, M. Sfeir, L. M. Campos, X. Roy, and X.-Y. Zhu, "Distinct Properties of the Triplet Pair State from Singlet Fission," *Science advances*, vol. 3, no. 7, p. e1700241, 2017.

[105] I. Breen, R. Tempelaar, L. A. Bizimana, B. Kloss, D. R. Reichman, and D. B. Turner, "Triplet Separation Drives Singlet Fission after Femtosecond Correlated Triplet Pair Production in Rubrene," *Journal of the American Chemical Society*, vol. 139, no. 34, pp. 11745–11751, 2017.

[106] N. R. Monahan, D. Sun, H. Tamura, K. W. Williams, B. Xu, Y. Zhong, B. Kumar, C. Nuckolls, A. R. Harutyunyan, G. Chen, *et al.*, "Dynamics of the Triplet-Pair State Reveals the Likely Coexistence of Coherent and Incoherent Singlet Fission in Crystalline Hexacene," *Nature chemistry*, vol. 9, no. 4, pp. 341–346, 2017.

[107] B. S. Basel, J. Zirzlmeier, C. Hetzer, B. T. Phelan, M. D. Krzyaniak, S. R. Reddy, P. B. Coto, N. E. Horwitz, R. M. Young, F. J. White, *et al.*, "Unified Model for Singlet Fission within a Non-Conjugated Covalent Pentacene Dimer," *Nature communications*, vol. 8, no. 1, pp. 1–8, 2017.

[108] S. Matsuda, S. Oyama, and Y. Kobori, "Electron Spin Polarization Generated by Transport of Singlet and Quintet Multiexcitons to Spin-Correlated Triplet Pairs during Singlet Fissions," *Chemical Science*, vol. 11, no. 11, pp. 2934–2942, 2020.

[109] D. Casanova, "Theoretical Modeling of Singlet Fission," *Chemical reviews*, vol. 118, no. 15, pp. 7164–7207, 2018.

[110] A. Japahuge and T. Zeng, "Theoretical Studies of Singlet Fission: Searching for Materials and Exploring Mechanisms," *ChemPlusChem*, vol. 83, no. 4, pp. 146–182, 2018.

[111] A. F. Morrison and J. M. Herbert, "Evidence for Singlet Fission Driven by Vibronic Coherence in Crystalline Tetracene," *The journal of physical chemistry letters*, vol. 8, no. 7, pp. 1442–1448, 2017.

[112] K. Shizu, C. Adachi, and H. Kaji, "Effect of Vibronic Coupling on Correlated Triplet Pair Formation in the Singlet Fission Process of Linked Tetracene Dimers," *The Journal of Physical Chemistry A*, vol. 124, no. 18, pp. 3641–3651, 2020.

[113] G. Deng, Q. Wei, J. Han, Y. Qian, J. Luo, A. R. Harutyunyan, G. Chen, H. Bian, H. Chen, and Y. Rao, "Vibronic Fingerprint of Singlet Fission in Hexacene," *The Journal of Chemical Physics*, vol. 151, no. 5, p. 054703, 2019.

[114] M. Chen, Y. J. Bae, C. M. Mauck, A. Mandal, R. M. Young, and M. R. Wasielewski, "Singlet Fission in Covalent Terrylenediimide Dimers: Probing the Nature of the Multiexciton State using Femtosecond Mid-Infrared Spectroscopy," *Journal of the American Chemical Society*, vol. 140, no. 29, pp. 9184–9192, 2018.

[115] E. A. Margulies, N. Kerisit, P. Gawel, C. M. Mauck, L. Ma, C. E. Miller, R. M. Young, N. Trapp, Y. Wu, F. Diederich, *et al.*, "Substituent Effects on Singlet Exciton Fission in Polycrystalline Thin Films of Cyano-Substituted Diaryltetracenes," *The Journal of Physical Chemistry C*, vol. 121, no. 39, pp. 21262–21271, 2017.

[116] C. Grieco, E. R. Kennehan, H. Kim, R. D. Pensack, A. N. Brigeman, A. Rimshaw, M. M. Payne, J. E. Anthony, N. C. Giebink, G. D. Scholes, *et al.*, "Direct Observation of Correlated Triplet Pair Dynamics During Singlet Fission using Ultrafast Mid-IR Spectroscopy," *The Journal of Physical Chemistry C*, vol. 122, no. 4, pp. 2012–2022, 2018.

[117] C. Grieco, G. S. Doucette, K. T. Munson, J. R. Swartzfager, J. M. Munro, J. E. Anthony, I. Dabo, and J. B. Asbury, "Vibrational Probe of the Origin of Singlet Exciton Fission in TIPS-Pentacene Solutions," *The Journal of chemical physics*, vol. 151, no. 15, p. 154701, 2019.

[118] M. Angelella, C. Wang, and M. J. Tauber, "Resonance Raman Spectra of a Perylene Bis(dicarboximide) Chromophore in Ground and Lowest Triplet States," *The Journal of Physical Chemistry A*, vol. 117, no. 38, pp. 9196–9204, 2013.

[119] C. Wang, M. Angelella, S. J. Doyle, L. A. Lytwak, P. J. Rossky, B. J. Holliday, and M. J. Tauber, "Resonance Raman Spectroscopy of the T_1 Triplet Excited State of Oligothiophenes," *The journal of physical chemistry letters*, vol. 6, no. 18, pp. 3521–3527, 2015.

[120] M. J. Llansola-Portoles, K. Redeckas, S. Streckaité, C. Ilioaia, A. A. Pascal, A. Telfer, M. Vengris, L. Valkunas, and B. Robert, "Lycopene Crystalloids Exhibit Singlet Exciton Fission in Tomatoes," *Physical Chemistry Chemical Physics*, vol. 20, no. 13, pp. 8640–8646, 2018.

[121] C. Wang and M. J. Tauber, "High-Yield Singlet Fission in a Zeaxanthin Aggregate Observed by Picosecond Resonance Raman Spectroscopy," *Journal of the American Chemical Society*, vol. 132, no. 40, pp. 13988–13991, 2010.

[122] C. Wang, D. E. Schlamadinger, V. Desai, and M. J. Tauber, "Triplet Excitons of Carotenoids Formed by Singlet Fission in a Membrane," *ChemPhysChem*, vol. 12, no. 16, pp. 2891–2894, 2011.

[123] H. L. Stern, A. Cheminal, S. R. Yost, K. Broch, S. L. Bayliss, K. Chen, M. Tabachnyk, K. Thorley, N. Greenham, J. M. Hodgkiss, *et al.*, "Vibronically Coherent Ultrafast Triplet-Pair Formation and Subsequent Thermally Activated Dissociation Control Efficient Endothermic Singlet Fission," *Nature chemistry*, vol. 9, no. 12, p. 1205, 2017.

[124] A. A. Bakulin, S. E. Morgan, T. B. Kehoe, M. W. Wilson, A. W. Chin, D. Zigmantas, D. Egorova, and A. Rao, "Real-Time Observation of Multiexcitonic States in Ultrafast Singlet Fission using Coherent 2D Electronic Spectroscopy," *Nature chemistry*, vol. 8, no. 1, pp. 16–23, 2016.

[125] S. M. Hart, W. R. Silva, and R. R. Frontiera, "Femtosecond Stimulated Raman Evidence for Charge-Transfer Character in Pentacene Singlet Fission," *Chemical science*, vol. 9, no. 5, pp. 1242–1250, 2018.

[126] L. Ma, K. Zhang, C. Kloc, H. Sun, M. E. Michel-Beyerle, and G. G. Gurzadyan, "Singlet Fission in Rubrene Single Crystal: Direct Observation by Femtosecond Pump–Probe Spectroscopy," *Physical Chemistry Chemical Physics*, vol. 14, no. 23, pp. 8307–8312, 2012.

[127] R. Merrifield, "Magnetic Effects on Triplet Exciton Interactions," in *Organic Solid-State Chemistry–2*, pp. 481–498, Elsevier, 1971.

[128] M. J. Tayebjee, S. N. Sanders, E. Kumarasamy, L. M. Campos, M. Y. Sfeir, and D. R. McCamey, "Quintet Multiexciton Dynamics in Singlet Fission," *Nature Physics*, vol. 13, no. 2, pp. 182–188, 2017.

[129] J. Musfeldt, L. Vergara, T. Brinzari, C. Lee, L. Tung, J. Kang, Y. Wang, J. Schlueter, J. L. Manson, and M.-H. Whangbo, "Magnetoelastic Coupling through the Antiferromagnet-to-Ferromagnet Transition of Quasi-Two-Dimensional $[Cu(HF_2)(pyz)_2]BF_4$ using Infrared Spectroscopy," *Physical review letters*, vol. 103, no. 15, p. 157401, 2009.

[130] E. M. Grumstrup, J. C. Johnson, and N. H. Damrauer, "Enhanced Triplet Formation in Polycrystalline Tetracene Films by Femtosecond Optical-Pulse Shaping," *Physical review letters*, vol. 105, no. 25, p. 257403, 2010.

[131] M. A. Castellanos and P. Huo, "Enhancing Singlet Fission Dynamics by Suppressing Destructive Interference between Charge-Transfer Pathways," *The journal of physical chemistry letters*, vol. 8, no. 11, pp. 2480–2488, 2017.

[132] B. C. Paulus, S. L. Adelman, L. L. Jamula, and J. K. McCusker, "Leveraging Excited-State Coherence for Synthetic Control of Ultrafast Dynamics," *Nature*, vol. 582, no. 7811, pp. 214–218, 2020.

[133] A. I. McIntosh, B. Yang, S. M. Goldup, M. Watkinson, and R. S. Donnan, "Terahertz Spectroscopy: a Powerful New Tool for the Chemical Sciences?," *Chemical Society Reviews*, vol. 41, no. 6, pp. 2072–2082, 2012.

[134] O. Esenturk, P. A. Lane, J. S. Melinger, and E. J. Heilweil, "Ultrafast Terahertz Spectroscopy for Measuring Carrier Dynamics in Nanoscale Photovoltaic Materials," in *Ultrafast Phenomena in Semiconductors and Nanostructure Materials XIV*, vol. 7600, p. 76000I, International Society for Optics and Photonics, 2010.

[135] Y. Lan, X. Tao, X. Kong, Y. He, X. Zheng, M. Sutton, M. G. Kanatzidis, H. Guo, and D. G. Cooke, "Coherent Charge-Phonon Correlations and Exciton Dynamics in Orthorhombic $CH_3NH_3PbI_3$ Measured by Ultrafast Multi-THz Spectroscopy," *The Journal of chemical physics*, vol. 151, no. 21, p. 214201, 2019.

[136] T. Zhu and L. Huang, "Exciton Transport in Singlet Fission Materials: a New Hare and Tortoise Story," *The journal of physical chemistry letters*, vol. 9, no. 22, pp. 6502–6510, 2018.

[137] ThorLabs, https://www.thorlabs.com/drawings/a05faf8d259504b9-A5525E1C-E422-9F85-AAE652A78351DBDC/GVS012_M-Manual.pdf, *Single- and Dual-Axis Scanning Galvo Systems for Large Beam Diameter User Guide*, October 2020.

[138] M. A. Reed, "Molecular-Scale Electronics," *Proceedings of the IEEE*, vol. 87, no. 4, pp. 652–658, 1999.

[139] C. Joachim, J. K. Gimzewski, and A. Aviram, "Electronics Using Hybrid-Molecular and Mono-Molecular Devices," *Nature*, vol. 408, no. 6812, pp. 541–548, 2000.

[140] R. Stadler, "Molecular Electronics," in *Properties of Single Organic Molecules on Crystal Surfaces*, pp. 363–387, World Scientific, 2006.

[141] J. Bourgoin, D. Vuillaume, M. F. Goffman, and A. Filoramo, "Molecular Electronics," in *Nanoscience*, pp. 447–501, Springer, 2007.

[142] P. Tyagi, "Multilayer Edge Molecular Electronics Devices: a Review," *Journal of Materials Chemistry*, vol. 21, no. 13, pp. 4733–4742, 2011.

[143] C. A. Mack, "Fifty Years of Moore's Law," *IEEE Transactions on semiconductor manufacturing*, vol. 24, no. 2, pp. 202–207, 2011.

[144] J. R. Powell, "The Quantum Limit to Moore's Law," *Proceedings of the IEEE*, vol. 96, no. 8, pp. 1247–1248, 2008.

[145] M. Lundstrom, "Moore's Law Forever?," *Science*, vol. 299, no. 5604, pp. 210–211, 2003.

[146] R. Thakur, "50 Years of Moore's Law," *Solid State Technololgy*, vol. 58, no. 4, p. 41, 2015.

[147] P. Hersch and K. Zweibel, "Basic Photovoltaic Principles and Methods," tech. rep., Feb. 1982.

[148] J. Nelson, "Organic Photovoltaic Films," *Current Opinion in Solid State and Materials Science*, vol. 6, no. 1, pp. 87–95, 2002.

[149] K. M. Coakley and M. D. McGehee, "Conjugated Polymer Photovoltaic Cells," *Chemistry of materials*, vol. 16, no. 23, pp. 4533–4542, 2004.

[150] M. Grätzel, "Solar Energy Conversion by Dye-Sensitized Photovoltaic Cells," *Inorganic chemistry*, vol. 44, no. 20, pp. 6841–6851, 2005.

[151] H. A. Atwater and A. Polman, "Plasmonics for Improved Photovoltaic Devices," *Materials for sustainable energy: A collection of peer-reviewed research and review articles from nature publishing group*, pp. 1–11, 2011.

[152] B. Parida, S. Iniyan, and R. Goic, "A Review of Solar Photovoltaic Technologies," *Renewable and sustainable energy reviews*, vol. 15, no. 3, pp. 1625–1636, 2011.

[153] J. Franck and E. Teller, "Migration and Photochemical Action of Excitation Energy in Crystals," *The Journal of Chemical Physics*, vol. 6, no. 12, pp. 861–872, 1938.

[154] T. S. Rose, R. Righini, and M. Fayer, "Picosecond Transient Grating Measurements of Singlet Exciton Transport in Anthracene Single Crystals," *Chemical physics letters*, vol. 106, no. 1-2, pp. 13–19, 1984.

[155] C. Y. Wong, B. L. Cotts, H. Wu, and N. S. Ginsberg, "Exciton Dynamics Reveal Aggregates with Intermolecular Order at Hidden Interfaces in Solution-Cast Organic Semiconducting Films," *Nature communications*, vol. 6, no. 1, pp. 1–7, 2015.

[156] T. Yago, Y. Tamaki, A. Furube, and R. Katoh, "Self-Trapping Limited Exciton Diffusion in a Monomeric Perylene Crystal as Revealed by Femtosecond Transient

Absorption Microscopy," *Physical Chemistry Chemical Physics*, vol. 10, no. 30, pp. 4435–4441, 2008.

[157] G. Grancini, D. Polli, D. Fazzi, J. Cabanillas-Gonzalez, G. Cerullo, and G. Lanzani, "Transient Absorption Imaging of P3HT: PCBM Photovoltaic Blend: Evidence for Interfacial Charge Transfer State," *The Journal of Physical Chemistry Letters*, vol. 2, no. 9, pp. 1099–1105, 2011.

[158] Z. Guo, J. S. Manser, Y. Wan, P. V. Kamat, and L. Huang, "Spatial and Temporal Imaging of Long-Range Charge Transport in Perovskite Thin Films by Ultrafast Microscopy," *Nature communications*, vol. 6, no. 1, pp. 1–8, 2015.

[159] M. J. Simpson, B. Doughty, B. Yang, K. Xiao, and Y. Ma, "Imaging Electronic Trap States in Perovskite Thin Films with Combined Fluorescence and Femtosecond Transient Absorption Microscopy," *The journal of physical chemistry letters*, vol. 7, no. 9, pp. 1725–1731, 2016.

[160] N. S. Ginsberg and W. A. Tisdale, "Spatially Resolved Photogenerated Exciton and Charge Transport in Emerging Semiconductors," *Annual review of physical chemistry*, vol. 71, pp. 1–30, 2020.

[161] T. Zhu, J. M. Snaider, L. Yuan, and L. Huang, "Ultrafast Dynamic Microscopy of Carrier and Exciton Transport," *Annual review of physical chemistry*, vol. 70, pp. 219–244, 2019.

[162] E. S. Massaro, A. H. Hill, and E. M. Grumstrup, "Super-Resolution Structured Pump–Probe Microscopy," *ACS Photonics*, vol. 3, no. 4, pp. 501–506, 2016.

[163] M. M. Gabriel, J. R. Kirschbrown, J. D. Christesen, C. W. Pinion, D. F. Zigler, E. M. Grumstrup, B. P. Mehl, E. E. Cating, J. F. Cahoon, and J. M. Papanikolas, "Direct Imaging of Free Carrier and Trap Carrier Motion in Silicon Nanowires by

Spatially-Separated Femtosecond Pump–Probe Microscopy," *Nano letters*, vol. 13, no. 3, pp. 1336–1340, 2013.

[164] L. Tong, Y. Liu, B. D. Dolash, Y. Jung, M. N. Slipchenko, D. E. Bergstrom, and J. Cheng, "Label-Free Imaging of Semiconducting and Metallic Carbon Nanotubes in Cells and Mice using Transient Absorption Microscopy," *Nature nanotechnology*, vol. 7, no. 1, pp. 56–61, 2012.

[165] D. Davydova, A. de la Cadena, D. Akimov, and B. Dietzek, "Transient Absorption Microscopy: Advances in Chemical Imaging of Photoinduced Dynamics," *Laser & Photonics Reviews*, vol. 10, no. 1, pp. 62–81, 2016.

[166] L. Huang, G. V. Hartland, L. Chu, R. M. Feenstra, C. Lian, K. Tahy, and H. Xing, "Ultrafast Transient Absorption Microscopy Studies of Carrier Dynamics in Epitaxial Graphene," *Nano letters*, vol. 10, no. 4, pp. 1308–1313, 2010.

[167] B. Gao, G. Hartland, T. Fang, M. Kelly, D. Jena, H. Xing, and L. Huang, "Studies of Intrinsic Hot Phonon Dynamics in Suspended Graphene by Transient Absorption Microscopy," *Nano letters*, vol. 11, no. 8, pp. 3184–3189, 2011.

[168] N. Kumar, J. He, D. He, Y. Wang, and H. Zhao, "Charge Carrier Dynamics in Bulk MoS_2 Crystal Studied by Transient Absorption Microscopy," *Journal of Applied Physics*, vol. 113, no. 13, p. 133702, 2013.

[169] B. P. Mehl, J. R. Kirschbrown, R. L. House, and J. M. Papanikolas, "The End is Different than the Middle: Spatially Dependent Dynamics in ZnO Rods Observed by Femtosecond Pump–Probe Microscopy," *The Journal of Physical Chemistry Letters*, vol. 2, no. 14, pp. 1777–1781, 2011.

[170] G. V. Hartland, "Ultrafast Studies of Single Semiconductor and Metal Nanostructures through Transient Absorption Microscopy," *Chemical Science*, vol. 1, no. 3, pp. 303–309, 2010.

[171] F. D. Fuller, J. Pan, A. Gelzinis, V. Butkus, S. S. Senlik, D. E. Wilcox, C. F. Yocum, L. Valkunas, D. Abramavicius, and J. P. Ogilvie, "Vibronic Coherence in Oxygenic Photosynthesis," *Nature chemistry*, vol. 6, no. 8, pp. 706–711, 2014.

[172] J. D. Gaynor, T. L. Courtney, M. Balasubramanian, and M. Khalil, "Fourier Transform Two-Dimensional Electronic-Vibrational Spectroscopy Using an Octave-Spanning Mid-IR Probe," *Optics letters*, vol. 41, no. 12, pp. 2895–2898, 2016.

[173] H. Bronstein, C. B. Nielsen, B. C. Schroeder, and I. McCulloch, "The Role of Chemical Design in the Performance of Organic Semiconductors," *Nature Reviews Chemistry*, vol. 4, no. 2, pp. 66–77, 2020.

[174] P. Kukura, S. Yoon, and R. A. Mathies, "Femtosecond Stimulated Raman Spectroscopy," 2006.

[175] D. P. Hoffman and R. A. Mathies, "Femtosecond Stimulated Raman Exposes the Role of Vibrational Coherence in Condensed-Phase Photoreactivity," *Accounts of chemical research*, vol. 49, no. 4, pp. 616–625, 2016.

[176] Y. Hontani, M. Kloz, T. Polívka, M. K. Shukla, R. Sobotka, and J. T. Kennis, "Molecular Origin of Photoprotection in Cyanobacteria Probed by Watermarked Femtosecond Stimulated Raman Spectroscopy," *The journal of physical chemistry letters*, vol. 9, no. 7, pp. 1788–1792, 2018.

[177] M. Jen, S. Lee, K. Jeon, S. Hussain, and Y. Pang, "Ultrafast Intramolecular Proton Transfer of Alizarin Investigated by Femtosecond Stimulated Raman Spectroscopy," *The Journal of Physical Chemistry B*, vol. 121, no. 16, pp. 4129–4136, 2017.

[178] G. Batignani, E. Pontecorvo, C. Ferrante, M. Aschi, C. G. Elles, and T. Scopigno, "Visualizing Excited-State Dynamics of a Diaryl Thiophene: Femtosecond Stimulated Raman Scattering as a Probe of Conjugated Molecules," *The journal of physical chemistry letters*, vol. 7, no. 15, pp. 2981–2988, 2016.

[179] A. Weigel and N. Ernsting, "Excited Stilbene: Intramolecular Vibrational Redistribution and Solvation Studied by Femtosecond Stimulated Raman Spectroscopy," *The Journal of Physical Chemistry B*, vol. 114, no. 23, pp. 7879–7893, 2010.

[180] H. Kuramochi, S. Takeuchi, and T. Tahara, "Ultrafast Structural Evolution of Photoactive Yellow Protein Chromophore Revealed by Ultraviolet Resonance Femtosecond Stimulated Raman Spectroscopy," *The Journal of Physical Chemistry Letters*, vol. 3, no. 15, pp. 2025–2029, 2012.

[181] K. E. Brown, B. S. Veldkamp, D. T. Co, and M. R. Wasielewski, "Vibrational Dynamics of a Perylene–Perylenediimide Donor–Acceptor Dyad Probed with Femtosecond Stimulated Raman Spectroscopy," *The journal of physical chemistry letters*, vol. 3, no. 17, pp. 2362–2366, 2012.

[182] L. Tang, L. Zhu, M. A. Taylor, Y. Wang, S. J. Remington, and C. Fang, "Excited State Structural Evolution of a GFP Single-Site Mutant Tracked by Tunable Femtosecond-Stimulated Raman Spectroscopy," *Molecules*, vol. 23, no. 9, p. 2226, 2018.

[183] J. Anthony, D. Eaton, and S. Parkin, "A Road Map to Stable, Soluble, Easily Crystallized Pentacene Derivatives," *Organic letters*, vol. 4, no. 1, pp. 15–18, 2002.

[184] J. Anthony, J. Brooks, D. Eaton, and S. Parkin, "Functionalized Pentacene: Improved Electronic Properties From Control of Solid-State Order," *Journal of the American Chemical Society*, vol. 123, no. 38, pp. 9482–9483, 2001.

[185] H. T. Yi, M. M. Payne, J. E. Anthony, and V. Podzorov, "Ultra-Flexible Solution-Processed Organic Field-Effect Transistors," *Nature communications*, vol. 3, no. 1, pp. 1–7, 2012.

[186] W. R. Silva, C. T. Graefe, and R. R. Frontiera, "Toward Label-Free Super-Resolution Microscopy," *Acs Photonics*, vol. 3, no. 1, pp. 79–86, 2016.

[187] P. Tournois, "Acousto-Optic Programmable Dispersive Filter for Adaptive Compensation of Group Delay Time Dispersion in Laser Systems," *Optics communications*, vol. 140, no. 4-6, pp. 245–249, 1997.

[188] D. Kaplan, P. Tournois, B. Chatel, and A. Monmayrant, "Tunable Wavelength Pulse Shaping of Visible NOPA Outputs with an Acousto-Optic Programmable Dispersive Filter," in *International Conference on Ultrafast Phenomena*, p. TuE40, Optical Society of America, 2004.

[189] S. Wood, G. Rigas, A. Zoladek-Lemanczyk, J. C. Blakesley, S. Georgakopoulos, M. Mas-Torrent, M. Shkunov, and F. A. Castro, "Precise Characterisation of Molecular Orientation in a Single Crystal Field-Effect Transistor Using Polarised Raman Spectroscopy," *Scientific reports*, vol. 6, no. 1, pp. 1–8, 2016.

[190] D. A. Kadri, D. A. Karim, M. Seck, K. Diouma, P. Marcel, *et al.*, "Optimization of 6,13Bis(triisopropylsilylethynyl) Pentacene (TIPS-Pentacene) Organic Field Effect Transistor: Annealing Temperature and Solvent Effects," *Materials Sciences and Applications*, vol. 9, no. 11, p. 900, 2018.

[191] D. T. James, B. C. Kjellander, W. T. Smaal, G. H. Gelinck, C. Combe, I. McCulloch, R. Wilson, J. H. Burroughes, D. D. Bradley, and J. Kim, "Thin-Film Morphology of Inkjet-Printed Single-Droplet Organic Transistors Using Polarized Raman Spectroscopy: Effect of Blending TIPS-Pentacene with Insulating Polymer," *ACS nano*, vol. 5, no. 12, pp. 9824–9835, 2011.

[192] A. Stein, F. Maaß, and P. Tegeder, "Triisopropylsilylethynyl-Pentacene on Au (111): Adsorption Properties, Electronic Structure, and Singlet Fission Dynamics," *The Journal of Physical Chemistry C*, vol. 121, no. 33, pp. 18075–18083, 2017.

[193] D. Choi, B. Ahn, S. H. Kim, K. Hong, M. Ree, and C. E. Park, "High-Performance Triisopropylsilylethynyl Pentacene Transistors via Spin Coating with a Crystallization-Assisting Layer," *ACS applied materials & interfaces*, vol. 4, no. 1, pp. 117–122, 2012.

[194] J. Wade, F. Steiner, D. Niedzialek, D. T. James, Y. Jung, D. Yun, D. D. Bradley, J. Nelson, and J. Kim, "Charge Mobility Anisotropy of Functionalized Pentacenes in Organic Field Effect Transistors Fabricated by Solution Processing," *Journal of Materials Chemistry C*, vol. 2, no. 47, pp. 10110–10115, 2014.

[195] K. Sakamoto, J. Ueno, K. Bulgarevich, and K. Miki, "Anisotropic Charge Transport and Contact Resistance of 6,13-Bis(triisopropylsilylethynyl) Pentacene Field-Effect Transistors Fabricated by a Modified Flow-Coating Method," *Applied Physics Letters*, vol. 100, no. 12, p. 75, 2012.

[196] J. Chen, C. K. Tee, M. Shtein, D. C. Martin, and J. Anthony, "Controlled Solution Deposition and Systematic Study of Charge-Transport Anisotropy in Single Crystal and Single-Crystal Textured TIPS Pentacene Thin Films," *Organic Electronics*, vol. 10, no. 4, pp. 696–703, 2009.

[197] C. Grieco, G. S. Doucette, R. D. Pensack, M. M. Payne, A. Rimshaw, G. D. Scholes, J. E. Anthony, and J. B. Asbury, "Dynamic Exchange During Triplet Transport in Nanocrystalline TIPS-Pentacene Films," *Journal of the American Chemical Society*, vol. 138, no. 49, pp. 16069–16080, 2016.

[198] J. Herz, T. Buckup, F. Paulus, J. Engelhart, U. H. Bunz, and M. Motzkus, "Unveiling Singlet Fission Mediating States in TIPS-pentacene and its Aza Derivatives," *The Journal of Physical Chemistry A*, vol. 119, no. 25, pp. 6602–6610, 2015.

[199] R. D. Pensack, A. J. Tilley, C. Grieco, G. E. Purdum, E. E. Ostroumov, D. B. Granger, D. G. Oblinsky, J. C. Dean, G. S. Doucette, J. B. Asbury, *et al.*, "Striking the Right Balance of Intermolecular Coupling for High-Efficiency Singlet Fission," *Chemical science*, vol. 9, no. 29, pp. 6240–6259, 2018.

[200] S. Lee, D. Hwang, S. I. Jung, and D. Kim, "Electron Transfer from Triplet State of TIPS-Pentacene Generated by Singlet Fission Processes to $CH_3NH_3PbI_3$ Perovskite," *The journal of physical chemistry letters*, vol. 8, no. 4, pp. 884–888, 2017.

[201] T. Mino, Y. Saito, H. Yoshida, S. Kawata, and P. Verma, "Molecular Orientation Analysis of Organic Thin Films by z-Polarization Raman Microscope," *Journal of Raman Spectroscopy*, vol. 43, no. 12, pp. 2029–2034, 2012.

[202] N. Onojima, A. Nakamura, H. Saito, and N. Daicho, "Aligned Growth of TIPS Pentacene Crystalline Domains Adhered to Au Stripes Formed on SiO_2 Surfaces," *Journal of Crystal Growth*, vol. 432, pp. 146–151, 2015.

[203] J. Chen, D. C. Martin, and J. E. Anthony, "Morphology and Molecular Orientation of Thin-Film Bis(triisopropylsilylethynyl) Pentacene," *Journal of materials research*, vol. 22, no. 6, pp. 1701–1709, 2007.

[204] E. Binder, T. Kuhn, and G. Mahler, "Coherent Intraband and Interband Dynamics in Double Quantum Wells: Exciton and Free-Carrier Effects," *Physical Review B*, vol. 50, no. 24, p. 18319, 1994.

[205] L. Q. Phuong, Y. Yamada, M. Nagai, N. Maruyama, A. Wakamiya, and Y. Kanemitsu, "Free Carriers Versus Excitons in $CH_3NH_3PbI_3$ Perovskite Thin Films at Low Temperatures: Charge Transfer from the Orthorhombic Phase to the Tetragonal Phase," *The journal of physical chemistry letters*, vol. 7, no. 13, pp. 2316–2321, 2016.

[206] W. Wang, Y. Li, X. Wang, Y. Lv, S. Wang, K. Wang, Y. Shi, L. Xiao, Z. Chen, and Q. Gong, "Density-Dependent Dynamical Coexistence of Excitons and Free Carriers in the Organolead Perovskite $CH_3NH_3PbI_3$," *Physical Review B*, vol. 94, no. 14, p. 140302, 2016.

[207] R. Endres, D. Cox, R. Singh, and S. Pati, "Mediation of Long Range Charge Transfer by Kondo Bound States," *Physical review letters*, vol. 88, no. 16, p. 166601, 2002.

[208] Y. Jiang, Z. Shuai, and M. Liu, "Roles of Long-Range Hopping, Quantum Nuclear Effect, and Exciton Delocalization in Exciton Transport in Organic Semiconductors: A Multiscale Study," *The Journal of Physical Chemistry C*, vol. 122, no. 32, pp. 18365–18375, 2018.

[209] C. Ramanan, A. Smeigh, J. Anthony, T. Marks, and M. Wasielewski, "Competition Between Singlet Fission and Charge Separation in Solution-Processed Blend Films of 6,13-Bis(triisopropylsilylethynyl) Pentacene with Sterically-Encumbered Perylene-3,4:9,10-Bis(dicarboximide)s," *Journal of the American Chemical Society*, vol. 134, no. 1, pp. 386–397, 2012.

[210] Y. Wu, K. Liu, H. Liu, Y.-D. Zhang, H.-L. Zhang, J. Yao, and H. Fu, "Impact of Intermolecular Distance on Singlet Fission in a Series of TIPS Pentacene Compounds," *The journal of physical chemistry letters*, vol. 5, no. 20, pp. 3451–3455, 2014.

[211] B. D. Folie, J. B. Haber, S. Refaely-Abramson, J. B. Neaton, and N. S. Ginsberg, "Long-Lived Correlated Triplet Pairs in a π-Stacked Crystalline Pentacene Derivative," *Journal of the American Chemical Society*, vol. 140, no. 6, pp. 2326–2335, 2018.

[212] W. Chan, M. Ligges, and X. Zhu, "The Energy Barrier in Singlet Fission can be Overcome through Coherent Coupling and Entropic Gain," *Nature chemistry*, vol. 4, no. 10, pp. 840–845, 2012.

[213] W. Bao, X. Cai, D. Kim, K. Sridhara, and M. S. Fuhrer, "High Mobility Ambipolar MoS_2 Field-Effect Transistors: Substrate and Dielectric Effects," *Applied Physics Letters*, vol. 102, no. 4, p. 042104, 2013.

[214] R. Ruiz, A. Papadimitratos, A. C. Mayer, and G. G. Malliaras, "Thickness Dependence of Mobility in Pentacene Thin-Film Transistors," *Advanced Materials*, vol. 17, no. 14, pp. 1795–1798, 2005.

[215] C. Bell, S. Harashima, Y. Kozuka, M. Kim, B. G. Kim, Y. Hikita, and H. Hwang, "Dominant Mobility Modulation by the Electric Field Effect at the $LaAlO_3/SrTiO_3$ Interface," *Physical review letters*, vol. 103, no. 22, p. 226802, 2009.

[216] T. Dramstad, Z. Sohrabpour, and A. Massari, "Thickness Dependent Molecular Structure at the Interfaces of Thin Films of Sexithiophene," *Submitted*, 2020.

[217] S. Yu, Y. Ni, L. He, and Q. Ye, "Tunable Formation of Ordered Wrinkles in Metal Films with Controlled Thickness Gradients Deposited on Soft Elastic Substrates," *ACS applied materials & interfaces*, vol. 7, no. 9, pp. 5160–5167, 2015.

[218] W. Yin, J. Yang, J. Kang, Y. Yan, and S. Wei, "Halide Perovskite Materials for Solar Cells: a Theoretical Review," *Journal of Materials Chemistry A*, vol. 3, no. 17, pp. 8926–8942, 2015.

[219] S. D. Stranks, G. E. Eperon, G. Grancini, C. Menelaou, M. J. Alcocer, T. Leijtens, L. M. Herz, A. Petrozza, and H. J. Snaith, "Electron-Hole Diffusion Lengths Exceeding 1 Micrometer in an Organometal Trihalide Perovskite Absorber," *Science*, vol. 342, no. 6156, pp. 341–344, 2013.

[220] H. Wei, Y. Fang, P. Mulligan, W. Chuirazzi, H. Fang, C. Wang, B. R. Ecker, Y. Gao, M. A. Loi, L. Cao, *et al.*, "Sensitive X-Ray Detectors Made of Methylammonium Lead Tribromide Perovskite Single Crystals," *Nature Photonics*, vol. 10, no. 5, pp. 333–339, 2016.

[221] L. Protesescu, S. Yakunin, M. I. Bodnarchuk, F. Krieg, R. Caputo, C. H. Hendon, R. X. Yang, A. Walsh, and M. V. Kovalenko, "Nanocrystals of Cesium Lead Halide Perovskites ($CsPbX_3$, X= Cl, Br, and I): Novel Optoelectronic Materials Showing Bright Emission with Wide Color Gamut," *Nano letters*, vol. 15, no. 6, pp. 3692–3696, 2015.

[222] C. Wang, Y. Zhang, A. Wang, Q. Wang, H. Tang, W. Shen, Z. Li, and Z. Deng, "Controlled Synthesis of Composition Tunable Formamidinium Cesium Double Cation Lead Halide Perovskite Nanowires and Nanosheets with Improved Stability," *Chemistry of Materials*, vol. 29, no. 5, pp. 2157–2166, 2017.

[223] Z. Guo, Y. Wan, M. Yang, J. Snaider, K. Zhu, and L. Huang, "Long-Range Hot-Carrier Transport in Hybrid Perovskites Visualized by Ultrafast Microscopy," *Science*, vol. 356, no. 6333, pp. 59–62, 2017.

[224] A. H. Hill, K. E. Smyser, C. L. Kennedy, E. S. Massaro, and E. M. Grumstrup, "Screened Charge Carrier Transport in Methylammonium Lead Iodide Perovskite Thin Films," *The journal of physical chemistry letters*, vol. 8, no. 5, pp. 948–953, 2017.

[225] D. H. Arias, D. T. Moore, J. van de Lagemaat, and J. C. Johnson, "Direct Measurements of Carrier Transport in Polycrystalline Methylammonium Lead Iodide

Perovskite Films with Transient Grating Spectroscopy," *The journal of physical chemistry letters*, vol. 9, no. 19, pp. 5710–5717, 2018.

[226] O. F. Williams, N. Zhou, J. Hu, Z. Ouyang, A. Kumbhar, W. You, and A. M. Moran, "Imaging Excited State Dynamics in Layered 2D Perovskites with Transient Absorption Microscopy," *The Journal of Physical Chemistry A*, vol. 123, no. 51, pp. 11012–11021, 2019.

[227] J. Sung, C. Schnedermann, L. Ni, A. Sadhanala, R. Y. Chen, C. Cho, L. Priest, J. M. Lim, H. Kim, B. Monserrat, *et al.*, "Long-Range Ballistic Propagation of Carriers in Methylammonium Lead Iodide Perovskite Thin Films," *Nature Physics*, vol. 16, no. 2, pp. 171–176, 2020.

[228] P. Pistor, A. Ruiz, A. Cabot, and V. Izquierdo-Roca, "Advanced Raman Spectroscopy of Methylammonium Lead Iodide: Development of a Non-Destructive Characterisation Methodology," *Scientific reports*, vol. 6, no. 1, pp. 1–8, 2016.

[229] M. Park, N. Kornienko, S. E. Reyes-Lillo, M. Lai, J. B. Neaton, P. Yang, and R. A. Mathies, "Critical Role of Methylammonium Librational Motion in Methylammonium Lead Iodide ($CH_3NH_3PbI_3$) Perovskite Photochemistry," *Nano letters*, vol. 17, no. 7, pp. 4151–4157, 2017.

[230] M. A. Perez-Osorio, Q. Lin, R. T. Phillips, R. L. Milot, L. M. Herz, M. B. Johnston, and F. Giustino, "Raman Spectrum of the Organic–Inorganic Halide Perovskite $CH_3NH_3PbI_3$ from First Principles and High-Resolution Low-Temperature Raman Measurements," *The Journal of Physical Chemistry C*, vol. 122, no. 38, pp. 21703–21717, 2018.

[231] K. Nakada, Y. Matsumoto, Y. Shimoi, K. Yamada, and Y. Furukawa, "Temperature-Dependent Evolution of Raman Spectra of Methylammonium Lead Halide Perovskites, $CH_3NH_3PbX_3$ (X= I, Br)," *Molecules*, vol. 24, no. 3, p. 626, 2019.

[232] T. Ben-Uliel, H. Aviv, J. Zhou, M. Li, S. Avadyayev, O. Kapon, V. Damle, C. Yi, and Y. Tischler, "Raman Scattering Obtained from Laser Excitation of $MAPbI_3$ Single Crystal," *Applied Materials Today*, vol. 19, p. 100571, 2020.

[233] M. I. Saidaminov, A. L. Abdelhady, B. Murali, E. Alarousu, V. M. Burlakov, W. Peng, I. Dursun, L. Wang, Y. He, G. Maculan, *et al.*, "High-Quality Bulk Hybrid Perovskite Single Crystals within Minutes by Inverse Temperature Crystallization," *Nature communications*, vol. 6, no. 1, pp. 1–6, 2015.

[234] A. Kaminskii, N. Tanaka, H. Eichler, H. Rhee, K. Ueda, K. Takaichi, A. Shirakawa, M. Tokurakawa, Y. Kintaka, S. Kuretake, *et al.*, "Picosecond Raman Induced Stokes and Anti-Stokes Lasing in Fine-Grained Ba (Sn, Zr, Mg, Ta) O_3 Crystalline Ceramics with the Cubic Perovskite Structure," *Laser Physics Letters*, vol. 4, no. 11, p. 819, 2007.

[235] E. J. Candès and M. B. Wakin, "An Introduction to Compressive Sampling," *IEEE signal processing magazine*, vol. 25, no. 2, pp. 21–30, 2008.

[236] J. C. Ye, "Compressed Sensing MRI: a Review from Signal Processing Perspective," *BMC Biomedical Engineering*, vol. 1, no. 1, pp. 1–17, 2019.

[237] J. A. Dunbar, D. G. Osborne, J. M. Anna, and K. J. Kubarych, "Accelerated 2D-IR Using Compressed Sensing," *The Journal of Physical Chemistry Letters*, vol. 4, no. 15, pp. 2489–2492, 2013.

[238] S. Adhikari, C. L. Cortes, X. Wen, S. Panuganti, D. J. Gosztola, R. D. Schaller, G. P. Wiederrecht, and S. K. Gray, "Accelerating Ultrafast Spectroscopy with Compressive Sensing," *Physical Review Applied*, vol. 15, no. 2, p. 024032, 2021.

[239] D. F. Galvis-Carreño, Y. H. Mejía-Melgarejo, and H. Arguello-Fuentes, "Efficient Reconstruction of Raman Spectroscopy Imaging Based on Compressive Sensing," *Dyna*, vol. 81, no. 188, pp. 116–124, 2014.

[240] O. Denk, K. Zheng, D. Zigmantas, and K. Žídek, "Compressive Imaging of Transient Absorption Dynamics on the Femtosecond Timescale," *Optics express*, vol. 27, no. 7, pp. 10234–10246, 2019.

[241] A. M. Müller, Y. S. Avlasevich, W. W. Schoeller, K. Müllen, and C. J. Bardeen, "Exciton Fission and Fusion in Bis(tetracene) Molecules with Different Covalent Linker Structures," *Journal of the American Chemical Society*, 2007.

[242] K. M. Felter, R. K. Dubey, and F. C. Grozema, "Relation Between Molecular Packing and Singlet Fission in Thin Films of Brominated Perylenediimides," *Journal of Chemical Physics*, 2019.

[243] K. Kuroda, K. Yazaki, Y. Tanaka, M. Akita, H. Sakai, T. Hasobe, N. V. Tkachenko, and M. Yoshizawa, "A Pentacene-Based Nanotube Displaying Enriched Electrochemical and Photochemical Activities," *Angewandte Chemie - International Edition*, 2019.

[244] C. Hetzer, B. S. Basel, S. M. Kopp, F. Hampel, F. J. White, T. Clark, D. M. Guldi, and R. R. Tykwinski, "Chromophore Multiplication To Enable Exciton Delocalization and Triplet Diffusion Following Singlet Fission in Tetrameric Pentacene," *Angewandte Chemie - International Edition*, 2019.

[245] J. L. Ryerson, A. Zaykov, L. E. Aguilar Suarez, R. W. Havenith, B. R. Stepp, P. I. Dron, J. Kaleta, A. Akdag, S. J. Teat, T. F. Magnera, J. R. Miller, Z. Havlas, R. Broer, S. Faraji, J. Michl, and J. C. Johnson, "Structure and Photophysics of Indigoids for Singlet Fission: Cibalackrot," *Journal of Chemical Physics*, 2019.

[246] M. Chen, M. D. Krzyaniak, J. N. Nelson, Y. J. Bae, S. M. Harvey, R. D. Schaller, R. M. Young, and M. R. Wasielewski, "Quintet-Triplet Mixing Determines the Fate of the Multiexciton State Produced by Singlet Fission in a Terrylenediimide Dimer at Room Temperature," *Proceedings of the National Academy of Sciences of the United States of America*, 2019.

[247] Y. Matsui, S. Kawaoka, H. Nagashima, T. Nakagawa, N. Okamura, T. Ogaki, E. Ohta, S. Akimoto, A. Sato-Tomita, S. Yagi, Y. Kobori, and H. Ikeda, "Exergonic Intramolecular Singlet Fission of an Adamantane-Linked Tetracene Dyad via Twin Quintet Multiexcitons," *Journal of Physical Chemistry C*, 2019.

[248] E. A. Buchanan, J. Kaleta, J. Wen, S. H. Lapidus, I. Císařová, Z. Havlas, J. C. Johnson, and J. Michl, "Molecular Packing and Singlet Fission: The Parent and Three Fluorinated 1,3-Diphenylisobenzofurans," *Journal of Physical Chemistry Letters*, 2019.

[249] S. Nakamura, H. Sakai, H. Nagashima, Y. Kobori, N. V. Tkachenko, and T. Hasobe, "Quantitative Sequential Photoenergy Conversion Process from Singlet Fission to Intermolecular Two-Electron Transfers Utilizing Tetracene Dimer," *ACS Energy Letters*, 2019.

[250] B. D. Datko, R. Grimm, D. J. Walwark, B. Burnside, and J. K. Grey, "Resolving Population Dynamics and Interactions of Multiple Triplet Excitons One Molecule at a Time," *Journal of Chemical Physics*, 2019.

[251] N. Aggarwal and A. Patnaik, "Dimeric Conformation Sensitive Electronic Excited States of Tetracene Congeners and their Unconventional Non-Fluorescent Behaviour," *Journal of Chemical Sciences*, 2019.

[252] S. Bange, U. Scherf, and J. M. Lupton, "Absence of Singlet Fission and Carrier Multiplication in a Model Conjugated Polymer: Tracking the Triplet Population through Phosphorescence," *Journal of the American Chemical Society*, 2012.

[253] D. M. Finton, E. A. Wolf, V. S. Zoutenbier, K. A. Ward, and I. Biaggio, "Routes to Singlet Exciton Fission in Rubrene Crystals and Amorphous Films," *AIP Advances*, 2019.

[254] Y. J. Bae, J. A. Christensen, G. Kang, J. Zhou, R. M. Young, Y. L. Wu, R. P. Van Duyne, G. C. Schatz, and M. R. Wasielewski, "Substituent Effects on Energetics and Crystal Morphology Modulate Singlet Fission in 9,10-bis(phenylethynyl)anthracenes," *Journal of Chemical Physics*, 2019.

[255] N. Alagna, J. L. Pérez Lustres, N. Wollscheid, Q. Luo, J. Han, A. Dreuw, F. L. Geyer, V. Brosius, U. H. Bunz, T. Buckup, and M. Motzkus, "Singlet Fission in Tetraaza-TIPS-Pentacene Oligomers: From fs Excitation to μs Triplet Decay via the Biexcitonic State," *Journal of Physical Chemistry B*, 2019.

[256] K. Sato and R. Katoh, "Fluorescence Properties of -Perylene Crystals Prepared by a Physical Vapor Transport Method Under Atmospheric Pressure," *Chemical Physics Letters*, 2019.

[257] I. Papadopoulos, J. Zirzlmeier, C. Hetzer, Y. J. Bae, M. D. Krzyaniak, M. R. Wasielewski, T. Clark, R. R. Tykwinski, and D. M. Guldi, "Varying the Inter-pentacene Electronic Coupling to Tune Singlet Fission," *Journal of the American Chemical Society*, 2019.

[258] A. N. Stuart, P. C. Tapping, E. Schrefl, D. M. Huang, and T. W. Kee, "Controlling the Efficiency of Singlet Fission in TIPS-Pentacene/Polymer Composite Nanoparticles," *Journal of Physical Chemistry C*, 2019.

[259] J. P. Mora-Fuentes, I. Papadopoulos, D. Thiel, R. Álvarez-Boto, D. Cortizo-Lacalle, T. Clark, M. Melle-Franco, D. M. Guldi, and A. Mateo-Alonso, "Singlet Fission in Pyrene-Fused Azaacene Dimers," *Angewandte Chemie - International Edition*, 2020.

[260] L. Wang, S. Bai, Y. Wu, Y. Liu, J. Yao, and H. Fu, "Revealing the Nature of Singlet Fission under the Veil of Internal Conversion," *Angewandte Chemie - International Edition*, 2020.

[261] B. Manna and A. Nandi, "Exploration of Photophysics and Presence of Long Singlet Exciton Diffusion Length in Dibenz[a,h]anthracene Nanoaggregates," *Journal of Photochemistry and Photobiology A: Chemistry*, 2020.

[262] V. Jankus, E. W. Snedden, D. W. Bright, E. Arac, D. Dai, and A. P. Monkman, "Competition Between Polaron Pair Formation and Singlet Fission Observed in Amorphous Rubrene Films," *Physical Review B - Condensed Matter and Materials Physics*, 2013.

[263] M. Chen, N. E. Powers-Riggs, A. F. Coleman, R. M. Young, and M. R. Wasielewski, "Singlet Fission in Quaterrylenediimide Thin Films," *Journal of Physical Chemistry C*, 2020.

[264] Y. Hong, J. Kim, W. Kim, C. Kaufmann, H. Kim, F. Würthner, and D. Kim, "Efficient Multiexciton State Generation in Charge-Transfer-Coupled Perylene Bisimide Dimers via Structural Control," *Journal of the American Chemical Society*, 2020.

[265] S. Masoomi-Godarzi, M. Liu, Y. Tachibana, V. D. Mitchell, L. Goerigk, K. P. Ghiggino, T. A. Smith, and D. J. Jones, "Liquid Crystallinity as a Self-Assembly Motif for High-Efficiency, Solution-Processed, Solid-State Singlet Fission Materials," *Advanced Energy Materials*, 2019.

[266] J. N. Mastron, S. T. Roberts, R. E. McAnally, M. E. Thompson, and S. E. Bradforth, "Aqueous colloidal acene nanoparticles: a new platform for studying singlet fission," *The Journal of Physical Chemistry B*, vol. 117, no. 49, pp. 15519–15526, 2013.

[267] B. J. Walker, A. J. Musser, D. Beljonne, and R. H. Friend, "Singlet Exciton Fission in Solution," *Nature chemistry*, vol. 5, no. 12, p. 1019, 2013.

[268] L. Ma, K. Zhang, C. Kloc, H. Sun, C. Soci, M. E. Michel-Beyerle, and G. G. Gurzadyan, "Fluorescence from Rubrene Single Crystals: Interplay of Singlet Fission and Energy Trapping," *Physical Review B - Condensed Matter and Materials Physics*, 2013.

[269] G. B. Piland, J. J. Burdett, D. Kurunthu, and C. J. Bardeen, "Magnetic Field Effects on Singlet Fission and Fluorescence Decay Dynamics in Amorphous Rubrene," *Journal of Physical Chemistry C*, 2013.

[270] R. J. Dillon, G. B. Piland, and C. J. Bardeen, "Different Rates of Singlet Fission in Monoclinic Versus Orthorhombic Crystal Forms of Diphenylhexatriene," *Journal of the American Chemical Society*, 2013.

[271] S. W. Eaton, L. E. Shoer, S. D. Karlen, S. M. Dyar, E. A. Margulies, B. S. Veldkamp, C. Ramanan, D. A. Hartzler, S. Savikhin, T. J. Marks, and M. R. Wasielewski, "Singlet Exciton Fission in Polycrystalline Thin Films of a Slip-Stacked Perylenediimide," *Journal of the American Chemical Society*, 2013.

[272] X. Wen, P. Yu, C. T. Yuan, X. Ma, and J. Tang, "Singlet and Triplet Carrier Dynamics in Rubrene Single Crystal," *Journal of Physical Chemistry C*, 2013.

[273] J. C. Johnson, A. Akdag, M. Zamadar, X. Chen, A. F. Schwerin, I. Paci, M. B. Smith, Z. Havlas, J. R. Miller, M. A. Ratner, A. J. Nozik, and J. Michl, "Toward Designed Singlet Fission: Solution Photophysics of Two Indirectly Coupled Covalent Dimers of 1,3-diphenylisobenzofuran," *Journal of Physical Chemistry B*, 2013.

[274] V. M. Nichols, M. T. Rodriguez, G. B. Piland, F. Tham, V. N. Nesterov, W. J. Youngblood, and C. J. Bardeen, "Assessing the Potential of Peropyrene as a Singlet Fission Material: Photophysical Properties in Solution and the Solid State," *Journal of Physical Chemistry C*, 2013.

[275] M. J. Tayebjee, R. G. Clady, and T. W. Schmidt, "The Exciton Dynamics in Tetracene Thin Films," *Physical Chemistry Chemical Physics*, 2013.

[276] B. Zhang, C. Zhang, R. Wang, Z. Tan, Y. Liu, W. Guo, X. Zhai, Y. Cao, X. Wang, and M. Xiao, "Nonlinear Density Dependence of Singlet Fission Rate in Tetracene Films," *Journal of Physical Chemistry Letters*, 2014.

[277] S. Yost, J. Lee, W. Wilson, T. Wu, D. McMahon, R. Parkhurst, N. Thompson, D. Congreve, A. Rao, and K. Johnson, "A Transferable Model for Singlet-Fission Kinetics," *Nature chemistry*, vol. 6, no. 6, pp. 492–497, 2014.

[278] L. Ma, K. J. Tan, H. Jiang, C. Kloc, M. E. Michel-Beyerle, and G. G. Gurzadyan, "Excited-State Dynamics in an α-Perylene Single Crystal: Two-Photon- and Consecutive Two-Quantum-Induced Singlet Fission," *Journal of Physical Chemistry A*, 2014.

[279] S. Selvakumar, K. Sivaji, A. Arulchakkaravarthi, and S. Sankar, "Electron Momentum Distribution and Singlet-Singlet Annihilation in the Organic Anthracene Molecular Crystals Using Positron 2D-ACAR and Fluorescence Spectroscopy," *Physical Chemistry Chemical Physics*, 2014.

[280] G. B. Piland, J. J. Burdett, T. Y. Hung, P. H. Chen, C. F. Lin, T. L. Chiu, J. H. Lee, and C. J. Bardeen, "Dynamics of Molecular Excitons near a Semiconductor Surface Studied by Fluorescence Quenching of Polycrystalline Tetracene on Silicon," *Chemical Physics Letters*, 2014.

[281] B. Gieseking, T. Schmeiler, B. Müller, C. Deibel, B. Engels, V. Dyakonov, and J. Pflaum, "Effects of Characteristic Length Scales on the Exciton Dynamics in Rubrene Single Crystals," *Physical Review B - Condensed Matter and Materials Physics*, 2014.

[282] J. L. Ryerson, J. N. Schrauben, A. J. Ferguson, S. C. Sahoo, P. Naumov, Z. Havlas, J. Michl, A. J. Nozik, and J. C. Johnson, "Two Thin Film Polymorphs of the Singlet Fission Compound 1,3-diphenylisobenzofuran," *Journal of Physical Chemistry C*, 2014.

[283] J. C. Johnson, A. J. Nozik, and J. Michl, "High Triplet Yield from Singlet Fission in a Thin Film of 1,3-diphenylisobenzofuran," *Journal of the American Chemical Society*, 2010.

[284] J. Li, Z. Chen, Q. Zhang, Z. Xiong, and Y. Zhang, "Temperature-Dependent Singlet Exciton Fission Observed in Amorphous Rubrene Films," *Organic Electronics*, 2015.

[285] J. Li, Z. Chen, Y. Lei, Z. Xiong, and Y. Zhang, "Competition Between Singlet Exciton Fission, Radiation, and Dissociation Measured in Rubrene-Doped Amorphous Films," *Synthetic Metals*, 2015.

[286] N. J. Thompson, E. Hontz, W. Chang, T. Van Voorhis, and M. Baldo, "Magnetic Field Dependence of Singlet Fission in Solutions of Diphenyl Tetracene," *Philosophical Transactions of the Royal Society A: Mathematical, Physical and Engineering Sciences*, 2015.

[287] S. Lukman, A. J. Musser, K. Chen, S. Athanasopoulos, C. K. Yong, Z. Zeng, Q. Ye, C. Chi, J. M. Hodgkiss, J. Wu, *et al.*, "Tuneable Singlet Exciton Fission and Triplet–Triplet Annihilation in an Orthogonal Pentacene Dimer," *Advanced Functional Materials*, vol. 25, no. 34, pp. 5452–5461, 2015.

[288] R. Wang, C. Zhang, B. Zhang, Y. Liu, X. Wang, and M. Xiao, "Magnetic Dipolar Interaction Between Correlated Triplets Created by Singlet Fission in Tetracene Crystals," *Nature Communications*, 2015.

[289] O. Varnavski, N. Abeyasinghe, J. Aragó, J. J. Serrano-Pérez, E. Ortí, J. T. López Navarrete, K. Takimiya, D. Casanova, J. Casado, and T. Goodson, "High Yield Ultrafast Intramolecular Singlet Exciton Fission in a Quinoidal Bithiophene," *Journal of Physical Chemistry Letters*, 2015.

[290] S. N. Sanders, E. Kumarasamy, A. B. Pun, M. T. Trinh, B. Choi, J. Xia, E. J. Taffet, J. Z. Low, J. R. Miller, X. Roy, *et al.*, "Quantitative Intramolecular Singlet Fission in Bipentacenes," *Journal of the American Chemical Society*, vol. 137, no. 28, pp. 8965–8972, 2015.

[291] G. B. Piland and C. J. Bardeen, "How Morphology Affects Singlet Fission in Crystalline Tetracene," *Journal of Physical Chemistry Letters*, 2015.

[292] H. Liu, V. M. Nichols, L. Shen, S. Jahansouz, Y. Chen, K. M. Hanson, C. J. Bardeen, and X. Li, "Synthesis and Photophysical Properties of a "Face-to-Face" Stacked Tetracene Dimer," *Physical Chemistry Chemical Physics*, 2015.

[293] A. Schwerin, J. C. Johnson, M. B. Smith, P. Sreearunothai, D. Popović, J. Černý, Z. Havias, I. Paci, A. Akdag, M. K. MacLeod, X. Chen, D. E. David, M. A. Ratner, J. R. Miller, A. J. Nozik, and J. Michl, "Toward Designed Singlet Fission: Electronic States and Photophysics of 1,3-diphenylisobenzofuran," *Journal of Physical Chemistry A*, 2010.

[294] M. Ullah, S. D. Yambem, E. G. Moore, E. B. Namdas, and A. K. Pandey, "Singlet Fission and Triplet Exciton Dynamics in Rubrene/Fullerene Heterojunctions: Implications for Electroluminescence," *Advanced Electronic Materials*, 2015.

[295] V. M. Nichols, K. Broch, F. Schreiber, and C. J. Bardeen, "Excited-State Dynamics of Diindenoperylene in Liquid Solution and in Solid Films," *Journal of Physical Chemistry C*, 2015.

[296] S. Lukman, K. Chen, J. M. Hodgkiss, D. H. Turban, N. D. Hine, S. Dong, J. Wu, N. C. Greenham, and A. J. Musser, "Tuning the Role of Charge-Transfer States in Intramolecular Singlet Exciton Fission Through Side-Group Engineering," *Nature Communications*, 2016.

[297] E. A. Margulies, C. E. Miller, Y. Wu, L. Ma, G. C. Schatz, R. M. Young, and M. R. Wasielewski, "Enabling Singlet Fission by Controlling Intramolecular Charge Transfer in π-Stacked Covalent Terrylenediimide Dimers," *Nature Chemistry*, 2016.

[298] J. N. Schrauben, A. Akdag, J. Wen, Z. Havlas, J. L. Ryerson, M. B. Smith, J. Michl, and J. C. Johnson, "Excitation Localization/Delocalization Isomerism in a Strongly Coupled Covalent Dimer of 1,3-Diphenylisobenzofuran," *Journal of Physical Chemistry A*, 2016.

[299] M. J. Tayebjee, K. Schwarz, R. MacQueen, M. Dvorák, A. W. Lam, K. Ghiggino, D. McCamey, T. Schmidt, and G. Conibeer, "Morphological Evolution and Singlet Fission in Aqueous Suspensions of TIPS-Pentacene Nanoparticles," *The Journal of Physical Chemistry C*, vol. 120, no. 1, pp. 157–165, 2016.

[300] D. Kato, H. Sakai, N. V. Tkachenko, and T. Hasobe, "High-Yield Excited Triplet States in Pentacene Self-Assembled Monolayers on Gold Nanoparticles through Singlet Exciton Fission," *Angewandte Chemie - International Edition*, 2016.

[301] Y. H. L. Lin, M. A. Fusella, O. V. Kozlov, X. Lin, A. Kahn, M. S. Pshenichnikov, and B. P. Rand, "Morphological Tuning of the Energetics in Singlet Fission Organic Solar Cells," *Advanced Functional Materials*, 2016.

[302] N. V. Korovina, S. Das, Z. Nett, X. Feng, J. Joy, R. Haiges, A. I. Krylov, S. E. Bradforth, and M. E. Thompson, "Singlet Fission in a Covalently Linked Cofacial Alkynyltetracene Dimer," *Journal of the American Chemical Society*, vol. 138, no. 2, pp. 617–627, 2016.

[303] J. J. Burdett, A. M. Müller, D. Gosztola, and C. J. Bardeen, "Excited State Dynamics in Solid and Monomeric Tetracene: The Roles of Superradiance and Exciton Fission," *Journal of Chemical Physics*, 2010.

[304] S. N. Sanders, E. Kumarasamy, A. B. Pun, K. Appavoo, M. L. Steigerwald, L. M. Campos, and M. Y. Sfeir, "Exciton Correlations in Intramolecular Singlet Fission," *Journal of the American Chemical Society*, 2016.

[305] A. K. Le, J. A. Bender, and S. T. Roberts, "Slow Singlet Fission Observed in a Polycrystalline Perylenediimide Thin Film," *Journal of Physical Chemistry Letters*, 2016.

[306] J. D. Cook, T. J. Carey, and N. H. Damrauer, "Solution-Phase Singlet Fission in a Structurally Well-Defined Norbornyl-Bridged Tetracene Dimer," *Journal of Physical Chemistry A*, 2016.

[307] C. M. Mauck, P. E. Hartnett, E. A. Margulies, L. Ma, C. E. Miller, G. C. Schatz, T. J. Marks, and M. R. Wasielewski, "Singlet Fission via an Excimer-Like Intermediate in 3,6-Bis(thiophen-2-yl)diketopyrrolopyrrole Derivatives," *Journal of the American Chemical Society*, 2016.

[308] Y.-D. Zhang, Y. Wu, Y. Xu, Q. Wang, K. Liu, J.-W. Chen, J.-J. Cao, C. Zhang, H. Fu, and H.-L. Zhang, "Excessive Exoergicity Reduces Singlet Exciton Fission Efficiency of Heteroacenes in Solutions," *Journal of the American Chemical Society*, 2016.

[309] T. Yago, K. Ishikawa, R. Katoh, and M. Wakasa, "Magnetic Field Effects on Triplet Pair Generated by Singlet Fission in an Organic Crystal: Application of Radical Pair Model to Triplet Pair," *Journal of Physical Chemistry C*, 2016.

[310] T. Sun, L. Shen, H. Liu, X. Sun, and X. Li, "Synthesis and Photophysical Properties of a Single Bond Linked Tetracene Dimer," *Journal of Molecular Structure*, 2016.

[311] T. Sakuma, H. Sakai, Y. Araki, T. Mori, T. Wada, N. V. Tkachenko, and T. Hasobe, "Long-Lived Triplet Excited States of Bent-Shaped Pentacene Dimers by Intramolecular Singlet Fission," *Journal of Physical Chemistry A*, 2016.

[312] A. K. Le, J. A. Bender, D. H. Arias, D. E. Cotton, J. C. Johnson, and S. T. Roberts, "Singlet Fission Involves an Interplay between Energetic Driving Force and Electronic Coupling in Perylenediimide Films," *Journal of the American Chemical Society*, 2018.

[313] X. Tian, L. Zhou, X. Chen, Y. Meng, Z. Xiong, X. Zhou, and Y. Zhang, "Nanoscale Exponential Distance Dependence and Electron-Transfer Model for Intermolecular Singlet Exciton Fission Observed in Rubrene-Doped Organic Films," *Organic Electronics*, 2017.

[314] R. Katoh, M. Hashimoto, A. Takahashi, Y. Sonoda, T. Yago, and M. Wakasa, "Singlet Fission in Fluorinated Diphenylhexatrienes," *Journal of Physical Chemistry C*, 2017.

[315] G. B. Piland and C. J. Bardeen, "Photoluminescence Dynamics in Singlet Fission Chromophore Liquid Melts," *Chemical Physics Letters*, 2017.

[316] S. Izadnia, D. W. Schönleber, A. Eisfeld, A. Ruf, A. C. LaForge, and F. Stienkemeier, "Singlet Fission in Weakly Interacting Acene Molecules," *Journal of Physical Chemistry Letters*, 2017.

[317] J. C. Dean, R. Zhang, R. K. Hallani, R. D. Pensack, S. N. Sanders, D. G. Oblinsky, S. R. Parkin, L. M. Campos, J. E. Anthony, and G. D. Scholes, "Photophysical Characterization and Time-Resolved Spectroscopy of a Anthradithiophene Dimer:

Exploring the Role of Conformation in Singlet Fission," *Physical Chemistry Chemical Physics*, 2017.

[318] A. Thampi, H. L. Stern, A. Cheminal, M. J. Tayebjee, A. J. Petty, J. E. Anthony, and A. Rao, "Elucidation of Excitation Energy Dependent Correlated Triplet Pair Formation Pathways in an Endothermic Singlet Fission System," *Journal of the American Chemical Society*, 2018.

[319] H. Liu, R. Wang, L. Shen, Y. Xu, M. Xiao, C. Zhang, and X. Li, "A Covalently Linked Tetracene Trimer: Synthesis and Singlet Exciton Fission Property," *Organic Letters*, 2017.

[320] S. Lukman, J. M. Richter, L. Yang, P. Hu, J. Wu, N. C. Greenham, and A. J. Musser, "Efficient Singlet Fission and Triplet-Pair Emission in a Family of Zethrene Diradicaloids," *Journal of the American Chemical Society*, 2017.

[321] A. B. Pun, S. N. Sanders, E. Kumarasamy, M. Y. Sfeir, D. N. Congreve, and L. M. Campos, "Triplet Harvesting from Intramolecular Singlet Fission in Polytetracene," *Advanced Materials*, 2017.

[322] C. K. Yong, A. J. Musser, S. L. Bayliss, S. Lukman, H. Tamura, O. Bubnova, R. K. Hallani, A. Meneau, R. Resel, M. Maruyama, S. Hotta, L. M. Herz, D. Beljonne, J. E. Anthony, J. Clark, and H. Sirringhaus, "The Entangled Triplet Pair State in Acene and Heteroacene Materials," *Nature Communications*, 2017.

[323] J. J. Burdett, D. Gosztola, and C. J. Bardeen, "The Dependence of Singlet Exciton Relaxation on Excitation Density and Temperature in Polycrystalline Tetracene Thin Films: Kinetic Evidence for a Dark Intermediate State and Implications for Singlet Fission," *Journal of Chemical Physics*, 2011.

[324] P. I. Dron, J. Michl, and J. C. Johnson, "Singlet Fission and Excimer Formation in Disordered Solids of Alkyl-Substituted 1,3-Diphenylisobenzofurans," *Journal of Physical Chemistry A*, 2017.

[325] H. Liu, X. Wang, L. Pan, L. Shen, X. Wang, Q. Chen, and X. Li, "Synthesis and Photophysical Properties of a Bistetracene Compound with Slipped Stacked Structure," *Journal of Photochemistry and Photobiology A: Chemistry*, 2017.

[326] Y. V. Aulin, K. M. Felter, D. D. Günbas, R. K. Dubey, W. F. Jager, and F. C. Grozema, "Morphology-Independent Efficient Singlet Exciton Fission in Perylene Diimide Thin Films," *ChemPlusChem*, 2018.

[327] A. J. Tilley, R. D. Pensack, E. L. Kynaston, G. D. Scholes, and D. S. Seferos, "Singlet Fission in Core-Shell Micelles of End-Functionalized Polymers," *Chemistry of Materials*, 2018.

[328] C. B. Dover, J. K. Gallaher, L. Frazer, P. C. Tapping, A. J. Petty, M. J. Crossley, J. E. Anthony, T. W. Kee, and T. W. Schmidt, "Endothermic Singlet Fission is Hindered by Excimer Formation," *Nature Chemistry*, 2018.

[329] B. Manna, A. Nandi, and R. Ghosh, "Ultrafast Singlet Exciton Fission Dynamics in 9,10-Bis(phenylethynyl)anthracene Nanoaggregates and Thin Films," *Journal of Physical Chemistry C*, 2018.

[330] S. Masoomi-Godarzi, M. Liu, Y. Tachibana, L. Goerigk, K. P. Ghiggino, T. A. Smith, and D. J. Jones, "Solution-Processable, Solid State Donor–Acceptor Materials for Singlet Fission," *Advanced Energy Materials*, 2018.

[331] J. K. H. Pun, J. K. Gallaher, L. Frazer, S. K. K. Prasad, C. B. Dover, R. W. MacQueen, and T. W. Schmidt, "TIPS-Anthracene: a Singlet Fission or Triplet Fusion Material?," *Journal of Photonics for Energy*, 2018.

[332] G. Lavarda, J. Zirzlmeier, M. Gruber, P. R. Rami, R. R. Tykwinski, T. Torres, and D. M. Guldi, "Tuning Intramolecular Förster Resonance Energy Transfer and Activating Intramolecular Singlet Fission," *Angewandte Chemie - International Edition*, 2018.

[333] T. Yamakado, S. Takahashi, K. Watanabe, Y. Matsumoto, A. Osuka, and S. Saito, "Conformational Planarization versus Singlet Fission: Distinct Excited-State Dynamics of Cyclooctatetraene-Fused Acene Dimers," *Angewandte Chemie - International Edition*, 2018.

[334] T. Banerjee, S. P. Hill, M. A. Hermosilla-Palacios, B. D. Piercy, J. Haney, B. Casale, A. E. Deprince, M. D. Losego, V. D. Kleiman, and K. Hanson, "Diphenylisobenzofuran Bound to Nanocrystalline Metal Oxides: Excimer Formation, Singlet Fission, Electron Injection, and Low Energy Sensitization," *Journal of Physical Chemistry C*, 2018.

[335] Y. J. Bae, G. Kang, C. D. Malliakas, J. N. Nelson, J. Zhou, R. M. Young, Y. L. Wu, R. P. Van Duyne, G. C. Schatz, and M. R. Wasielewski, "Singlet Fission in 9,10-Bis(phenylethynyl)anthracene Thin Films," *Journal of the American Chemical Society*, 2018.

[336] H. Nagashima, S. Kawaoka, S. Akimoto, T. Tachikawa, Y. Matsui, H. Ikeda, and Y. Kobori, "Singlet-Fission-Born Quintet State: Sublevel Selections and Trapping by Multiexciton Thermodynamics," *Journal of Physical Chemistry Letters*, 2018.

[337] J. Hu, K. Xu, L. Shen, Q. Wu, G. He, J. Y. Wang, J. Pei, J. Xia, and M. Y. Sfeir, "New Insights into the Design of Conjugated Polymers for Intramolecular Singlet Fission," *Nature Communications*, 2018.

[338] C. M. Mauck, Y. J. Bae, M. Chen, N. Powers-Riggs, Y.-L. Wu, and M. R. Wasielewski, "Charge-Transfer Character in a Covalent Diketopyrrolopyrrole Dimer: Implications for Singlet Fission," *ChemPhotoChem*, 2018.

[339] H. Liu, Z. Wang, X. Wang, L. Shen, C. Zhang, M. Xiao, and X. Li, "Singlet Exciton Fission in a Linear Tetracene Tetramer," *Journal of Materials Chemistry C*, 2018.

[340] R. Montero, V. Martínez-Martínez, A. Longarte, N. Epelde-Elezcano, E. Palao, I. Lamas, H. Manzano, A. R. Agarrabeitia, I. López Arbeloa, M. J. Ortiz, and I. Garcia-Moreno, "Singlet Fission Mediated Photophysics of BODIPY Dimers," *Journal of Physical Chemistry Letters*, 2018.

[341] S. T. Roberts, R. E. McAnally, J. N. Mastron, D. H. Webber, M. T. Whited, R. L. Brutchey, M. E. Thompson, and S. E. Bradforth, "Efficient Singlet Fission Discovered in a Disordered Acene Film," *Journal of the American Chemical Society*, 2012.

[342] E. A. Wolf, D. M. Finton, V. Zoutenbier, and I. Biaggio, "Quantum Beats of a Multiexciton State in Rubrene Single Crystals," *Applied Physics Letters*, 2018.

[343] F. S. Conrad-Burton, T. Liu, F. Geyer, R. Costantini, A. P. Schlaus, M. S. Spencer, J. Wang, R. H. Sánchez, B. Zhang, Q. Xu, M. L. Steigerwald, S. Xiao, H. Li, C. P. Nuckolls, and X.-Y. Zhu, "Controlling Singlet Fission by Molecular Contortion," *Journal of the American Chemical Society*, 2019.

[344] P. H. Sher, C. H. Chen, T. L. Chiu, C. F. Lin, J. K. Wang, and J. H. Lee, "Distinct Routes of Singlet Fission and Triplet Fusion: A Fluorescence Kinetic Study of Rubrene," *Journal of Physical Chemistry C*, 2019.

[345] L. M. Yablon, S. N. Sanders, H. Li, K. R. Parenti, E. Kumarasamy, K. J. Fallon, M. J. Hore, A. Cacciuto, M. Y. Sfeir, and L. M. Campos, "Persistent Multiexcitons from Polymers with Pendent Pentacenes," *Journal of the American Chemical Society*, 2019.

[346] C. Shen, S. Yan, X. Chen, L. Niu, and Y. Zhang, "Magnetic Field Effect on Singlet Exciton Fission: A Sensitive Probe of Molecular Level Morphology in Organic Films," *Organic Electronics*, 2019.

[347] N. Wollscheid, J. L. Pérez Lustres, O. Kefer, S. Hahn, V. Brosius, U. H. Bunz, M. Motzkus, and T. Buckup, "Oxygen-Catalysed Sequential Singlet Fission," *Nature Communications*, 2019.

[348] W. Ni, G. G. Gurzadyan, J. Zhao, Y. Che, X. Li, and L. Sun, "Singlet Fission from Upper Excited Electronic States of Cofacial Perylene Dimer," *Journal of Physical Chemistry Letters*, 2019.

[349] K. J. Fallon, P. Budden, E. Salvadori, A. M. Ganose, C. N. Savory, L. Eyre, S. Dowland, Q. Ai, S. Goodlett, C. Risko, D. O. Scanlon, C. W. Kay, A. Rao, R. H. Friend, A. J. Musser, and H. Bronstein, "Exploiting Excited-State Aromaticity to Design Highly Stable Singlet Fission Materials," *Journal of the American Chemical Society*, 2019.

[350] J. R. Allardice, A. Thampi, S. Dowland, J. Xiao, V. Gray, Z. Zhang, P. Budden, A. J. Petty, N. J. Davis, N. C. Greenham, J. E. Anthony, and A. Rao, "Engineering Molecular Ligand Shells on Quantum Dots for Quantitative Harvesting of Triplet Excitons Generated by Singlet Fission," *Journal of the American Chemical Society*, 2019.

[351] A. Mandal, M. Chen, E. D. Foszcz, J. D. Schultz, N. M. Kearns, R. M. Young, M. T. Zanni, and M. R. Wasielewski, "Two-Dimensional Electronic Spectroscopy Reveals Excitation Energy-Dependent State Mixing during Singlet Fission in a Terrylenediimide Dimer," *Journal of the American Chemical Society*, vol. 140, no. 51, pp. 17907–17914, 2018.

[352] W.-L. Chan, J. R. Tritsch, and X.-Y. Zhu, "Harvesting Singlet Fission for Solar Energy Conversion: One- Versus Two-Electron Transfer from the Quantum Mechanical Superposition," *Journal of the American Chemical Society*, 2012.

[353] J. R. Tritsch, W.-L. Chan, X. Wu, N. R. Monahan, and X.-Y. Zhu, "Harvesting Singlet Fission for Solar Energy Conversion via Triplet Energy Transfer," *Nature Communications*, 2013.

[354] H. Nagashima, S. Kawaoka, Y. Matsui, T. Tachikawa, H. Ikeda, and Y. Kobori, "Time-Resolved EPR Study on Singlet-Fission Induced Quintet Generation and Subsequent Triplet Dissociation in TIPS-phenyl-tetracene Aggregates," *Journal of Photopolymer Science and Technology*, 2018.

[355] D. Lubert-Perquel, E. Salvadori, M. Dyson, P. N. Stavrinou, R. Montis, H. Nagashima, Y. Kobori, S. Heutz, and C. W. Kay, "Identifying Triplet Pathways in Dilute Pentacene Films," *Nature Communications*, 2018.

[356] S. L. Bayliss, F. Kraffert, R. Wang, C. Zhang, R. Bittl, and J. Behrends, "Tuning Spin Dynamics in Crystalline Tetracene," *Journal of Physical Chemistry Letters*, 2019.

[357] Y. J. Bae, M. D. Krzyaniak, M. B. Majewski, M. Desroches, J. F. Morin, Y. L. Wu, and M. R. Wasielewski, "Competition between Singlet Fission and Spin-Orbit-Induced Intersystem Crossing in Anthanthrene and Anthanthrone Derivatives," *ChemPlusChem*, 2019.

[358] A. B. Pun, A. Asadpoordarvish, E. Kumarasamy, M. J. Tayebjee, D. Niesner, D. R. McCamey, S. N. Sanders, L. M. Campos, and M. Y. Sfeir, "Ultra-fast Intramolecular Singlet Fission to Persistent Multiexcitons by Molecular Design," *Nature Chemistry*, 2019.

[359] T. Saegusa, H. Sakai, H. Nagashima, Y. Kobori, N. V. Tkachenko, and T. Hasobe, "Controlled Orientations of Neighboring Tetracene Units by Mixed Self-Assembled Monolayers on Gold Nanoclusters for High-Yield and Long-Lived Triplet Excited States through Singlet Fission," *Journal of the American Chemical Society*, 2019.

[360] L. R. Weiss, S. L. Bayliss, F. Kraffert, K. J. Thorley, J. E. Anthony, R. Bittl, R. H. Friend, A. Rao, N. C. Greenham, and J. Behrends, "Strongly Exchange-Coupled Triplet Pairs in an Organic Semiconductor," *Nature Physics*, 2017.

[361] B. S. Basel, J. Zirzlmeier, C. Hetzer, S. R. Reddy, B. T. Phelan, M. D. Krzyaniak, M. K. Volland, P. B. Coto, R. M. Young, T. Clark, M. Thoss, R. R. Tykwinski, M. R. Wasielewski, and D. M. Guldi, "Evidence for Charge-Transfer Mediation in the Primary Events of Singlet Fission in a Weakly Coupled Pentacene Dimer," *Chem*, 2018.

[362] S. Jana, A. L. Yapamanu, and S. Umapathy, "Unraveling Structural Dynamics in Isoenergetic Excited S_1 and Multi-Excitonic ^{1}(TT) States of 9,10-Bis(phenylethynyl)anthracene (BPEA) in Solution: Via Ultrafast Raman Loss Spectroscopy," *Physical Chemistry Chemical Physics*, vol. 21, pp. 14341–14349, jul 2019.

[363] X. Wang, R. Wang, L. Shen, Z. Tang, C. Wen, B. Dong, H. Liu, C. Zhang, and X. Li, "Intramolecular Singlet Fission in a Face-to-Face Stacked Tetracene Trimer," *Physical Chemistry Chemical Physics*, 2018.

[364] A. M. Alvertis, S. Lukman, T. J. Hele, E. G. Fuemmeler, J. Feng, J. Wu, N. C. Greenham, A. W. Chin, and A. J. Musser, "Switching Between Coherent and Incoherent Singlet Fission via Solvent-Induced Symmetry Breaking," *Journal of the American Chemical Society*, 2019.

[365] N. J. Thompson, M. W. Wilson, D. N. Congreve, P. R. Brown, J. M. Scherer, T. S. Bischof, M. Wu, N. Geva, M. Welborn, T. Van Voorhis, V. Bulovi, M. G.

Bawendi, and M. A. Baldo, "Energy Harvesting of Non-Emissive Triplet Excitons in Tetracene by Emissive PbS Nanocrystals," *Interdisciplinary Toxicology*, 2018.

[366] N. J. Davis, J. R. Allardice, J. Xiao, A. J. Petty, N. C. Greenham, J. E. Anthony, and A. Rao, "Singlet Fission and Triplet Transfer to PbS Quantum Dots in TIPS-Tetracene Carboxylic Acid Ligands," *Journal of Physical Chemistry Letters*, 2018.

[367] R. Nagata, H. Nakanotani, W. J. Potscavage, and C. Adachi, "Exploiting Singlet Fission in Organic Light-Emitting Diodes," *Advanced Materials*, 2018.

[368] S. W. Tabernig, B. Daiber, T. Wang, and B. Ehrler, "Enhancing Silicon Solar Cells with Singlet Fission: the Case for Förster Resonant Energy Transfer Using a Quantum Dot Intermediate," *Journal of Photonics for Energy*, 2018.

[369] M. S. Niu, X. Y. Yang, C. C. Qin, P. Q. Bi, C. K. Lyu, L. Feng, W. Qin, K. Gao, and X. T. Hao, "Competition Between Singlet Fission and Singlet Exciton Dissociation at the Interface in TIPS-pentacene:IT-4F Blend," *Organic Electronics*, 2019.

[370] H. Lu, X. Chen, J. E. Anthony, J. C. Johnson, and M. C. Beard, "Sensitizing Singlet Fission with Perovskite Nanocrystals," *Journal of the American Chemical Society*, 2019.

[371] D. P. Medina, I. Papadopoulos, G. Lavarda, H. Gotfredsen, P. R. Rami, R. R. Tykwinski, M. S. Rodríguez-Morgade, D. M. Guldi, and T. Torres, "Light-Harvesting Porphyrazines to Enable Intramolecular Singlet Fission," *Nanoscale*, 2019.

[372] B. Daiber, S. P. Pujari, S. Verboom, S. L. Luxembourg, S. W. Tabernig, M. H. Futscher, J. Lee, H. Zuilhof, and B. Ehrler, "A Method to Detect Triplet Exciton Transfer from Singlet Fission Materials into Silicon Solar Cells: Comparing Different Surface Treatments," *Journal of Chemical Physics*, 2020.

[373] A. Ryasnyanskiy and I. Biaggio, "Triplet Exciton Dynamics in Rubrene Single Crystals," *Physical Review B - Condensed Matter and Materials Physics*, 2011.

[374] S. Reineke and M. A. Baldo, "Room Temperature Triplet State Spectroscopy of Organic Semiconductors," *Scientific Reports*, 2014.

[375] C. F. Perkinson, D. P. Tabor, M. Einzinger, D. Sheberla, H. Utzat, T. A. Lin, D. N. Congreve, M. G. Bawendi, A. Aspuru-Guzik, and M. A. Baldo, "Discovery of Blue Singlet Exciton Fission Molecules via a High-Throughput Virtual Screening and Experimental Approach," *Journal of Chemical Physics*, 2019.

[376] C. Y. Wong, S. B. Penwell, B. L. Cotts, R. Noriega, H. Wu, and N. S. Ginsberg, "Revealing Exciton Dynamics in a Small-Molecule Organic Semiconducting Film with Subdomain Transient Absorption Microscopy," *The Journal of Physical Chemistry C*, vol. 117, no. 42, pp. 22111–22122, 2013.

[377] T. Zhu, Y. Wan, Z. Guo, J. Johnson, and L. Huang, "Two Birds with One Stone: Tailoring Singlet Fission for Both Triplet Yield and Exciton Diffusion Length," *Advanced Materials*, 2016.

[378] Y. Wan, G. P. Wiederrecht, R. D. Schaller, J. C. Johnson, and L. Huang, "Transport of Spin-Entangled Triplet Excitons Generated by Singlet Fission," *Journal of Physical Chemistry Letters*, 2018.

[379] A. C. Jones, N. M. Kearns, J. J. Ho, J. T. Flach, and M. T. Zanni, "Impact of Non-Equilibrium Molecular Packings on Singlet Fission in Microcrystals Observed Using 2D White-Light Microscopy," *Nature Chemistry*, 2020.

[380] P. D. Reusswig, D. N. Congreve, N. J. Thompson, and M. A. Baldo, "Enhanced External Quantum Efficiency in an Organic Photovoltaic Cell Via Singlet Fission Exciton Sensitizer," *Applied Physics Letters*, 2012.

[381] N. J. Thompson, E. Hontz, D. N. Congreve, M. E. Bahlke, S. Reineke, T. Van Voorhis, and M. A. Baldo, "Nanostructured Singlet Fission Photovoltaics Subject to Triplet-Charge Annihilation," *Advanced Materials*, 2014.

[382] T. C. Wu, N. J. Thompson, D. N. Congreve, E. Hontz, S. R. Yost, T. Van Voorhis, and M. A. Baldo, "Singlet Fission Efficiency in Tetracene-Based Organic Solar Cells," *Applied Physics Letters*, 2014.

[383] S. L. Bayliss, A. D. Chepelianskii, A. Sepe, B. J. Walker, B. Ehrler, M. J. Bruzek, J. E. Anthony, and N. C. Greenham, "Geminate and Nongeminate Recombination of Triplet Excitons Formed by Singlet Fission," *Physical Review Letters*, 2014.

[384] H. Liu, W. Y. Jia, Y. Zhang, Q. M. Zhang, Y. L. Lei, C. L. Lu, Y. Z. Ling, and Z. H. Xiong, "Tuning Magneto-Electroluminescence in Organic Light Emitting Diodes by Controlling the Competition between Singlet Fission and Triplet Fusion," *Synthetic Metals*, 2014.

[385] X. Qiao, L. Luan, Y. Liu, Z. Yu, and B. Hu, "Inter-Triplet Spin-Spin Interaction Effects on Inter-Conversion Between Different Spin States in Intermediate Triplet-Triplet Pairs Towards Singlet Fission," *Organic Electronics*, 2014.

[386] M. Tabachnyk, B. Ehrler, S. Gélinas, M. L. Böhm, B. J. Walker, K. P. Musselman, N. C. Greenham, R. H. Friend, and A. Rao, "Resonant Energy Transfer of Triplet Excitons from Pentacene to PbSe Nanocrystals," *Nature Materials*, 2014.

[387] L. Yang, M. Tabachnyk, S. L. Bayliss, M. L. Böhm, K. Broch, N. C. Greenham, R. H. Friend, and B. Ehrler, "Solution-Processable Singlet Fission Photovoltaic Devices," *Nano Letters*, 2015.

[388] M. Wakasa, M. Kaise, T. Yago, R. Katoh, Y. Wakikawa, and T. Ikoma, "What Can Be Learned from Magnetic Field Effects on Singlet Fission: Role of Exchange Interaction in Excited Triplet Pairs," *Journal of Physical Chemistry C*, 2015.

[389] "Magneto-Optical Behaviors at a 2-D Ferromagnetic/Organic Semiconductor Interface for Singlet Fission," *Organic Electronics*, 2017.

[390] H. Yonemura, Y. Futaoka, T. Taniguchi, H. Sakaguchi, and S. Yamada, "Effect of Silver Nanoparticle on Singlet Exciton Fission in Rubrene Films," *Molecular Crystals and Liquid Crystals*, 2017.

[391] M. P. Hodges, M. Grell, N. A. Morley, and D. A. Allwood, "Wide Field Magnetic Luminescence Imaging," *Advanced Functional Materials*, 2017.

[392] M. Wakasa, T. Yago, Y. Sonoda, and R. Katoh, "Structure and Dynamics of Triplet-Exciton Pairs Generated from Singlet Fission Studied Via Magnetic Field Effects," *Communications Chemistry*, 2018.

[393] C. Y. Cheng, N. Chitraningrum, X. M. Chen, T. C. Wen, and T. F. Guo, "Magnetic Field Effect of the Singlet Fission Reaction in Tetracene-Based Diodes," *Organic Electronics*, 2018.

[394] S. L. Bayliss, L. R. Weiss, A. Mitioglu, K. Galkowski, Z. Yang, K. Yunusova, A. Surrente, K. J. Thorley, J. Behrends, R. Bittl, J. E. Anthony, A. Rao, R. H. Friend, P. Plochocka, P. C. Christianen, N. C. Greenham, and A. D. Chepelianskii, "Site-selective Measurement of Coupled Spin Pairs in an Organic Semiconductor," *Proceedings of the National Academy of Sciences of the United States of America*, 2018.

[395] K. Ishikawa, T. Yago, and M. Wakasa, "Exploring the Structure of an Exchange-Coupled Triplet Pair Generated by Singlet Fission in Crystalline Diphenylhexatriene: Anisotropic Magnetic Field Effects on Fluorescence in High Fields," *Journal of Physical Chemistry C*, 2018.

[396] X. Tang, Y. Hu, W. Jia, R. Pan, J. Deng, J. Deng, Z. He, and Z. Xiong, "Intersystem Crossing and Triplet Fusion in Singlet-Fission-Dominated Rubrene-Based OLEDs under High Bias Current," *ACS Applied Materials and Interfaces*, 2018.

[397] H. Zhu, W. Jia, L. Chen, X. Tang, Y. Hu, R. Pan, J. Deng, and Z. Xiong, "Trap-induced Conversion from Singlet Fission to Intersystem Crossing: Via In Situ Heating of Rubrene-Based Organic Light-Emitting Diodes," *Journal of Materials Chemistry C*, 2019.

[398] H. Yonemura, D. Aira, N. Asakura, K. Ezoe, and H. Sakaguchi, "Effect of Silver Nanoplate on Singlet Exciton Fission in Rubrene Polymer-Composite Films," *Japanese Journal of Applied Physics*, 2020.

Appendix A

Supplementary Information for Chapter 3: Advancements in Singlet Fission Chromophore Design Enabled by Vibrational Spectroscopies

In Figure 3.2, we listed various spectroscopic techniques that have been applied to studying each corresponding step of the singlet fission process. Here, we list the corresponding references from year 2000 onwards. Transient absorption is excluded because it is the most widely used technique (210 studies since year 2000). To the best of our abilities, the references are accurate as of May 2020.

Here are a list of acronyms and alternative names for the techniques used:

Acronym	Technique name(s)
TR-PL	Time resolved photoluminescence, time resolved fluorescence, time resolved emission, time-correlated single-photon counting
2DES	Two dimensional electronic spectroscopy
TR-2PPE	Time resolved 2 photon photoemission spectroscopy
TR-EPR	Time resolved electron paramagnetic/spin resonance
TRIR	Time resolved infrared spectroscopy, transient mid-infrared spectroscopy
ISRS	Impulsive stimulated Raman spectroscopy
RR	Resonance Raman spectroscopy
FSRS	Femtosecond stimulated Raman spectroscopy, ultrafast Raman loss spectroscopy
TAM	Transient absorption microscopy, pump-probe microscopy, 2D white light microscopy
SO-FSRS	Spatially-offset femtosecond stimulated Raman spectroscopy

Step 1

Technique	References
TR-PL	[42, 44, 46, 60, 93, 94, 101, 103, 114, 116, 123, 126, 199, 241–350]
2DES	[105, 124, 351]
TR-2PPE	[43, 106, 192, 212, 352, 353]
TR-EPR	[107, 108, 128, 246, 247, 249, 257, 336, 349, 354–361]
TRIR	[7, 113, 114, 116, 117]
ISRS	[8, 9, 123, 130, 323]
RR	[105, 121–124]
FSRS	[10, 11, 125, 362]

Step 2

Technique	References
2DES	[105, 351]
TRIR	[7, 113, 116, 117]
FSRS	[10, 11]

Step 3

Technique	References
TR-PL	[44, 46, 93, 103, 114, 126, 241, 245, 247, 248, 257–259, 261, 262, 265–269] [271, 273–276, 278, 279, 282, 284, 288, 295–302, 306, 307, 309, 313, 314] [318, 320, 322–325, 327, 328, 336, 337, 341–343, 348, 363, 364]
2DES	[105, 124, 351]
TR-2PPE	[43, 106, 192, 212, 352, 353]
TR-EPR	[107, 108, 128, 246, 247, 249, 257, 336, 349, 354–361]
TRIR	[7, 114, 116, 117]
RR	[105, 121, 122, 124]

Step 4

Technique	References
TR-PL	[94, 102, 200, 254, 268, 277, 280, 285, 294, 301, 334, 350, 365–372]
TR-2PPE	[43, 192, 352, 353]

Step 5

Technique	References
Delayed fluorescence/ phosphorescence	[60, 241, 251–253, 255, 262, 269–272, 275, 280, 283, 287] [42, 289, 294, 296, 303–305, 308, 312, 315, 318, 321, 322] [333–335, 337, 339, 344, 363, 364, 370, 372–375]

Step 6

Technique	References
Delayed fluorescence microscopy	[60]
TAM	[61, 136, 376–379]
SO-FSRS	[12]

Others

Technique	References
Magnetic field dependence of fluorescence	[269, 270, 284–286, 288, 292, 309] [314, 315, 319, 322, 342, 346, 350] [276, 356, 365, 367, 375, 380–398]

Appendix B

Supplementary Information for Chapter 5: Spatially-Offset Femtosecond Stimulated Raman Spectroscopy

B.1 Identifying the [210] axis in the TIPS-pn Crystal

To identify the [210] axis in the TIPS-pn crystal, we collected the spontaneous Raman spectrum of TIPS-pn crystals using a home-built continuous wave Raman spectrometer along multiple laser polarizations. We sent a 785 nm laser (CVI lasers) through a near-infrared half-wave plate and focused it on the sample through an Olympus microscope with an Olympus Ach 10×/0.25 objective. We measured the transmitted Raman signal using a Princeton Instruments 2500i spectrometer and a Princeton Instruments PIXIS 100BX CCD array. We defined the 0° laser polarization to be parallel to the horizontal laser table surface. We used an acquisition time of 3.5s and measured the Raman spectra of TIPS-pn from -120° to 240° laser polarization with an interval of 4°. The Raman

spectra were normalized with respect to the laser power of 99.9 mW at the sample.

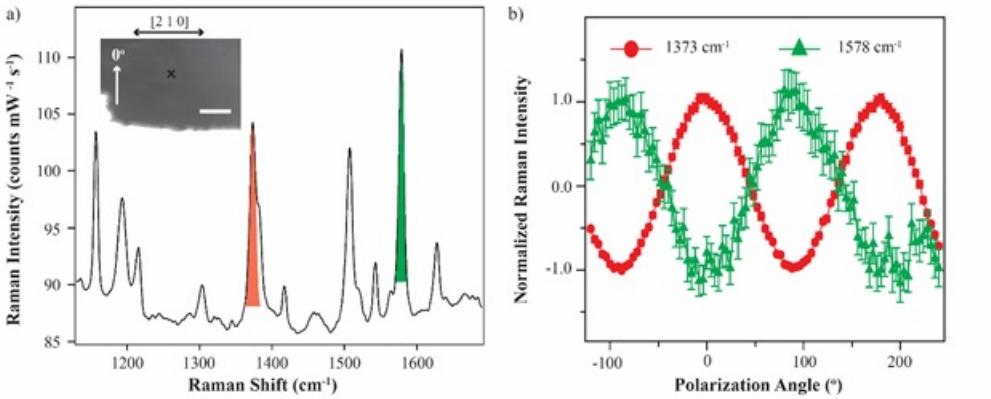

Figure B.1: (a) Spontaneous Raman spectrum of TIPS-pn at 240° laser polarization with respect to the laboratory horizontal axis. The insert shows the 0° polarization and [210] axes, as well as the location on the TIPS-pn crystal where the polarized Raman measurements were made. The scalebar in the picture is 0.2 mm. b) Normalized Raman intensity of 1373 and 1578 cm^{-1} peaks as a function of laser polarization.

We showed a spontaneous Raman spectrum of Tips-pn collected at 240° laser polarization in Figure B.1a, with the 0° polarization axis (parallel to the horizontal surface of the laser table) indicated in the insert. We tracked how the intensity of 1373 and 1578 cm^{-1} changed with polarization angles as shown in Figure SB.1b. We chose these two Raman peaks because they corresponded to C=C molecular vibrations along the short and long axis of the pentacene backbone respectively. [189,191,201,202] Our results are consistent with previous literature that also observed the same anti-phase relationship between the 2 peaks. [189, 191, 201] To identify the fast charge transport axis in our Tips-pn crystal, we compared our results directly to the work published by Onojima et. al., who established the relationship between the crystallographic axis [210] of their Tips-pn crystals and the angular dependence of the 1578 cm-1 peak. [202] When we compared our data in Figure S3b with their published data, we noticed a 90° phase shift of the angular dependence of the 1578 cm^{-1} peak. Since the [210] axis was parallel to the axis at 0° polarization in their work, [149] we deduced that the [210] axis of our

crystal is 90° rotated from our 0° polarization axis and corresponds to the long axis of our crystal as seen in the insert in Figure B.1a.

B.2 Extinction Spectrum of TIPS-pn

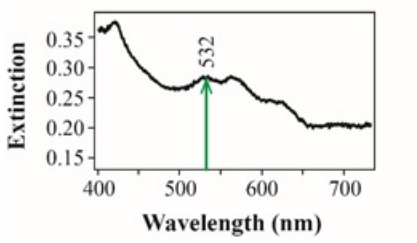

Figure B.2: Extinction spectrum of the TIPS-pn crystal used for SO-FSRS

We measured the extinction spectra of our TIPS-pn crystals using the UV-2600 UV-vis spectrometer by Shimadzu in transmission mode. Due to the small sizes of our crystals, we pierced a hole through a business card with a sewing needle and placed it right in front of our crystals to minimize scattering. Figure B.2 shows the extinction spectrum of the crystal used for SO-FSRS. We can see that it absorbs strongly at the photoexcitation wavelength of 532 nm. We present how we estimated the initial exciton density in a later section of the SI.

B.3 Quantifying Ground State Depletion

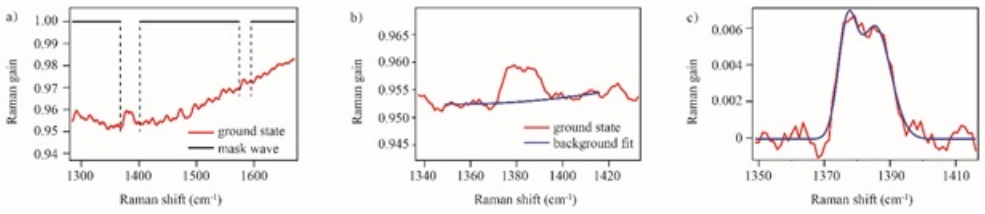

Figure B.3: (a) Ground state Raman spectrum of TIPS-pn and the mask used for background fitting. (b) Example of a polynomial fit of the background of the 1377-1386 cm^{-1} peaks. (c) The ground state spectrum after background subtraction.

We performed a one-to-one subtraction of the ground state FSR spectrum to extract the excited state FSR spectra at each time delay and position. Identifying depletion of ground state Raman features could be challenging because broad transient absorption features were growing in at the same time. To avoid this problem, we identified the frequencies of the Raman peaks, which were cross-referenced to the spontaneous Raman spectrum, from the stimulated ground state Raman spectrum. We fit a local region of each spectrum to a second-order polynomial while excluding the Raman features from the fitting algorithm. Subtracting the polynomial fit from the corresponding spectrum removes contributions from the transient absorption background, leaving behind Raman depletion on a constant background. We then fit these Raman features to gaussian functions based on the ground state fit parameters to obtain the depletion dynamics at each Raman peak. An example is illustrated in SI Figure B.3. All data analyses were performed with Labview, Igor and Matlab.

B.4 Selected SO-FSRS Data Sets

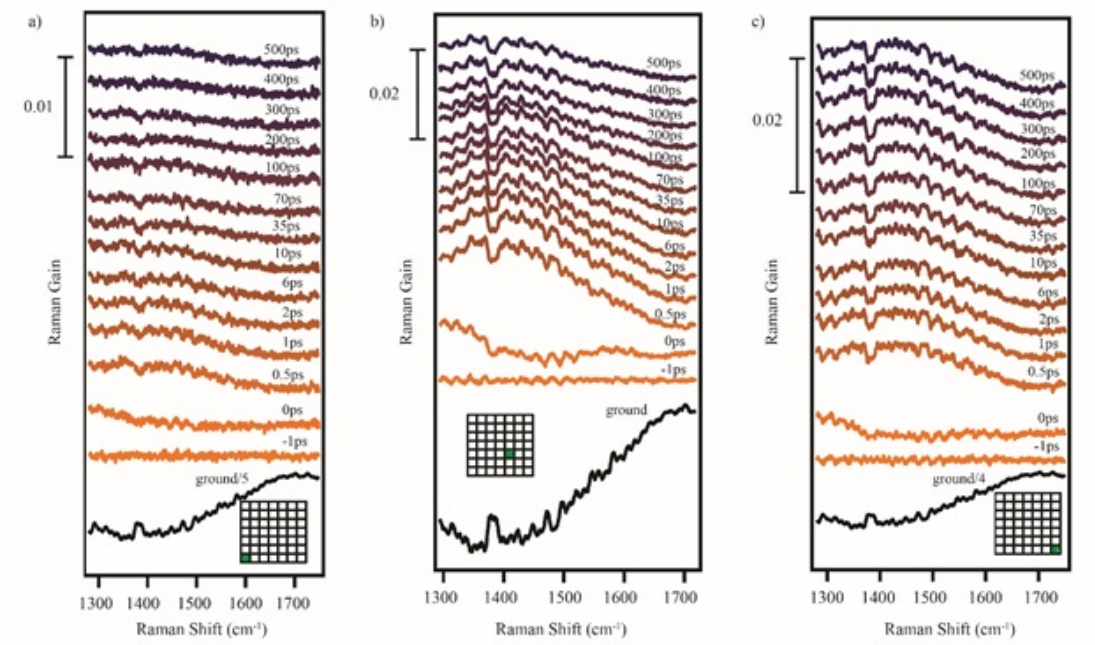

Figure B.4: FSR spectra at photoexcitation positions (a) (2, -4), (b) (0, 0) and (c) (2, 2).

B.5 Estimating Initial Exciton Density

When comparing the peak intensities of the 1377 and 1386 cm^{-1} Raman depletions to their ground state intensities at the (0, 0) position, we estimated that about 34% of TIPS-pn molecules in the photoexcitation region had been promoted to the excited state.

From comparing the extinction spectrum of our TIPS-pn crystal to was published in the literature, [197] we estimated the thickness of our crystal to be ∼100 nm. We know that the diameter of the photoexcitation beam is 18 μm under 40× objective.

Assuming a cylindrical illumination,

Volume illuminated by the photoexcitation pulse $= 100nm \times \pi \times \left(\frac{18\mu m}{2}\right)^2$

$\sim 2.5 \times 10^{13}$ Å^3

From the crystallographic data of TIPS-pn, [184]

Volume per molecule = 7.565 Å×7.75 Å× 1.6835 Å

~ 987 Å^3

$\therefore$ Number of molecules illuminated by the photoexcitation pulse $\sim 2.5 \times 10^{10}$

$\therefore$ Number of excitons generated $\sim 10^9$

B.6 1377 cm^{-1} and 1582 cm^{-1} Raman Depletion Dynamics

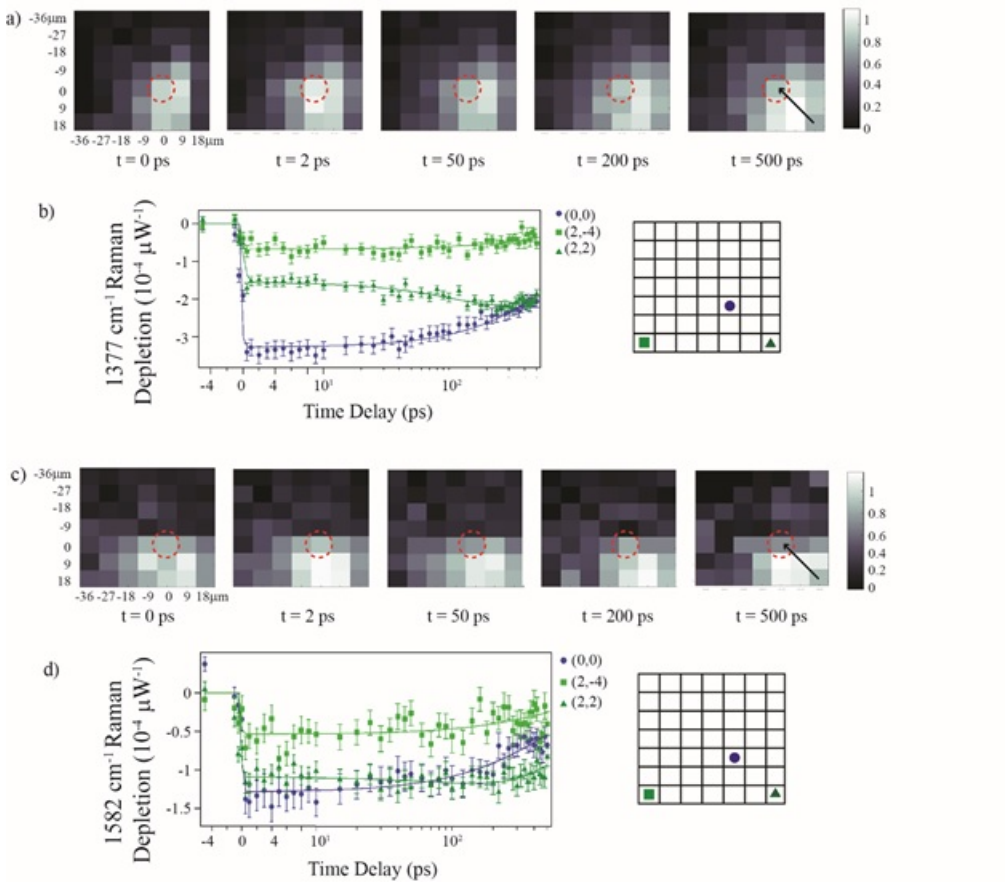

Figure B.5: (a) Evolution of the normalized 1377 cm^{-1} depletion over time. The dashed circle represents the Raman probe pulse and the (0, 0) position. Arrow in the right most panel represents the diffusion direction of the excitons generated in (2, 2), which falls along the fast exciton transport axis. (b) 1377 cm^{-1} Raman depletion dynamics at three photoexcitation locations. The x-axis is linear from -5 to 10 ps and logarithmic from 10 to 500 ps. (c) Evolution of the normalized 1582 cm-1 depletion over time. (d) 1582 cm^{-1} Raman depletion dynamics at three photoexcitation locations.

B.7 Additional SO-FSRS Data Set at Separate Crystal Location

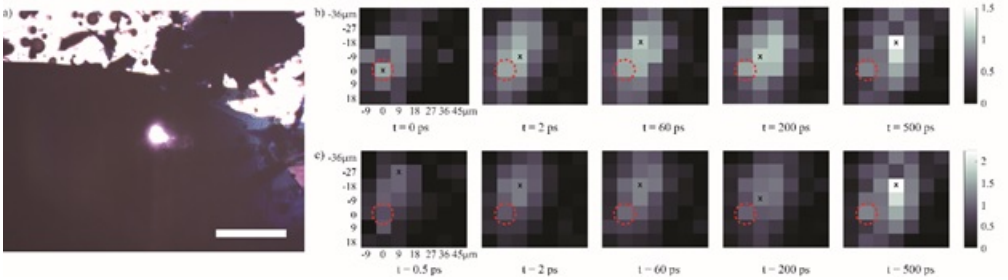

Figure B.6: (a) Location on the Tips-pn crystal under a 10× objective at which we conducted SO-FSRS measurements on. The scalebar is 0.2 mm. (b) Evolution of the normalized 1361 cm^{-1} depletion over time. (c) Evolution of the normalized 1369 cm^{-1} depletion over time. 'X' indicates the position with the strongest depletion. The dashed circle represents the Raman probe pulse and the (0, 0) position.

We performed SO-FSRS measurements at 532 nm photoexcitation at a different location of the same Tips-pn crystal presented in the main paper. From Figure B.6a, we can see that the [210] axis is horizontal to the position of the Raman probe pulse. By using the same analysis methods, we look at how the Raman depletions of 1361 and 1369 cm^{-1} evolve over time in Figures B.6b and B.6c. We used 'X' to depict the photoexcitation position where the Raman depletion is the highest at each time delay. We can see from both figures that these positions are shifting right as time delay increases, implying that excitons generated at those positions are migrating rapidly into the probing region as indicated by the dashed circles. Once again, we see evidence of fast exciton transport along the [210] axis. When we look closely at Figure B.6a again, we see that the right side of the crystal is thinner than the left, leading us to hypothesize that there is a preference for excitons to move from thin side of the crystal to the thicker regions. More experiments have to be conducted to test out our hypothesis.